MICROCOPY RESOLUTION TEST CHART
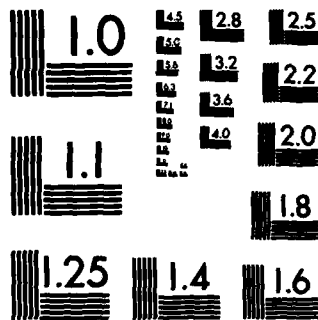NATIONAL BUREAU OF STANDARDS-1963-A

Final Report

AD-A144 194

Erosion Mechanisms of Metals

DTIC
SELECTED
AUG 8 1984
S
A

SOLAR
TURBINES
INCORPORATED

84 08 06 130

Final Report

SR84-R-4526-03
March 1984

Erosion Mechanisms of Metals

M.E. Gulden
K.G. Kubarych

Department of the Air Force
Office of Scientific Research
Bolling Air Force Base, DC 20332

Attn: AFOSR/NE
        Building 410

Contract No. F49620-78-C-0104
July 31, 1978 through August 31, 1983

REPORT DOCUMENTATION PAGE	READ INSTRUCTIONS BEFORE COMPLETING FORM

1. REPORT NUMBER	2. GOVT ACCESSION NO.	3. RECIPIENT'S CATALOG NUMBER
AFOSR-TR- 84-0633	H/44/94	

4. TITLE (and Subtitle)	5. TYPE OF REPORT & PERIOD COVERED
EROSION MECHANISMS OF METALS	FINAL REPORT
	6. PERFORMING ORG. REPORT NUMBER
	SR84-R-4526-03

7. AUTHOR(s)	8. CONTRACT OR GRANT NUMBER(s)
Mary Ellen Gulden & Kenneth G. Kubarych	F49620-78-C-0104

9. PERFORMING ORGANIZATION NAME AND ADDRESS	10. PROGRAM ELEMENT, PROJECT, TASK AREA & WORK UNIT NUMBERS
Solar Turbines Incorporated 2200 Pacific Highway, P.O. Box 805376 San Diego, CA 92138-5376	61102F, 2306, A2

11. CONTROLLING OFFICE NAME AND ADDRESS	12. REPORT DATE
Department of the Air Force Office of Scientific Research Bolling Air Force Base, DC 20332	January 1984
	13. NUMBER OF PAGES

14. MONITORING AGENCY NAME & ADDRESS(if different from Controlling Office)	15. SECURITY CLASS. (of this report)
	Unclassified
	15a. DECLASSIFICATION/DOWNGRADING SCHEDULE

16. DISTRIBUTION STATEMENT (of this Report)

Unclassified - Distribution Unlimited

Approved for public release;
distribution unlimited.

17. DISTRIBUTION STATEMENT (of the abstract entered in Block 20, if different from Report)

18. SUPPLEMENTARY NOTES

19. KEY WORDS (Continue on reverse side if necessary and identify by block number)

Metals	Strain Rate	Scanning Electron Microscopy
Dust Erosion	High Carbon Steel	
Solid Particle Impact	Microstructure	

20. ABSTRACT (Continue on reverse side if necessary and identify by block number)

The objective of this program is to identify the material properties which control erosion, as well as the material removal processes. Based on previous experimental work, an erosion model has been hypothesized and is based on the target stress-strain response beneath the impacting particle. At low particle energies only elastic strain is generated and no damage to the target occurs. At higher energies, the peak stresses increase, leading to brittle fracture or plastic deformation accompanied

DD FORM 1473 EDITION OF 1 NOV 68 IS OBSOLETE

by adiabatic heating. If adiabatic heating occurs, three possibilities arise. One is a temperature increase with no loss of material, and the second is that ductile fracture may occur due to inadequate ductility at whatever temperature is reached. The third is that localized regions attain the melting point prior to ductile fracture.

The original experimental approach was to study a single alloy which exhibits a transition from brittle to ductile type erosion response at room temperature. Brittle erosion is characterized by maximum erosion occurring at 90-degree impingement and ductile erosion is characterizd by maximum erosion occurring at an impingement angle around 30 degrees. SAE 1095 steel did exhibit such a transition as a function of heat treatment, and at 90-degree impingement, erosion increased with increasing hardness of the martensitic structures.

Examination of eroded surfaces and single impact damage revealed that brittle fracture did not occur even on the very hard targets, but rather the localized strain and plasticity of the damaged volume increased with increasing hardness. Plasticity also increased with decreasing particle size. Transformation products in the shear lips formed during impact and subsurface in regions of maximum shear stress on the hard targets are evidence of significant adiabatic heating. Transformation products were absent on the softer tempered targets. A phenomenological explanation for the experimental erosion results is given in terms of variation in strain rate and adiabatic heating during impact, and the attendant changes in mechanical properties of the target.

The erosion experiments performed on 1095 steel target revealed a complex relationship between the strain rate, adiabatic heating and erosion response. To further study this relationship the list of target materials was expanded to include Ti_3Al, 2024 aluminum and pure molybdenum, copper and gold as well as three Fe-Cr binary alloys.

All of the materials tested showed similar results. Typically, erosion rates were greater for large particle (940 micron) erosion and at incidence angles of 30 degrees. Heat treating the steel and aluminum target materials influenced erosion rates when large particles were used, but had little influence for small particles. Additionally, erosion at 30-degree impingement shows little influence by heat treatment for either large or small particles. Evidence of adiabatic heating was found by examining the eroded surfaces of the target materials.

TABLE OF CONTENTS

v

LIST OF FIGURES

LIST OF TABLES

1

INTRODUCTION

This final report summarizes research for the Department of the Air Force, Office of Scientific Research (AFOSF) under contract F49620-78-C-0104, performed in the period from July 1978 through August 1983. Work was directed toward the objective of identifying the material properties which control erosion, as well as the material removal processes. The experimental approach was to initially study a single alloy which exhibits a transition from brittle to ductile type erosion response at room temperature. At a later stage, the dynamic hardness of several substrate materials, both pure metals and alloys, was measured in order to provide a material property obtained under dynamic conditions similar to those during an actual erosion event.

The results can be conveniently separated into two phases as follows:

    Phase I: Erosion Material Removal Mechanisms, and

    Phase II: Correlation Between Dynamic Hardness and Erosion

Each phase will be discussed separately in Section 2.

2

RESEARCH ACCOMPLISHMENTS

2.1 PHASE I - EROSION MATERIAL REMOVAL MECHANISMS

2.1.1 Introduction

The erosion of metals by gases containing particles occurs in a large number of circumstances where performance and life of Air Force systems are severely affected. Although erosion has been investigated extensively over the past 20 years, the actual mechanisms are still not understood, particularly with regard to the rate controlling target properties. The need to understand erosion of metals is made greater by the trend toward materials with marginal ductility such as the titanium aluminides where a wider spectrum of erosion mechanisms may be expected. An understanding of erosion mechanisms is also necessary before modification of materials to improve erosion resistance can be made.

Solid particle erosion can be conveniently separated into two categories termed brittle and ductile erosion response. The ductile mode typical of most metals is characterized by maximum erosion occurring at some intermediate impingement angle between zero and 90 degrees, usually 20-35 degrees (Refs. 1, 2). The brittle mode typical of most ceramics is characterized by the erosion rate increasing with increasing impingement angle to a maximum rate at 90 degrees.

Due principally to the high strain rates and short dwell times during impact, conventional mechanical properties are not sufficient to explain erosion behavior for conditions which simulate a dust erosion environment. For example, it has been shown for a wide variety of pure metals and alloys which exhibit ductile erosion that resistance to erosion increases with increasing hardness of the pure metals (Refs. 1, 2). However, work hardening or heat treating these metals to increase hardness does not significantly alter the erosion resistance. Examination of single impacts and heavily eroded surfaces has shown a high degree of plastic deformation and flow associated with impacts under these conditions (Refs. 1, 3). Under certain conditions, the shear lips which are formed break off during impact (Ref. 3). Due to the short dwell times of impact, on the order of 10^{-6} sec, the deformation is essentially adiabatic and localized temperature increases are expected. The appearance of erosion debris and impact damage has suggested that localized melting may also be a significant contributor to erosion under certain conditions (Refs. 1, 4). However, the existence of melting has not been proven.

3

Strain rates during impact are dependent on both particle size and velocity. Under certain conditions, strain rates during impact on the order of 10^6/sec are expected (Ref. 5). These strain rates may approach or exceed the maximum plastic strain rate which can be accommodated by dislocation motion (determined by elastic shear wave velocity in the target) (Ref. 6). Limited information of the behavior of metals at these high strain rates is available. However, data exists that shows a linear variation of flow stress with strain, i.e., viscous flow at strain rates greater than 10^3/sec (Ref. 6). Further evidence that conventional deformation mechanisms are not necessarily rate controlling for metallic erosion is given by plotting erosion resistance of pure metal versus energy required to melt a unit volume on a log-log basis. A single straight line relationship is observed which exhibits much less deviation from a straight line than a plot of the same data versus hardness. Other basic properties such as bond energy also show good correlation with erosion of pure metals (Refs. 7,8).

The above discussion illustrates some of the unresolved areas in understanding erosion behavior of metals. One approach to elucidate these unresolved areas is to assume that erosion is related to the target stress-strain response beneath the impacting particle. Based on this assumption, a series of events can be postulated based on particle energy transfer (Ref. 9). In simple terms, at low particle energies only elastic strain is generated and no damage to the target occurs. At higher energies, the peak stresses increase, leading either to brittle fracture or to plastic deformation accompanied by adiabatic heating. If adiabatic heating occurs, three possibilities arise. One is a temperature increase with no loss of material, the second is that ductile fracture occurs due to inadequate ductility at whatever temperature is reached. The third is that localized regions attain the melting point prior to ductile fracture.

The initial experimental approach was to study a single target having properties ranging from brittle to ductile under impact conditions which simulate a dust erosion environment and to characterize the changes (both target properties and erosion parameters) which occur at the transition from brittle to ductile erosion behavior. Use of a single material removes the effects of variation of many physical properties (e.g., melting point and elastic modulus) that would complicate the analysis if a series of materials were used. Hutchins (Ref. 10) has concluded that conventional microstructural strengthening mechanisms become less effective as strain rates increase, based on data with strain rates up to 10^3-10^4/sec. Strain rates in erosion are typically 10^5-10^7/sec clearly indicating a need for characterizing erosion of materials in addition to conventionally heat treated alloys. Therefore the variety of materials to be examined was expanded to incorporate "lattice" type changes in addition to microstructural variations. The term lattice is used to mean fundamental characteristics associated with atomic bonding, i.e., bond energy, modulus of elasticity, etc.

2.1.2 Experimental Procedures

Materials

Initially five high carbon steels were selected for target materials. The primary reasons for this selection are that steels are well characterized mechanically and physically and a transition from brittle to ductile erosion behavior at room temperature has been shown previously for 1055 steel (Ref. 11). Furthermore, the procedures to produce the required range of mechanical properties are well documented. A list of the composition of the five target alloys is given in Table 1.

Table 1

Steel Target Compositions

Alloy Designation	Major Alloying Elements
1045	0.45% C
1095	0.95% C
440C	1% C, 1% Mn, 1% Si, 17% Cr
52100	1% C, 1.5% Cr
A2	1% C, 1% Mo, 5% Cr

High carbon content alloys were chosen because of their ability to produce high hardness martensite and a wide range of hardness in a given steel. The more highly alloyed steels exhibit greater hardenability and greater resistance to transformation to equilibrium products.

All of the steels were heat treated to five martensite conditions which were as follows: untempered, tempered to maximum hardness, tempered to maximum fracture toughness (K_{1c}), tempered to a hardness of Rc50 and tempered to a hardness of Rc30. The specific heat treatments varied for each alloy. The general procedure consisted of normalizing all specimens, then heating to above the austenizing temperature in a purified argon atmosphere followed by brine quenching. Some of the alloys required a further quench in dry ice plus acetone or liquid nitrogen to transform retained austenite and produce a fully martensitic alloy. For maximum hardness, all alloys were tempered in boiling water.

The specimens were chemically milled 0.02 cm after heat treatment to remove any scale or decarburized material. The specimens were again immersed in boiling water to remove any hydrogen introduced during the chemical milling treatment.

5

This rather elaborate specimen preparation procedure was considered necessary to produce consistent, well characterized target material.

Both micro and macro hardness measurments were made along with metallographic examination of the structures to ensure that the desired properties were produced. Although hardness does not categorically define mechanical properties, it was considered a sufficient property for this initial phase of the investigation. The heat treated hardnesses are shown in Table 2.

Table 2

Heat Treated Hardnesses of Alloys (Rc)

Heat Treat Condition \ Alloy Designation	1045	1095	52100	440C	A2
Untempered martensite	59	64	63	61	65
Tempered to maximum hardness	60	66	67	62	67
Tempered to maximum fracture toughness (K_{1c})	57	63	63	58	59
Tempered to Rc50	41	50	53	44	50
Tempered to Rc	29	30	33	31	26

After the initial work on the microstructural controlled steels, the number of materials was expanded to include those with "lattice" type variations. A list of the materials examined is given in Table 3.

The 1095 steel was erosion tested in the quenched and tempered condition as previously described. The 2024 aluminum is an age-hardeneable alloy, hardening is produced primarily by precipitation of the intermetallic phase γ' (i.e., $CuAl_2$). The materials were treated to three standard conditions 2024-0 furnace annealed, 2024-T3 solution treated, and 2024-T81 precipitation hardened. Typical mechanical properties of the materials tested are shown in Table 4.

Erosion Testing

Erosion tests were performed with a stationary target impacted by particles accelerated in an air stream. Particles are injected into the stream three

6

Table 3

Expanded List of Target Materials

Material	Condition
2024 Aluminum	Heat Treated
Alpha Ti_3Al	Heat Treated
OFHC Copper	Annealed
Molybdenum	Annealed
Gold	Annealed
Iron	Annealed
Fe-20wt%Cr	Annealed
Fe-30wt%Cr	Annealed

Table 4

Target Properties

Material	y (MPa)	Shear (MPa)	E (GPa)	Hardness (GPa)	Density (gm/cm^3)
2024Al-0	76	120	73	0.6	2.77
-T3	340	280	73	1.5	2.77
-T81	450	280	73	1.6	2.77
OFHC Copper	140	-	117	0.7	8.92
Molybdenum	570	-	324	2.0	10.2
Gold	-	-	79	-	19.32
Iron	-	-	207	-	7.84
1095 Rc 66	2070	-	207	8.5	7.84
1095 Rc 20	590	-	207	2.4	7.84

Room temperature values

meters from the target to provide sufficient distance for acceleration. The air velocity variation across the 0.95 cm diameter nozzle is less than five percent and velocity can be varied between 15 and 343 m/sec to achieve the desired particle velocity. Particle velocity is measured using the rotating double disc technique (Ref. 12). Particle velocities of 300, 188, 152, 120 and 61 mps for each particle size range were used to establish erosion rates and determine the particle size and velocity dependence on erosion. The particles are fed into the gas stream using a precision feeder at a sufficiently low concentration that particle interactions in the carrier gas stream or on the target surface are negligible. Typical test parameters are outlined in Table 5. A majority of the erosion testing used natural quartz sand

7

Table 5

Erosion Test Conditions

Impingement	(microns)	Particle Velocity (mps)
90°	10	300, 152, 61
	136	213, 152, 50
	273	188, 152, 44
	940	132
60°	10	300
	136	152
	273	152
30°	10	300, 152, 61
	136	213, 152, 50
	273	188, 152, 44
	940	132

(i.e., the major constituent in natural dust) with a few tests being done with SiC particles.

A single particle size range of SiC was used (660-1346 microns) to provide a significant increase in particle energy strain rate decrease.

To assess the type of erosion (brittle or ductile) tests were performed at 30, 60 and 90 degree impingement angles. Brittle type erosion is maximum at 90 degrees and ductile type erosion is maximum at an angle near 30 degrees. The number of particles per test was varied from a few particles (to examine single particle impacts) to as many as 10^{11} particles (400 gms of dust) over a 0.75 cm^2 target area. For long time tests with a large number of particles the specimens were weighed at specific intervals (50 grams of dust each) to assess any changes in erosion with number of impacts. All tests were performed at ambient temperature. In most cases, tests were performed in triplicate to assure reproducibility of the data.

Examination of Eroded Surfaces

The eroded surfaces and single impacts were examined both optically and by scanning electron microscopy (SEM). The energy dispersive X-ray attachment on the SEM was used to detect silicon which would indicate the presence of quartz particle residue. The surfaces were also examined in cross section to assess the nature of subsurface damage.

2.1.3 Erosion of Steel Targets

Erosion Function of Steel Composition and Heat Treatment

Erosion results for the five steels in five heat treat conditions are shown in Figure 1. The data shown is for erosion with 50 grams of 163 micron average particle size quartz traveling at 153 mps. The data points are average values of up to five tests on the same specimen. Weight loss of 0.03 gm corresponds to an approximate depth of 0.005 cm. No incubation period was observed under these test conditions (i.e., weight loss for the first test was not significantly different from that of the fifth test). This implies that either there is no incubation period under these test conditions or that erosion with 50 grams of 163 micron dust exceeds the incubation period. The number of particles in 50 grams of dust corresponds to approximately 100 impacts on the damage area of a single impact. This estimate was made by dividing the total target area subjected to erosion by the area damaged per impact. The damaged area was measured for single impacts.

The alloys 1095, 52100 and A2 do show a transition from a brittle to ductile type of erosion as evidenced by a change in the impingement angle for maximum erosion. For these alloys a brittle type of erosion response is exhibited for the untempered martensite and tempered to maximum hardness condition. The specimens treated to maximize fracture toughness did not show a significant erosion dependence on angle of impingement. The specimens tempered to Rc50 and RC30 exhibited a typical ductile erosion response.

Alloys 1045 and 440C did not exhibit brittle erosion behavior even in the untempered martensitic condition. For the 1045 alloy, this is probably due to the softer, lower carbon martensite which is formed. The microstructure of 440C alloy was very complex and it is likely that a low carbon martensite was produced. Reference to Table 1 shows that 1045 and 440C alloys had the lowest maximum hardness of the alloys investigated.

The results suggest that hardness or flow stress beyond a certain minimum value is required to produce brittle type erosion response. Consequently, not all alloys are expected to exhibit this behavior.

Of interest are the erosion results obtained at 30 degree impingement angle. There is no significant difference in weight loss between the alloys or with various heat treatment. This result is consistent with earlier work, which led to the conclusion that alloying or heat treatment had no effect on erosion (Refs. 1, 2). The results of this work reveal that at higher impingement angles, the heat treat condition can have a major effect on erosion response.

The lack of effect of heat treatment or alloying on erosion at 30 degrees may imply that the same mechanism is operative for each case. During an impact at 30 degrees on a ductile material a ridge or lip is pushed up by the impacting particle (Refs. 1, 3). It has been postulated that this lip is more susceptible to removal by subsequent impacts than the rest of the target (Ref. 3). If this is an important removal process,

9
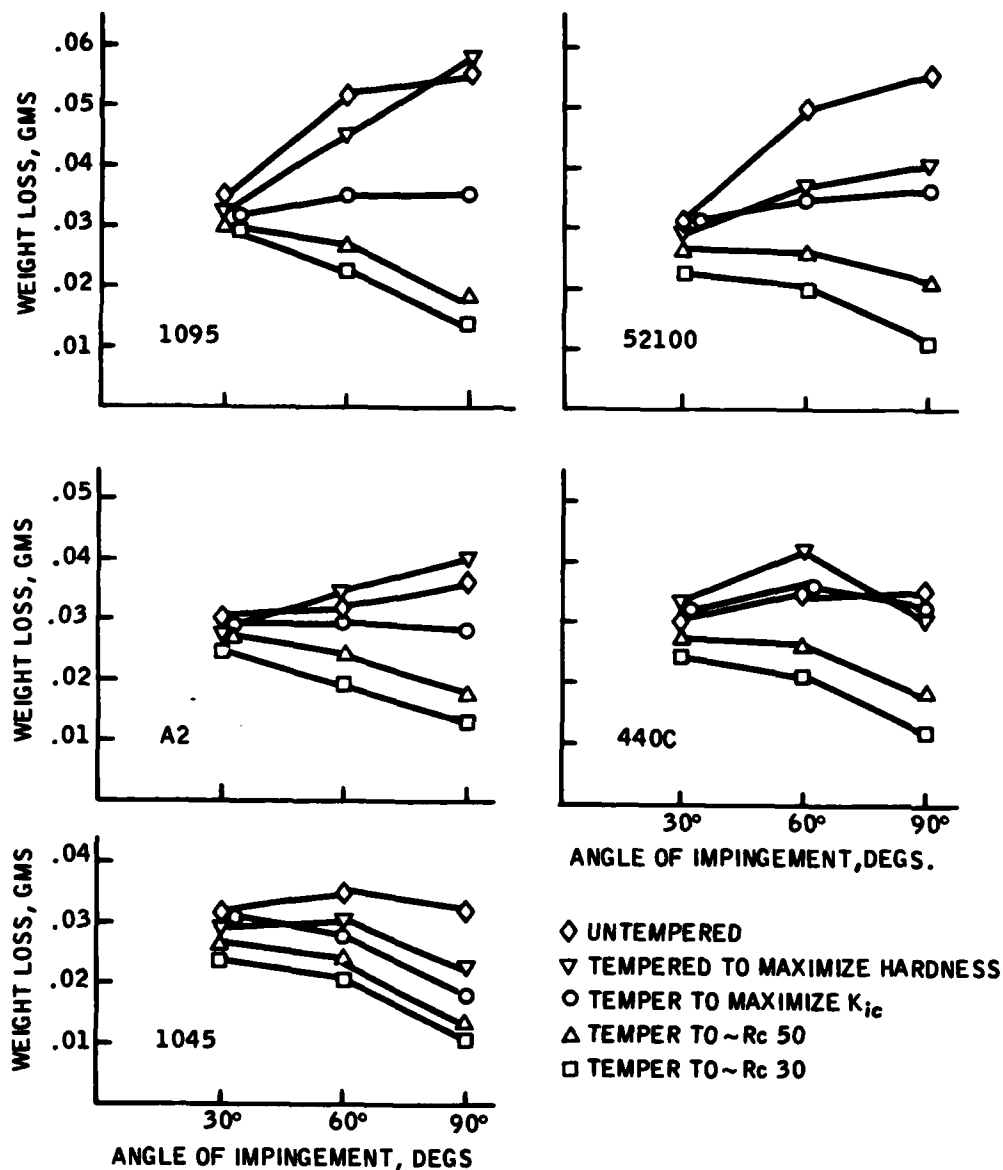
Figure 1.   Erosion of Five Steels as A Function of Impingement
            Angle and Heat Treat Condition; Erosion Conditions -
            50 Grams, 163 Micron Quartz, 153 mps

then these experimental results imply that there is no significant difference
between size or mechanical properties of these lips as a function of heat
treatment. This could occur if temperature excursions during lip formation
were sufficient to temper the material to approximately the same degree of
hardness or flow stress. Another explanation for the lack of dependence of
heat treatment on erosion at 30 degrees is that the same amount of work
hardening or plastic strain is reached.

However, for a ductile erosion response at impingement angles greater than 30 degrees, erosion increases with increasing hardness or flow stress, (see Figure 1, 440C and 1045 steels). This is contrary to earlier models which predicted that erosion was inversely proportional to target flow hardness or stress, and to experimental results on pure metals which do exhibit an inverse hardness or flow stress dependence on erosion (Ref. 2).

To further explore the transition from ductile to brittle erosion response as a function of temper condition the variety of tempering conditions was expanded.

The expanded results are shown in Figure 2 for erosion with 273 and 10 micron particles traveling at 153 mps. There is a transition in angle of maximum erosion as the fully hardened martensite is tempered to softer, lower flow stress material for impact with 273 micron particles. As expected from the prior results both the fully hardened martensite and martensite tempered to maximize fracture toughness again exhibited maximum erosion at 90 degrees. Whereas material tempered into the temper embrittlement region and softened to Rc 50 hardness exhibits maximum erosion at 60 degree impingement angle. The two softest martensitic materials, which are tempered to martensite-ferrite-cementite structures, with hardnesses of Rc 30 and 20, exhibit maximum erosion at 30 degree impingement angle. The material treated to have a large grained pearlite structure, although very soft (Rc 20 hardness), exhibited erosion loss similar to the medium hardness martensitic materials. This is likely a consequence of the parallel lamellar pearlite microstructure.

All of the materials eroded with 10 micron particles exhibited ductile erosion regardless of heat treated hardness, and there was not a significant difference in erosion weight loss between the materials.

The transition in brittle to ductile erosion behavior with hardness, controlled by heat treatment, for the martensitic materials is not unexpected because the ductility or flow stress changes significantly. Of particular interest is the erosion at 90 degrees which is shown in Figure 3 plotted against target hardness. There is reasonable agreement between increasing erosion and increasing hardness for all of the targets except the material heat treated into the temper embrittlement region. This increase in erosion with increasing flow stress is contrary to many of the theories and models for metallic erosion (Refs. 4, 6, 11) which predict that erosion is inversely proportional to flow stress.

The material heat treated into the temper embrittlement region exhibited less erosion than the other targets based on the erosion versus hardness relation at 90 degree impingement angle. Temper embrittlement in this alloy occurs at approximately 232°C (450°F) (Refs. 1, 13). The mechanical properties in this region are not well understood (Ref. 14).

Effect of Particle Energy on Erosion of 1095 Steel

The results shown in Figure 1 reveal that for a given erosion condition or particle energy, a transition between brittle and ductile type erosion
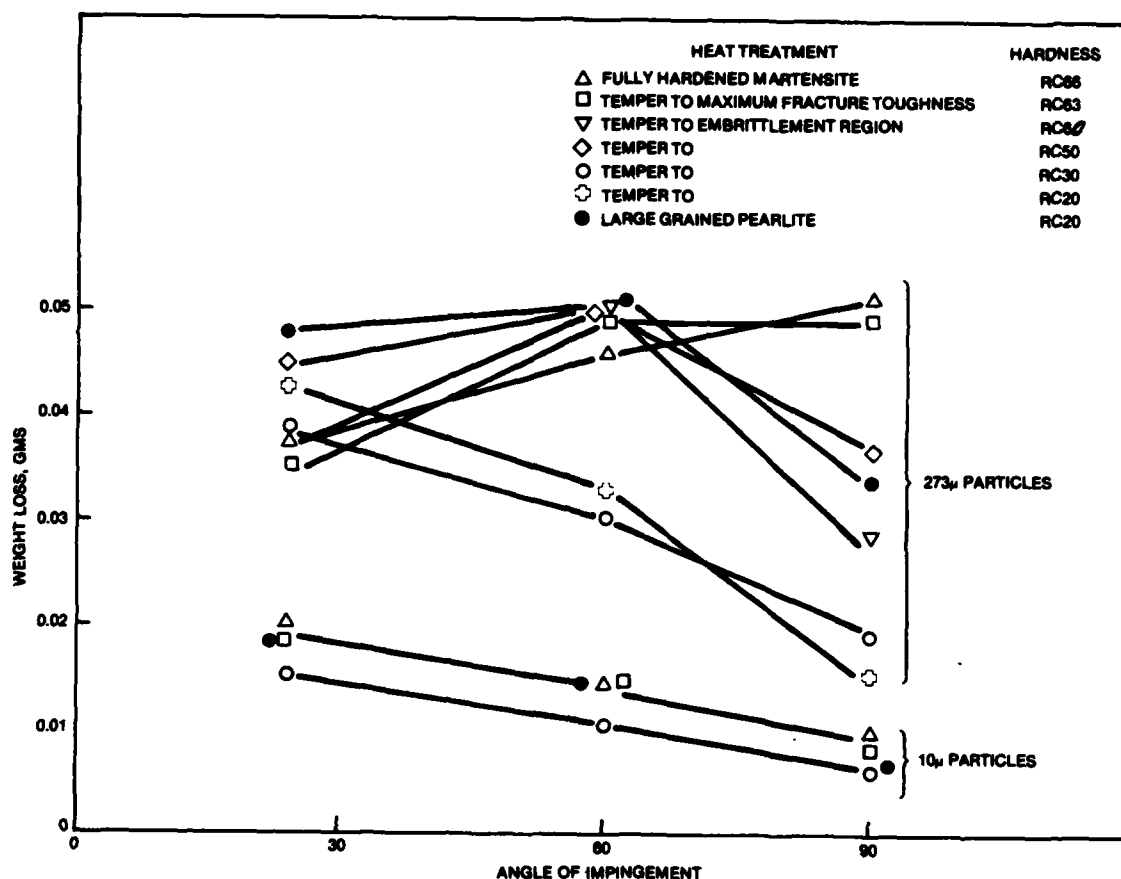
Figure 2. Erosion Weight Loss Versus Angle of Impingement for 1095 Steel
Targets in Various Heat Treat Conditions; Erosion Conditions:
50 Grams Quartz Particles Traveling at 153 mps

can occur for martensitic microstructures and is a function of heat treatment.
To determine the effect of particle energy on this behavior, a series of
tests was performed using 1095 steel as the target in three of the heat treat
conditions. These conditions were tempered to maximum hardness, tempered to
maximum fracture toughness and overtempered to Rc30 hardness. The range of
microstructures obtained is shown in Figure 4. The maximum hardness temper
produced fine grained martensite with uniformly distributed small carbide
particles. There is no evidence of retained austenite. As the specimens
are tempered, the martensite transforms to small grains of ferrite and carbide
particles, producing a mixed structure with no significant change in size of
the carbide particles. Both structures can be considered homogeneous in
comparison to the particle contact areas at least for the larger particles.
Flow stress and ductility will vary appreciably for this range of microstruc-
tures.

The importance of establishing the effect of particle size and velocity on
erosion is two-fold. Particle size and velocity determine the total energy

12
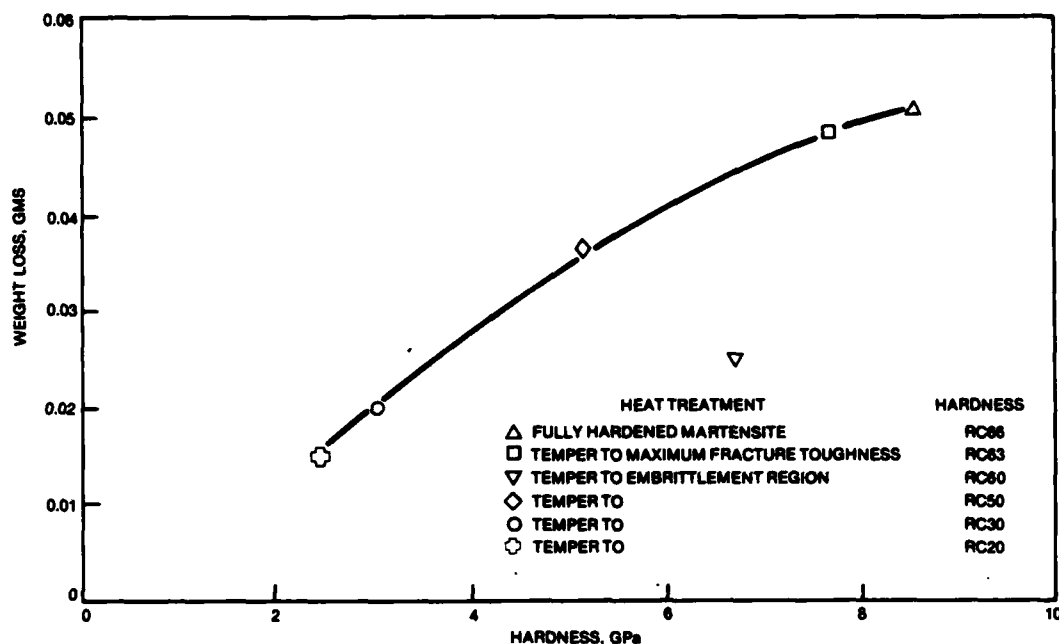
Figure 3.   Erosion Weight Loss Versus Target Hardness of 1095 Steel
at 90 Degree Impingement Angle   (Data taken from Figure 1)

transferred to the target.   Erosion of ductile materials such as metals is
generally proportional to R^3V^2 (a measure of kinetic energy) where R is par-
ticle radius and V is particle velocity (Ref. 1).   For brittle materials such
as ceramics, the radius exponent varies between three and four and the velo-
city exponent can vary between one and five (Ref. 15).   Consequently, a
change in particle size and velocity dependence may be expected through a
ductile to brittle erosion transition.

Figure 5 shows the results of erosion with 273 micron and 10 micron average
size particles traveling at 153 and 61 mps.   Again, as many as five tests for
a given erosion condition were performed on the same specimen.   For impact
with 273 micron particles traveling at 153 mps, the erosion behavior is con-
sistent with that produced by 163 micron particles in that a transition from
ductile to brittle type erosion is observed.   The material, heat treated to
maximum fracture toughness, exhibits a brittle type response for impact with
273 micron particles whereas for impact with 163 micron particles, no effect
of impingement angle was observed.   For impact with 10 micron particles
traveling at 153 mps, the erosion response is ductile regardless of heat
treat condition.   For the 61 mps velocity condition, there is not a signifi-
cant effect of impingement angle or heat treatment on erosion for either 273
or 10 micron impacts (except 90 degree impingement of Rc 30 specimen impacted
with 273 micron particles).   The weight losses are an order of magnitude less
than those for 153 mps impact.   This may indicate that the erosion weight
loss threshold is being approached at least for the 10 micron particle impact.

13
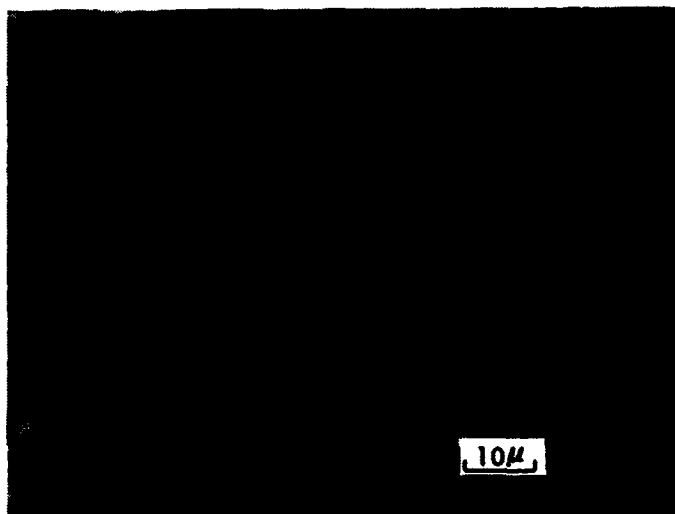
a) Fully Martensitic
   Tempered to Rc66
   (Maximum Hardness)

   Magnification: 1000X
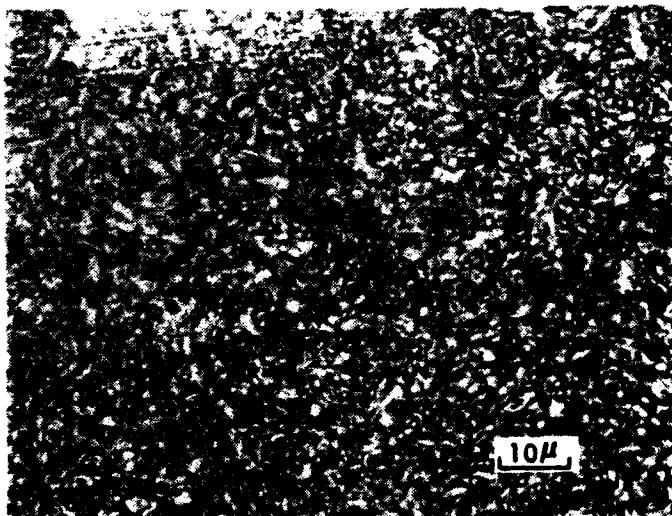
b) Tempered Rc30 Hardness

   Magnification: 1000X

Figure 4.   Range of 1095 Steel Microstructure Used for Erosion Tests

The effect of particle size variation on erosion is shown in Figure 6 where weight loss per impact versus angle of impingement is plotted for a single particle velocity, 153 mps. As would be expected, the amount of material removed decreases with decreasing particle size. The 1095 steel target tempered to Rc 30 exhibits a ductile type of response, as evidenced by maximum erosion at 30 degrees for all particle sizes tested. However, the targets heat treated to maximum hardness do exhibit a transition from brittle to ductile type behavior. For impact with particles 163 microns in diameter and larger, maximum erosion occurs at 90 degrees, which is consistent with a brittle response. For impact with 68 and 49 micron particles, the effect of angle is minimized, and impact with 10 micron particles produced a ductile
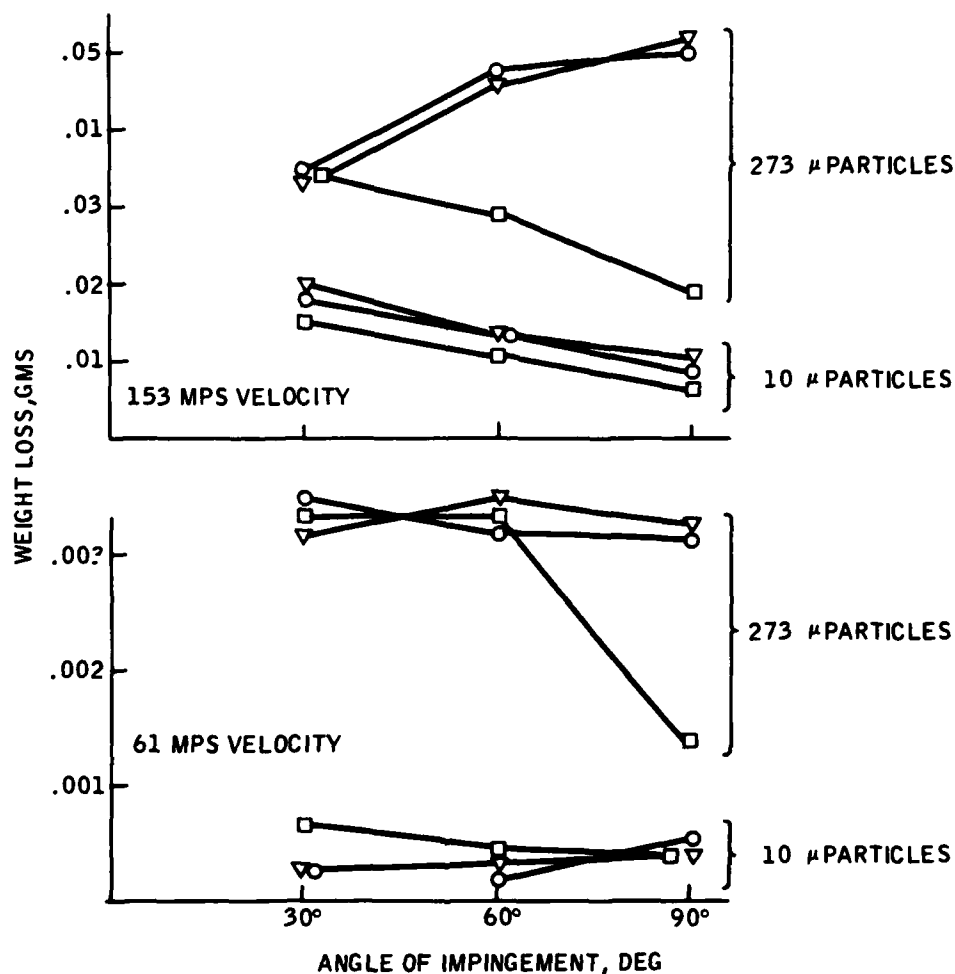
Figure 5. Erosion for 50 Grams of Dust Versus Impingement Angle for 1095
Steel in Three Heat Treat Conditions; ∇= Temper to Maximum
Hardness (Rc 66); O= Temper to Maximum Fracture Toughness
(Rc 63); □= Temper to Rc 30 Hardness

response. These results indicate that the transition between brittle and
ductile erosion behavior is particle size dependent. This could be related
to the change in strain rate expected for these impact conditions. Strain
rates produced by 10 micron particle impacts are expected to be two orders
of magnitude greater than for impact with 1000 micron particles for the same
velocity (Ref. 5). At high strain rates, flow stress can be a direct func-
tion of strain rate and the contribution of conventional strengthening is
minimized.

The effect of velocity variation is further shown in Figure 7 for impact with
273 micron particles on a 1095 steel target in the maximum hardness heat
treat condition. Erosion weight loss and effect of impingement on erosion
both decrease with decreasing velocity. However, a truly ductile response is
not observed.

15

WEIGHT LOSS PER IMPACT, GMS

ANGLE OF IMPINGEMENT, DEGREES

CLOSED SYMBOLS = TEMPER TO MAXIMUM HARDNESS (RC66)

OPEN SYMBOLS = TEMPER TO RC30

▽ 385μ

△ 273μ

□ 163μ

◇ 68μ

○ 10μ
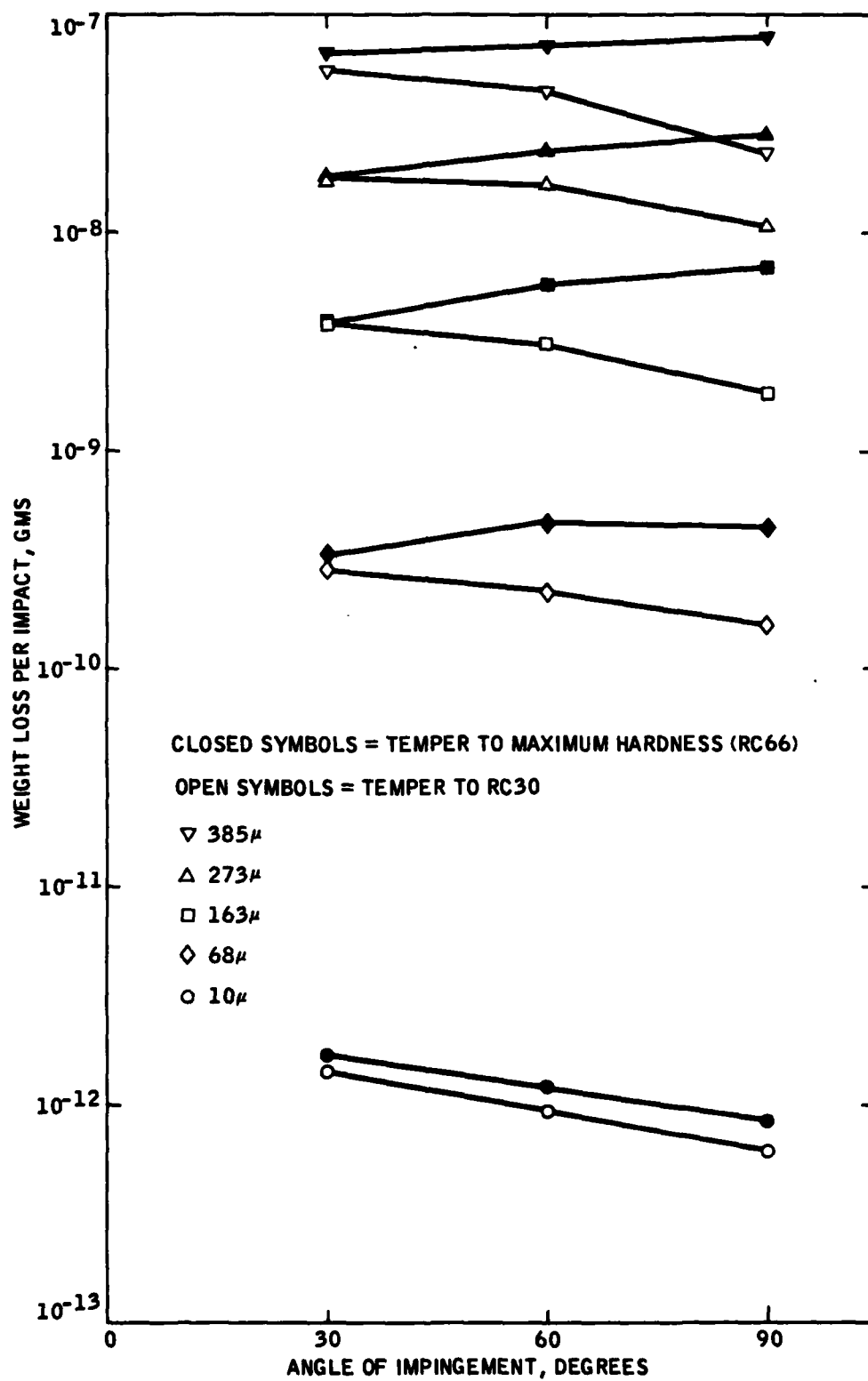
Figure 6.   Effect of Particle Size and Impingement Angle on Erosion of
1095 Steel for a Single Particle Velocity of 153 mps
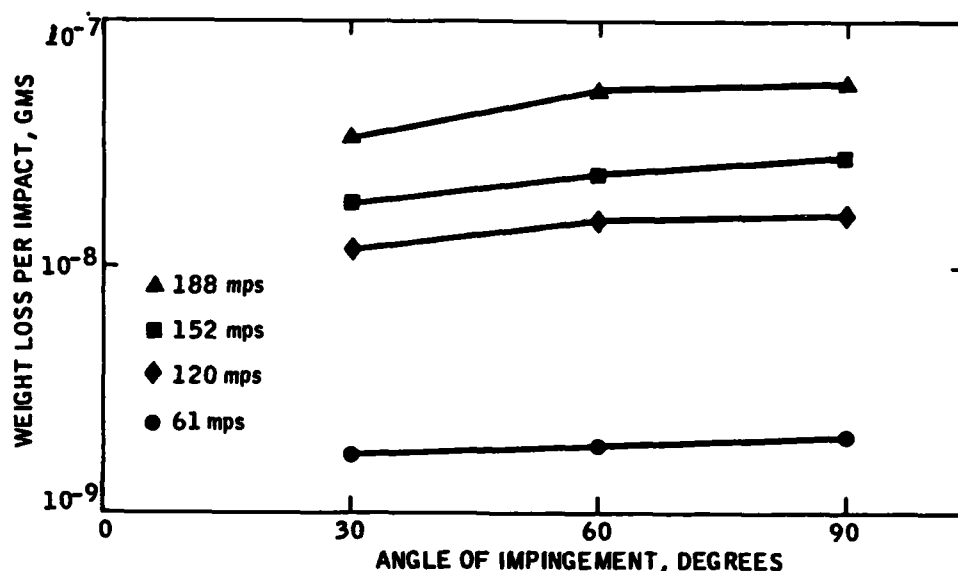
Figure 7. Effect of Particle Velocity and Impingement Angle on
Erosion of 1095 Steel Heat Treated to Maximum Hardness
and Impacted With 273 Micron Particles

Considering the differences in erosion behavior exhibited by the 1095 steel,
it was considered instructive to determine whether the particle size and
velocity dependencies also varied significantly. For ductile materials,
erosion weight loss per impact is generally proportional to particle kinetic
energy or R^3v^2 (Ref. 1). For brittle materials such as ceramics, the radius
exponent varies between three and four and the velocity exponent can vary
between one and five (Ref. 16). The radius exponent was close to three for
all test conditions. The velocity exponent varied between 2.7 and 3.1.
However, this variation was not systematic with variable test condition and
is not considered significant. Figure 8 shows a plot of erosion loss versus
$R^3v^{2.7}$ for the two extremes of heat treat condition and 90 degree impingement.
The slope of both of the lines is close to one. These results indicate that
any difference in erosion mechanisms for these targets is not reflected in a
change of particle size or velocity dependence.

The results have shown that a transition between brittle and ductile type
erosion behavior as evidenced by a change in impingement angle for maximum
erosion not only occurs as a function of martensitic heat treat condition of
some steels, but also as a function of particle size of the impacting particle.
For a given heat treatment, the trend toward brittle behavior increases with
increasing particle size. Erosion is proportional to $R^3v^{2.7}$ regardless of
whether a brittle or ductile erosion response is observed.

The particle size and velocity relate to the total strain produced on impact,
and also determine the strain rate during the impact. It can be shown that
$\varepsilon \sim v^{1/2}/R$ (Ref. 5), so that the strain rate, , produced by, for example, a 10
micron particle, is an order of magnitude greater than that produced by a 100

17

WEIGHT LOSS PER IMPACT, GMS

10^{-7}
10^{-8}
10^{-9}
10^{-10}
10^{-11}
10^{-12}
10^{-13}
10^{-14}

CLOSED SYMBOLS = TEMPER TO MAXIMUM HARDNESS (RC66)

OPEN SYMBOLS = TEMPER TO RC30

▽ 385μ   ◇ 68μ
△ 273μ   ◈ 49μ
◁ 230μ   ○ 10μ
□ 163μ

10^{-12} 10^{-11} 10^{-10} 10^{-9} 10^{-8} 10^{-7} 10^{-6} 10^{-5}

$R^3 V^{2.7}, M^{5.7} SEC^{-2.7}$
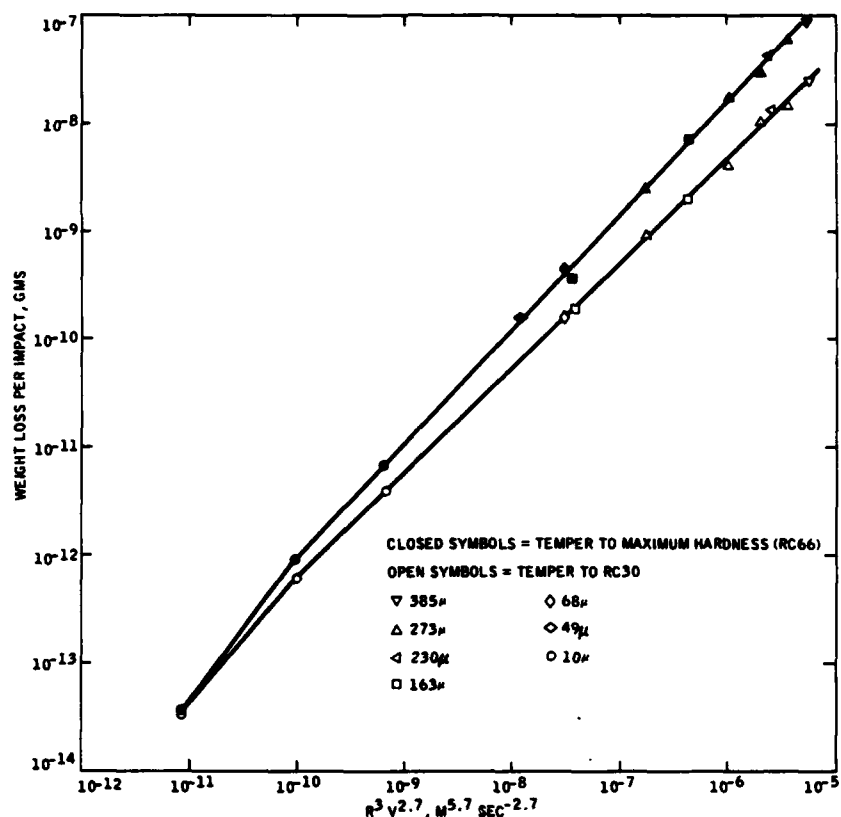
Figure 8. Erosion Versus a Function of Particle Size and Velocity
for 1095 Steel

micron particle traveling at the same velocity. Typical strain rates produced during erosion testing are of the order of 10^4/sec. and greater. Target deformation and fracture at these very high rates may not be controlled by the same mechanisms as low strain rate behavior (dislocation multiplication and movement) and this may provide a possible explanation for the particle size influence on erosion behavior.

To expand on this point, the 1095 steel in the fully hardened martensite and tempered to Rc 30 conditions were eroded with a number of larger particle sizes.

The effect of particle size variation on erosion for this new series of tests is shown in Figure 9 where weight loss per impact versus angle of impingement is plotted for a single particle velocity, 153 mps. As would be expected, the amount of material removed decreases with decreasing particle size. The 1095 steel target tempered to Rc 30 exhibits a ductile type of response, as evidenced by maximum erosion at 30 degrees for all particle sizes tested. However, the targets heat treated to maximum hardness do exhibit a transition from brittle to ductile type behavior. For impact with particles 163 microns in diameter and larger, maximum erosion occurs at 90 degrees, which is consis-

18
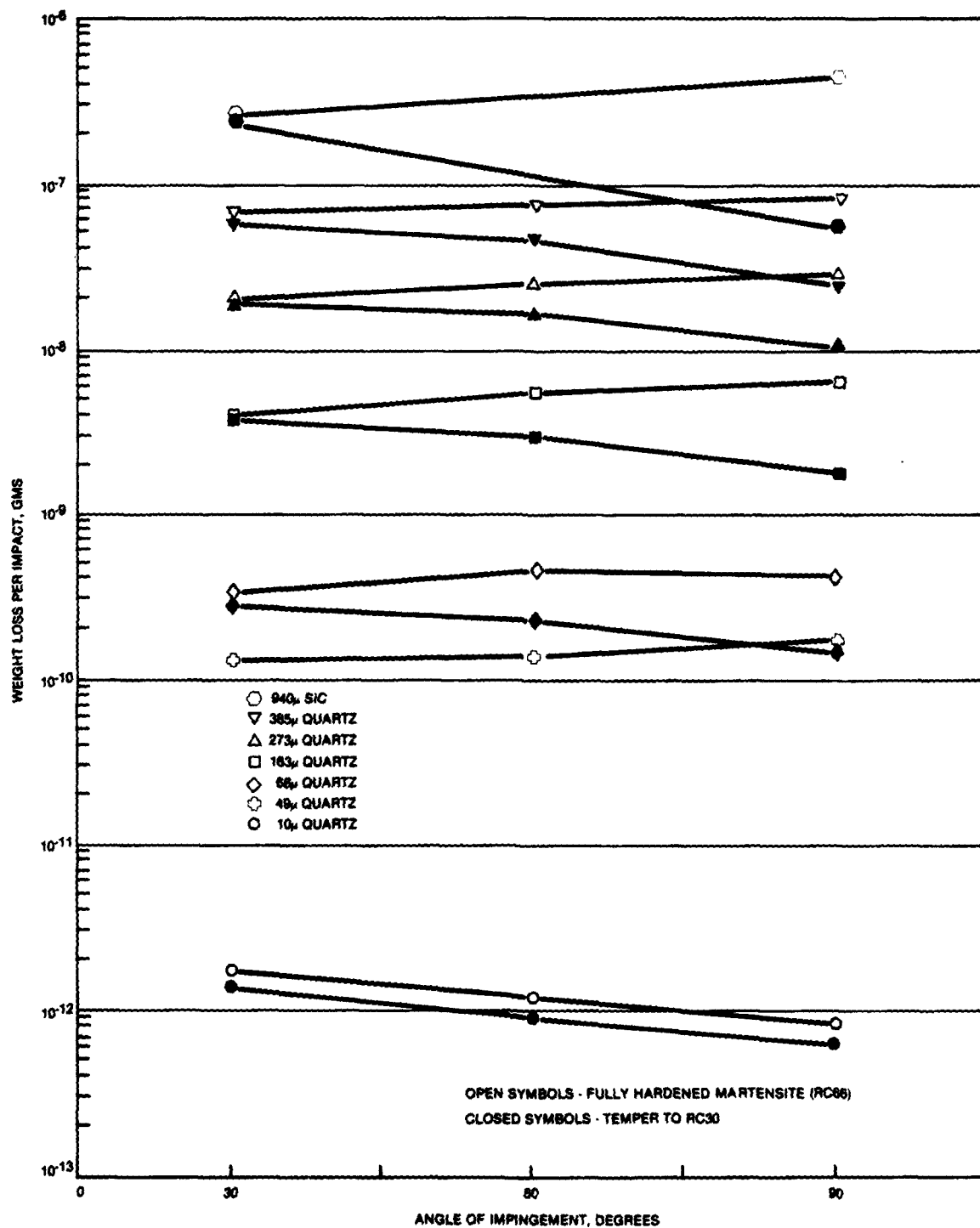
Figure 9. Weight Loss Per Impact Versus Angle of Impingement for 1095 Steel Targets. Particle Velocity = 153 mps

19

tent with a brittle response. For impact with 68 and 49 micron particles, the effect of angle is minimized, and impact with 10 micron particles produced a ductile response. These results indicate that the transition between brittle and ductile erosion behavior is particle size dependent. This could be related to the change in strain rate expected for these impact conditions.

The difference in erosion between the hard and soft targets for 90 degree impingement decreases with decreasing particle size (Fig. 9). There is nearly one order of magnitude difference for erosion with 940 micron SiC particles while for 10 micron particles, erosion loss is essentially the same between the hard and soft heat treatments. For the intermediate particle sizes, the differences are also intermediate. This result may be related to the different strain rates occurring under these test conditions. That is, for impacts with the larger particles, strain rates are comparatively low and hence traditional microstructural strengthening mechanisms may be operative, whereas for impacts with small particles, the strain rates are sufficiently high that the lattice properties become rate controlling, and differences in heat treated flow stress or hardness are minimized.

The strain rate, during an impact, is inversely proportional to the particle size; however, the strain rate is also proportional to the square root of the velocity. Therefore, the effect of velocity on the strain rate and consequently the erosion response is less significant than the particle size. The results shown in Figure 7 of the erosion produced with 273 micron particles traveling at 188, 152, 120 and 61 mps indicates that the weight loss drops with particle velocity, with little or no change in weight loss with impingement angle. This suggests that over this range of velocities the same erosion mechanism is operative; since, the variation in strain rate during impact are all similar. It is not possible with the present equipment to generate velocities over a wide enough range to observe the expected velocity dependence of the erosion mechanisms.

Examination of Eroded Surfaces

The impacted surfaces were examined to identify the damage and material removal processes and any changes which occur from the brittle to ductile transition. Figure 10 shows a typical example of damage produced by a single 273 micron particle traveling at 153 mps on 1095 steel tempered to maximum hardness. The specimen was etched after impact to assess changes in microstructure. The appearance of the damage suggests a highly viscous state during impact with extrusion of the metal into lips around the impact crater. Features normally associated with brittle or elastic fracture such as cleavage facets and cracks are not present. There is also a lack of features characteristic of ductile fracture such as dimpled structure. Although the fine grained martensitic structure is maintained in some areas of the crater floor, examination of the lips at higher magnification reveals an altered microstructure. The lip and matrix structure are shown in Figure 11. The light etching structure of the lip is characteristic of both a high degree of

20

Figure 10.

Single Particle Impact Damage on Fully Hardened 1095 Steel Produced by 273 Micron Particle Traveling at 152 mps and Impacting at 90 Degrees

plastic strain and untempered martensite. If the structure is untempered martensite, then the material in the lip reached a temperature beyond the austenizing temperature of about 700°C.

Figure 12 shows an impact site produced by a 273 micron particle impinging at 90 degrees and traveling at 61 mps. The specimen has been tempered to maximum hardness. The appearance of the damage is the same as that produced by the higher velcity particle (Fig. 10) although less tearing of the metal has occurred. Also, there is no significant difference in size of the damaged area between the two impacts, although erosion weight loss varies by an order of magnitude.

Figure 13 shows an impact site produced by 273 micron particle impinging at 90 degrees and traveling 61 mps on a specimen tempered to Rc30 hardness. The type of damage produced in this lower flow stress material is significantly different than that produced in the maximum hardness material. In the crater floor, flow initiated in many localized regions. Also, material was not extruded out of the crater to form a lip, as is observed with the fully hardened material. Rather, material flow is exhibited significantly beyond the impact site. Consequently, the area of target exhibiting plastic strain is much larger in the softer material.

The difference in erosion weight loss (factor of three) between these two heat treat conditions may be accounted for by the difference in the damage produced. It has been proposed that a major material removal mechanism in erosion of metals is the fracture and removal of the highly strained lips by subsequent impacts (Ref. 3). Assuming this is a major mechanism, then erosion would certainly be reduced under conditions where shear lip formation is minimized.

a) Ridge Pushed Up By Impact
    Showing Lack of Structure
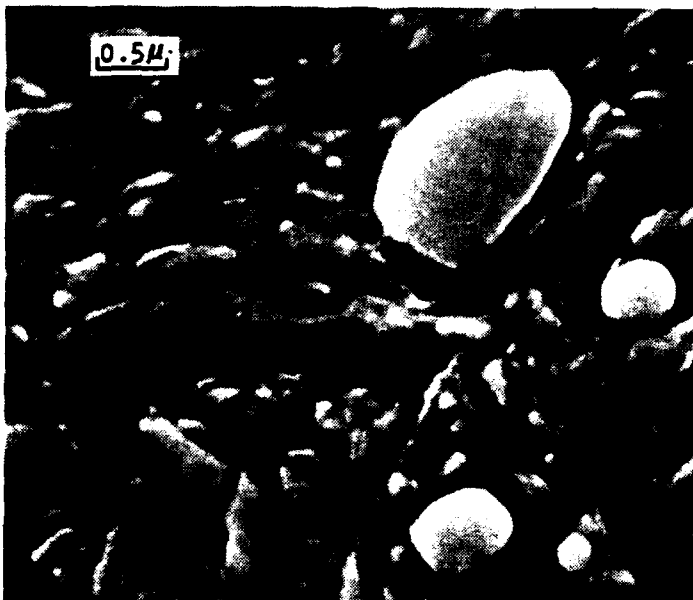
b) Undamaged Surface Struc-
    ture Showing Fine
    Grained Martensite and
    Carbide Particles

Figure 11. Etched Structure of Localized Regions From Figure 10

The results of Figure 9 show a large difference in erosion weight loss (nearly
one order of magnitude) between the 1095 steel tempered for maximum hardness
and a hardness of Rc30 when eroded with 940 micron SiC particles at 90 degrees
impingement. Erosion damage was characterized for these targets to determine
the changes occurring with the brittle to ductile erosion weight loss transi-

22
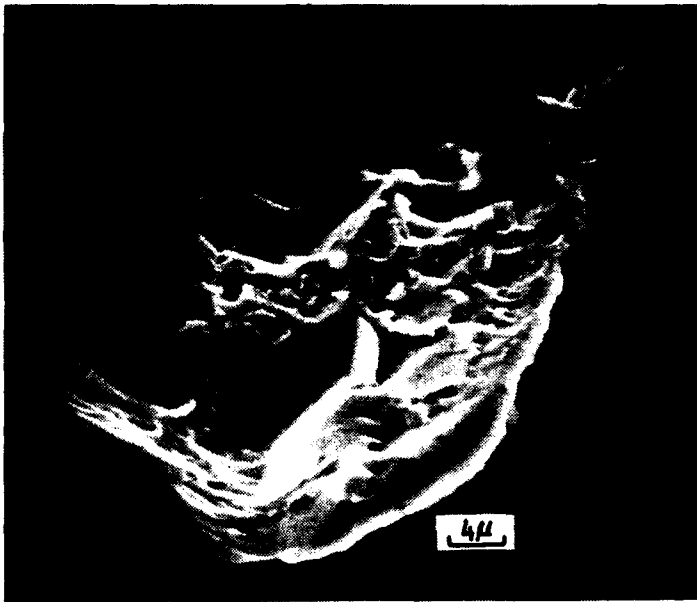
Figure 12.

Single Particle Impacting
Damage on Fully Hardened
1095 Steel Produced by 273
Micron Particle Traveling
at 61 mps and Impacting
at 90 Degrees
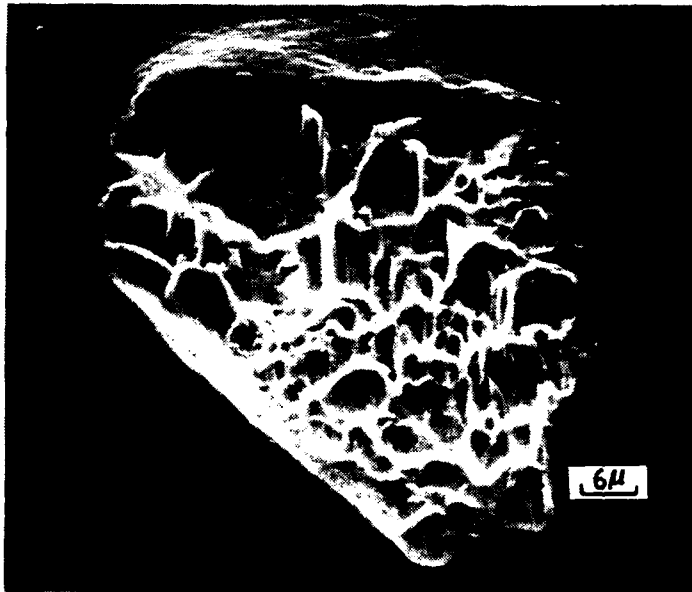
Figure 13.

Single Particle Impact
Damage on 1095 Steel
Tempered to RC30 Hardness
Produced by 273 Micron
Particle Traveling at 61
mps and Impacting at 90
Degrees

tion. Figure 14 shows a cross section of the eroded surfaces. The primary
difference between the two temper conditions is the greater depth of damage
produced in the Rc30 temper material. Also, a white etching phase (indicated
by an arrow) is observed subsurface on the maximum hardness temper material,
and is not observed on the softer target.

23
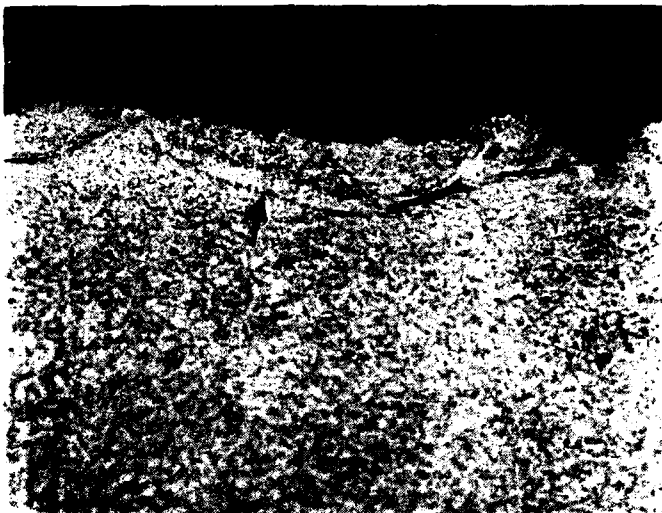
A. Maximum Hardness Temper

B. Temper to Rc 30 Hardness

Figure 14. Cross Section Showing Eroded Surface After Impact With
940 Micron SiC, 132 mps Velocity, 90-Degree Impingement.
Magnification: 500X

The specimens shown in Figure 14 were also examined in the SEM to further
characterize the damage. Fragments of SiC particles were found embedded
below the surface of the soft, low flow stress Rc30 hardness material. This
is shown in Figure 15 (same area as Fig. 14B) where the silicon X-ray dot map
reveals high concentrations of silicon in the subsurface damage regions.
Silicon was not observed subsurface on the maximum hardness, high flow stress
target. Although the additional weight of embedded SiC particle fragments
will reduce the measured erosion weight loss, the amount of SiC particles
necessary to account for the one order of magnitude difference in erosion
weight loss is much greater than observed. It is concluded that embedded SiC
particles in the soft target is not a primary cause of the reduced erosion
for this target.
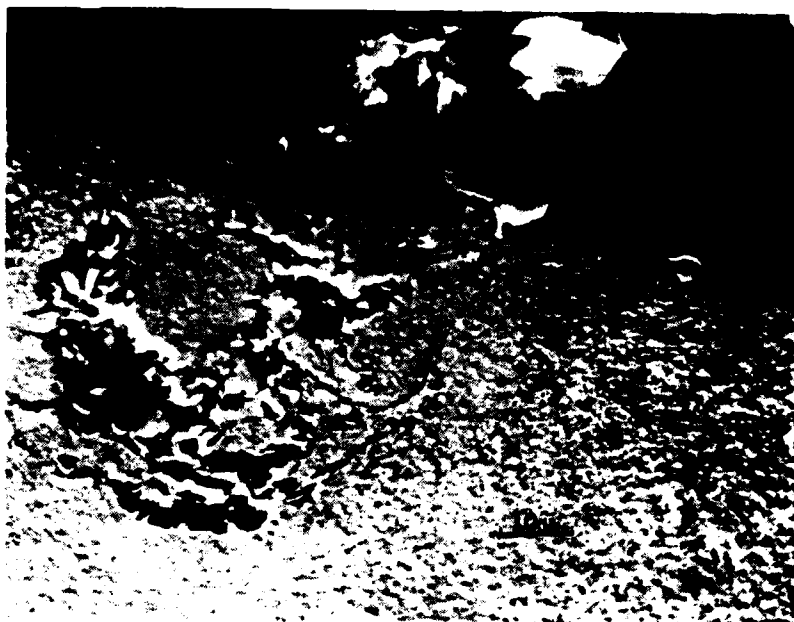
A. Secondary Electron Image
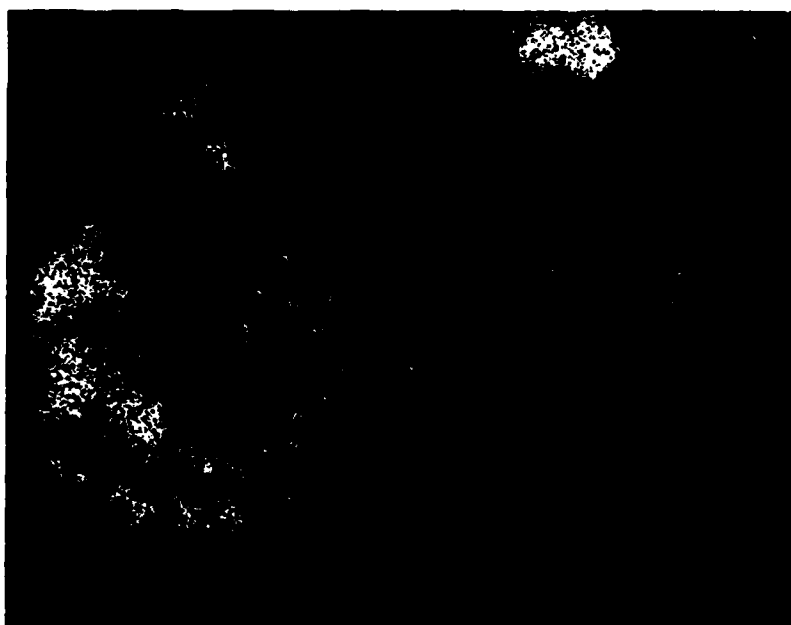
B. Si X-Ray Dot Map

Figure 15. SEM and Silicon X-Ray Images of Eroded Surface Cross Section (Temper to Rc 30 Hardness, 940 Micron SiC Impact, 132 mps Velocity, 90-Degree Impingement) Same Area as Shown in Figure 14B)

There are significant differences between the type of single impact damage observed by 940 micron SiC particles on the maximum hardness target (high flow stress) compared with material tempered to Rc30 (low flow stress).

Typical examples for the two targets are shown in Figure 16. It was originally expected that the very hard targets which exhibited brittle type erosion would exhibit brittle fracture characteristics, such as cleavage facets and cracks, on impact; since, the high hardness material exhibits very little, if any, ductility during standard tensile tests. However, as seen in Figure 16A, significant plastic deformation accompanies solid particle impact. Material is extruded out of the impact crater to form lips around the crater. Also, ledges are formed which originate within the crater and still retain the polishing scratches on the surface, i.e., no deformation has occurred on the ledge surface. There is essentially no apparent deformation of the target surface outside of the immediate area of the impact area. This latter observation is not unexpected due to the inherently high flow stress of this material.

The appearance of single particle damage on the softer, lower flow stress Rc30 hardness target is entirely different (Fig. 16B). Instead of shear lip formation, the particle impact pushes the adjacent target material away so that plastic flow is exhibited significantly beyond the impact site. Consequently, the material exhibiting plastic strain is much larger in the softer material; however, the total strain reached by localized areas is greater in the high hardness target (extruded lips). Although not shown, plastic strain initiates at many localized regions on the crater floor on the soft target.

These differences in impact damage between the hard and soft targets are consistent with that observed for quartz particle impact (Ref. 17). Although the hard targets exhibit brittle type erosion, as evidenced by maximum erosion at 90 degrees, the deformation mechanisms are not brittle but exhibit a high degree of plasticity.

The prior discussion of single impact damage dealt with differences due to target flow stress or hardness for a single impact condition. Differences in impact damage also occur with varying particle size for a given heat treatment. Average strain rate during impact is directly dependent on the inverse of particle size. Figure 17 shows typical single impacts for particles ranging from 940 to 10 microns, which also covers a two order of magnitude variation in the strain rate. The general characteristics of the impacts are the same, i.e., shear lip formation around the impact crater. However, the apparent viscosity of the target during impact varies with particle size. For impact with the largest particle (Figs. 16A and 17A) the shear lips exhibit tearing and still retain surface markings. For impact with 273 micron particles the appearance of the crater and lips suggest a viscous state during impact. The lack of markings on the lips suggests that material was hot enough during impact for surface diffusion to occur. This specimen was etched after erosion to detect changes in microstructure. The fine grained martensite structure of the matrix is retained in some areas on the crater floor but the lip material etches much lighter and is similar in appearance to the subsurface transformation bands shown previously (Fig. 14A). The impact crater produced by 10 micron particles at this low velocity (61 mps) is very small, but the damage is consistent with that produced by the larger particles. In this case the viscous metal appears to have flowed beyond the crater lip. The results indicate an increase in plasticity or temperature rise on impact with decreasing particle size.

A. Rc 66 Hardness
   (maximum hardness
   temper)

B. Rc 30 Hardness
   Temper

Figure 16. Typical Single Impacts on 1095 Steel Target Produced by
            940 Micron SiC Particles Traveling at 132 mps and
            Impinging at 90 Degrees

Small spherical iron particles have been observed adjacent to impact areas
produced by 273 micron particles on the maximum hardness targets. They
were not observed on the softer targets. Figure 18 shows an example of
the particles, which is indicated by "b". Energy dispersive X-ray analysis

27
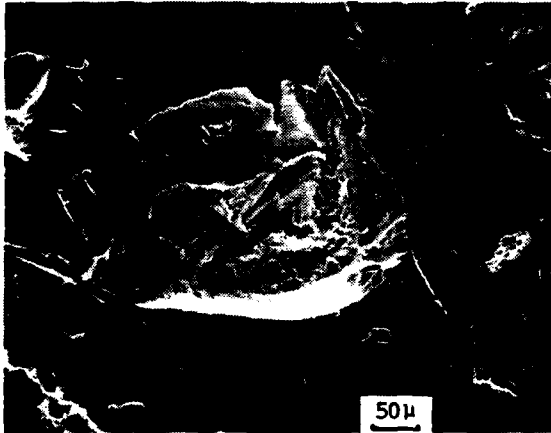
Impact Due to

A. 940 Micron SiC Particle
   132 mps Velocity

B. 273 Micron Quartz Particle
   152 mps Velocity

C. 10 Micron Quartz Particle
   60 mps Velocity

Figure 17.   Single Impact Damage 1095 Steel Heat Treated to Maximum
             Hardness 90 Degree Impingement

Figure 18.

Detail of Single Particle Impact Damage Showing Iron Base Particle (b) Adjacent to Impact Site

revealed iron to be the only detectable element present in this particle. No silicon was present and carbon is below the detectable limit of the analyzer. The particle presumably detached during impact and deposited back on the target surface. The particle has no defineable structure. The spherical shape of the particle suggests that it was sufficiently hot to melt or to allow rapid surface diffusion to approach an equilibrium spherical shape. A particle fractured from the surface is expected to be more angular, i.e., temperature increase insufficient to cause significant surface diffusion. The volume of this particle compared with the volume of material lost per impact (calculated from weight loss data) indicates that ejection of several hundred of these particles from a single impact would be necessary to account for the erosion. This seems highly unlikely and suggests that if localized temperature excursions during impact do exceed the melting point, that melting as droplet ejecta of this size is not the only mechanism of erosion weight loss under these test conditions.

The white etching phase shown in Figure 14A is also observed under certain other impact and heat treat conditions. Figure 19 shows appreciable subsurface white etching layer on a target treated to maximum fracture toughness impacted with 163 micron particles traveling at 153 mps velocity. This white layer is thought to be transformed material and has also been observed under some conditions of abrasive wear where bands occur beneath the ground surface (Ref. 18). The bands are caused by an accumulation of plastic strain following local yielding at a depth where the maximum shear stress is attained. The white etching bands have also been observed after high speed (10^2/sec) torsion tests of AMS 6418 steel and are attributed to adiabatic shear bands where the shear instability is so severe as to form narrow transformed regions (Ref. 19). Considering the high strain rates involved during solid particle

Figure 19.

1095 Steel Heat Treated to
Maximum Fracture Toughness.
Erosion Conditions: 163
Micron Particles, 153 mps
Velocity, 90-Degree Impinge-
ment.

(Arrows indicate transforma-
tion bands)

Magnification: 1000X

impact, the white etching bands are also probably due to transformation
produced by adiabatic heating at a depth of maximum shear.

In Figure 19, carbide particles are seen in the transformation bands, suggest-
ing that adiabatic heating was sufficient to transform the matrix martensite;
but was not sufficient to dissolve the carbide particles. These transforma-
tion bands are evidence that adiabatic heating exceeded 800°C (1472°F) which
is the austenite transformation temperature for this alloy. The targets
tempered to hardness below Rc 64 did not exhibit transformation products, nor
did material heat treated to have a coarse grained pearlite structure (Fig.
20). Figure 21 shows an example where both a transformation band (1) and a
cracked deformation band (2) exist. The length of these regions are approxi-
mately an order of magnitude less than the particle diameter. It is possible
that particle orientation during impact is responsible for the deformation or
transformation which occurs, e.g., the highest energy density and greatest
potential for adiabatic heating occurs when the angular particles impact on a
corner.

Figure 20.

1095 Steel in Pearlitic
Condition.
Erosion Conditions:
273 Micron Particles, 153
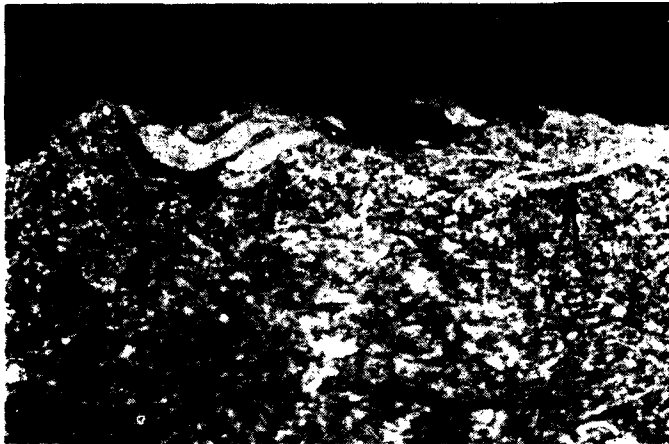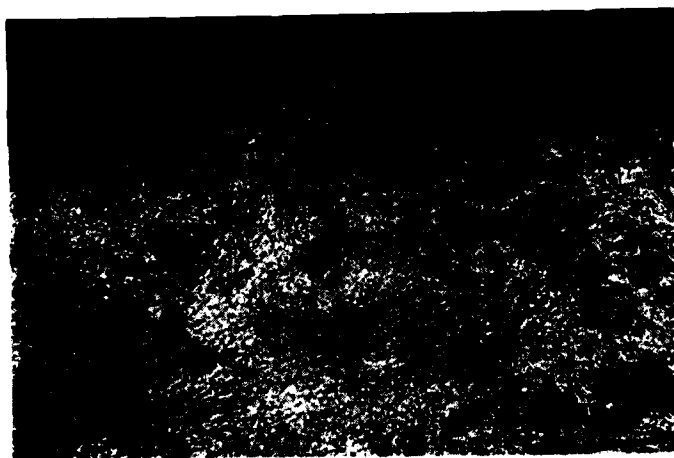mps Velocity, 90-Degree
Impingement.

Magnification: 1000X

30

Figure 21.

1095 Steel Treated to Maximum Hardness.
Erosion Conditions: 385 Micron Particles, 153 mps Velocity, 90-Degree Impingement.

(Arrow 1 indicates transformation band, arrow 2 indicates cracked deformation band)

Magnification: 1000X

An explanation for the greater erosion of the hard targets at 90 degrees compared with the soft targets may be that the material bounded by the surface and the cracks is removed by a subsequent impact. In Figure 21, this volume is approximately 7×10^{-9} cm^3. The volume loss per impact calculated on an erosion weight loss basis is approximately 1×10^{-8} cm^3. Similar calculations for impact with 940 micron SiC on hard targets gives 5×10^{-8} cm^3 for volume of the cracked region compared with 9×10^{-8} cm^3 for volume loss based on erosion weight loss. Considering the assumptions made in these calculations, this is considered quite good agreement and supports the premise that the greater material removal at 90 degree impingement angle for the hard targets is due, at least in part, to removal of the subsurface laterally cracked material.

The reduced erosion exhibited by the material tempered into the temper embrittlement region may be due to the fact that the transformation bands are very near the surface and very few cracked deformation bands occur, e.g., the volume encompassed by the cracked regions is small compared with the other hard targets.

Examination of Erosion Debris

To further elucidate the role of impacting particle size on degree of adiabatic heating, erosion products were collected after erosion with 940 micron SiC, and 273 and 10 micron quartz particles on maximum hardness targets. This was accomplished by placing a magnet beneath the target. Figure 22 shows examples of the debris produced by the three erosion conditions. The appearance of the erosion debris is consistent with the appearance of the single impact damage (Fig. 17) in that the apparent plasticity increases with decreasing particle size. For impact with 940 micron SiC, wear marks are apparent on the surface (Fig. 22A). Although plastic deformation has occurred, adiabatic heating was not sufficient to allow surface diffusion so that surface markings still remain. This particular example looks more like a

31
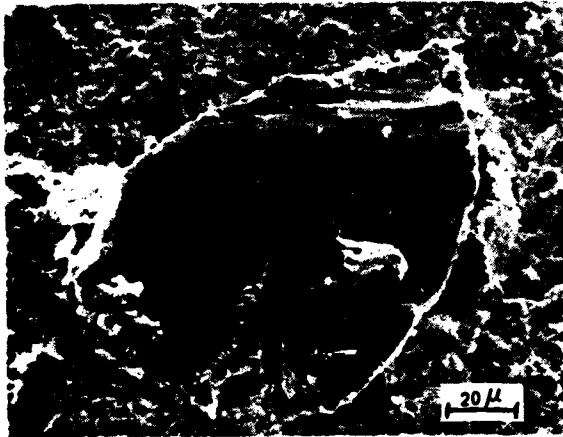
Impact Conditions

A. 940 Micron SiC,
    132 mps

B. 273 Micron Quartz,
    153 mps

C. 10 Micron Quartz
    153 mps

    Arrow Indicates
    Iron Particle

Figure 22. Eroded Steel Particles From Maximum Hardness Targets,
            90° Impingement

detached shear lip than subsurface laterally cracked material. The volume of this fragment (2×10^{-7} cm^3) is also consistent with both.

The fragments shown in Figure 22B and 22C are more rounded and lack mechanical markings, suggesting that the temperature reached was at least sufficient for significant surface diffusion. There is no clear evidence of molten erosion products. Since erosion with 10 micron particles produces the highest average strain rates, this condition is the most likely to cause melting. The erosion fragments are so small (approx. one micron) it is difficult to ascertain specific details.

Evidence of melting in the form of discrete spherical iron particles attached to the target surface after erosion have been observed. Examination of erosion debris particles confirm the existence of melting during erosion. Small spherical drops of iron (determined by scanning electron microscope [SEM] - X-ray analysis) are routinely observed attached to the much larger erosion debris particles on targets heat treated to high hardness levels. An example is shown in Figure 23. In addition to the spherical droplets other evidence of melting or incipient melting is seen in the flatish droplets on the surface. In this particular case, molten material per se does not contribute significantly to erosion weight loss, but may contribute to the liklihood that the erosion debris particle will detach from the target. The melting may occur during particle impact due to adiabatic heating in the subsurface maximum shear stress band (corresponds to transformation and deformation zones seen in cross section) or as the erosion debris particles detach due to adiabatic plastic deformation and friction.

Additional evidence of significant adiabatic heating in the hard 1095 steel targets exists in the form of the dimpled structure observed on erosion debris particles. An example is shown in Figure 24. This dimpled structure is typical of ductile overload fracture and would not be expected on fracture surfaces of the low ductility as-heat treated material.

The formation of subsurface transformation bands (Fig. 25), indicative of temperature excursions to at least 800°C, is a function of both heat treatment and impacting particle size. Prerequisites for transformation are a certain high level of initial flow stress or hardness combined with sufficient particle kinetic energy. For example, after erosion with 385 micron quartz particles traveling at 150 mps, transformation bands are observed in targets of hardness as low as Rc 50 and all harder targets. On the hardest target (treated to Rc 66) transformation bands are observed after erosion with particles $\geq$163 microns. Smaller particles do not produce transformation or deformation bands.

Erosion as a Function of the Number of Impacting Particles

It was shown previously, through examination of single impacts, that although the high hardness targets exhibited maximum erosion at 90 degrees which is characteristic of brittle materials, the impact damage was not brittle, but exhibited a high degree of plastic deformation. The damage is characterized

33
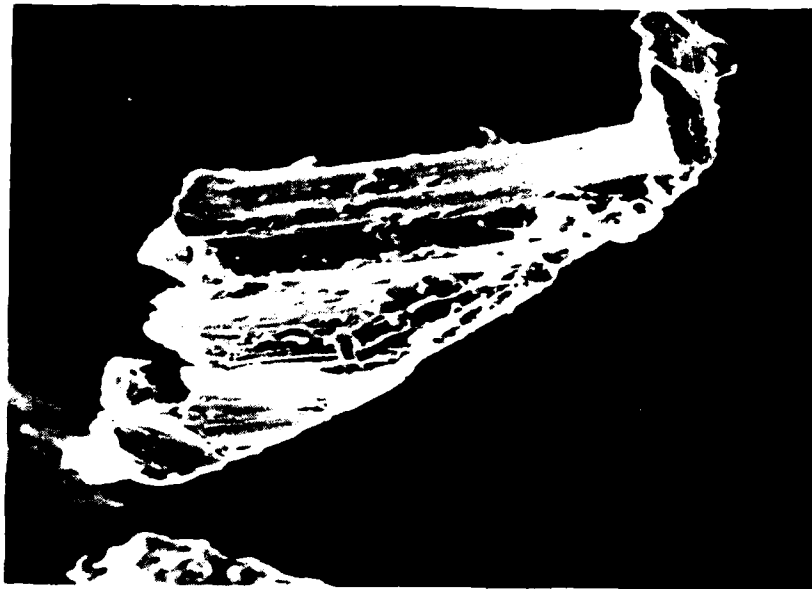
A. Erosion Debris Particle (Magnification: 660X)
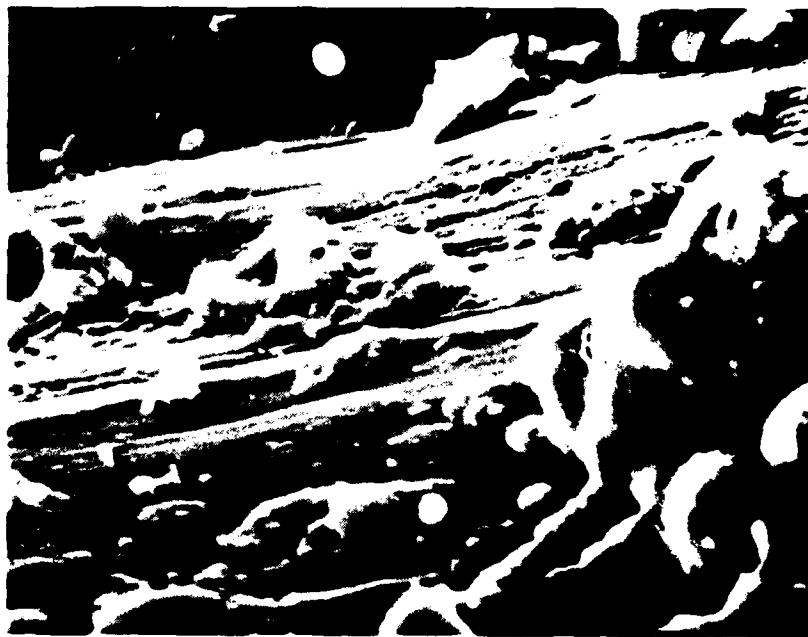
B. Details on Surface. Spherical Droplets are Evidence of
Melting During Erosion. (Magnification: 5350X)

Figure 23. Erosion Debris Particle From 940 Micron SiC Impact at 90-Degree
Impingement and 132 mps 1095 Steel Target Heat Treated to
Maximum Hardness

Figure 24. Dimpled Structure Characteristic of Ductile Overload Fracture
Observed on Erosion Debris Particle From 1095 Steel Target in
Maximum Hardness Condition. Erosion Condition - 940 Micron
SiC, 90-Degree Impingement, 132 mps Velocity. (Mag: 10,000X)

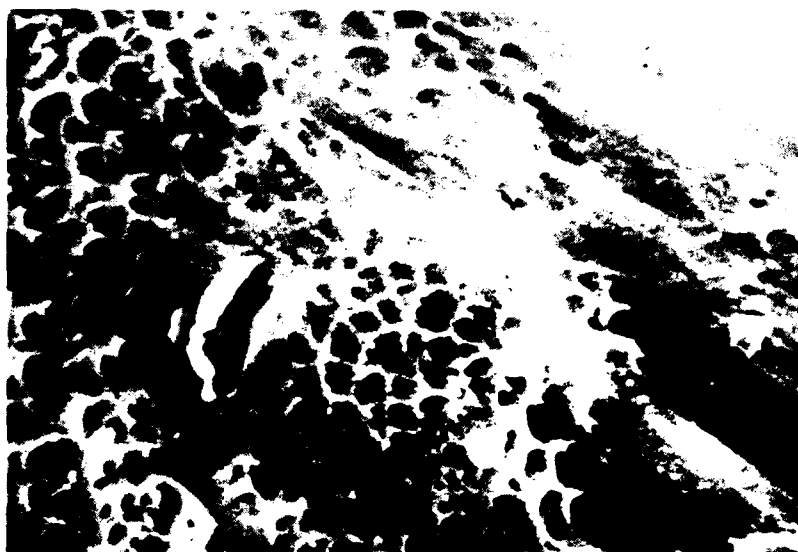by shear lips extruded out of the impact crater. This shear lip formation
was minimized in the softer targets. A possible reason for the up to eight-
fold greater erosion exhibited by the high hardness targets is that the shear
lips are more easily removed by subsequent impacts. To investigate this
premise, Rc 66 and Rc 30 hardness targets were eroded successively with 0.432
grams of 273 micron quartz. This weight of dust corresponds to the number of
particles required to just cover the surface with single impact damage and
was arrived at by dividing the erosion area by the average area damaged by a
single particle. The results of this test are shown in Figure 26. Figure 26
(top) shows weight loss per test and (bottom) shows cumulative weight loss.
On the hard material there is no abrupt increase in weight loss for the second
test, as would be expected if shear lip removal was entirely responsible for
increased erosion. For both the soft and hard targets, there is a gradual
increase in weight loss with successive tests. However, the weight loss of
the soft material appears to have leveled off after approximately six expo-
sures, whereas the hard materials per exposure weight loss is still slowly
increasing after twelve exposures. This may indicate that the formation of
shear lips increase with substrate damage in the hardened material and that
the material removal rate does not saturate until the substrate has received
sufficient damage.

2.1.4 Erosion of Nonferrous Targets

To compliment the erosion work on steels, several materials, including pure
metals, binary alloys, intermetallic compounds and commercial aluminum were

35

A. Rc 48, 385 Micron Quartz,
90-Degree Impingement,
152 mps Velocity

B. Rc 21, 273 Micron Quartz,
90-Degree Impingement,
152 mps Velocity

Figure 25. Optical Micrographs of 1095 Steel Showing Subsurface
Transformation Band Indicative of High Temperature
Exposure (Magnification: 1000X)

erosion tested under various conditions. The results of erosion testing the
various materials will follow.

Erosion of Alpha Ti₃Al

Erosion of alpha Ti_3Al was investigated because it is of engineering interest
to the Air Force for use in gas turbine engines and because the limited duc-
tility of this material makes it a potential candidate to study the ductile
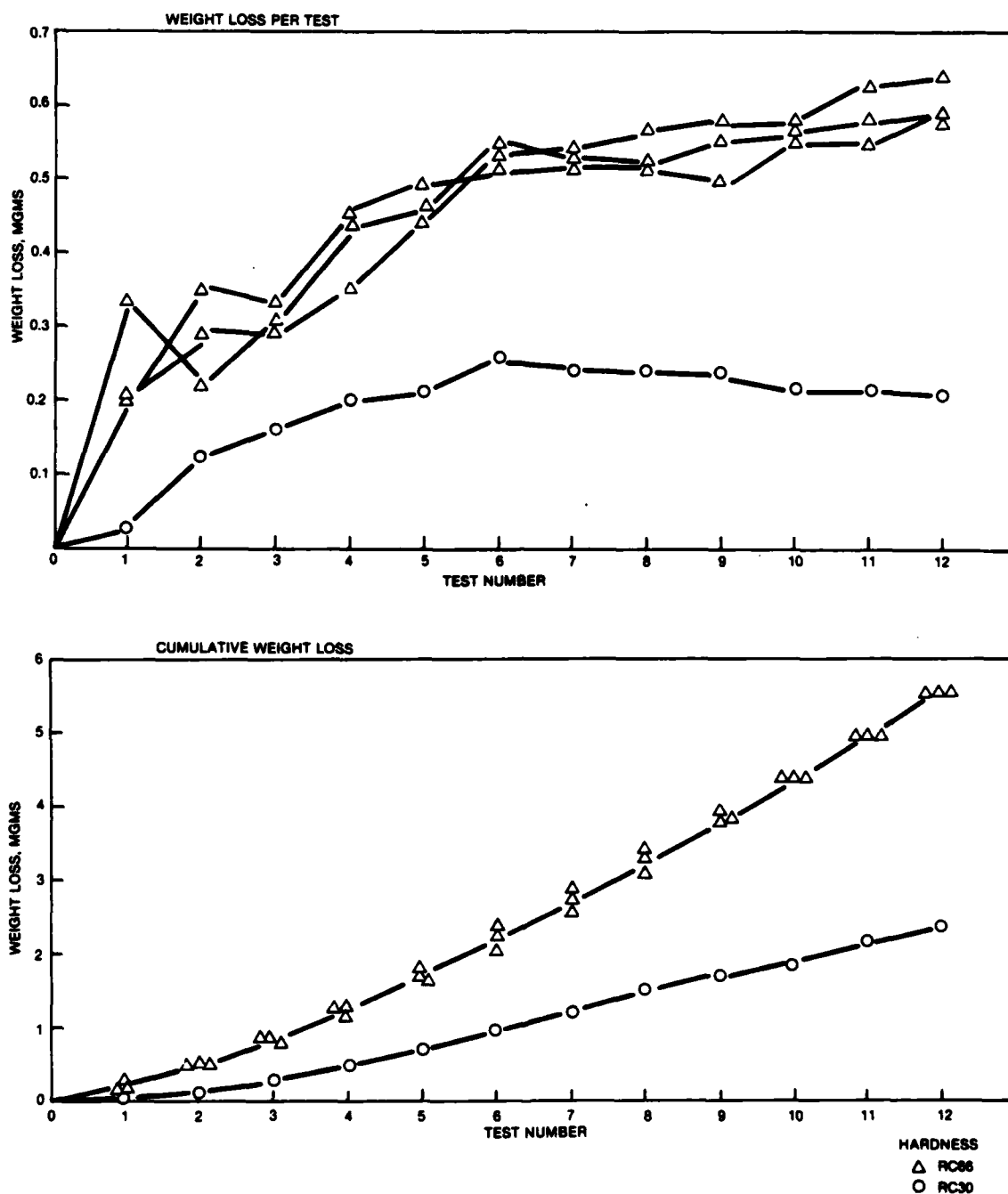
Figure 26. Erosion of 1095 Steel Targets Impacted With 273 Micron Particles to Just Cover the Surface With Impact Damage One Layer Deep For Each Test

to brittle erosion transition. Sheet specimens, code TiMet heat No. V5706, BL rolling process, were provided by Pratt & Whitney Aircraft. Composition of the alloy is 14.5Al-21.5Nb-0.15Si-64.85Ti. The specimens are reported to have textured ductility (in tension) ranging from 0.2 percent in the short axis of the 1 inch by 2 inch specimens to 1.5 percent in the long axis. Ductility increases to approximately five percent at 500°F. Tensile fracture is characterized by quasi cleavage with limited plastic deformation. It is also reported that the material is soft in compression and has fatigue strength which exceeds the ultimate tensile strength due to its work hardening ability.

Specimens were eroded in the as-received condition described above and also heat treated to embrittle the structure.

In the as-received heat treat condition, specimens were eroded at 30, 60 and 90 degrees with 385, 273, 115 and 10 micron quartz particles traveling at 153 mps particle velocity. The embrittled material was eroded with 273 micron particles. The results are shown in Figure 27. There is essentially no effect of angle of impingement on erosion weight loss for all particle sizes, i.e., weight loss was the same, within experimental error, for all three angles for a given particle size. Furthermore, the material heat treated to a brittle condition exhibited the same erosion loss as the as-received material.

The erosion weight loss per impact versus particle radius (log.log basis) was plotted (Fig. 28) to determine the exponential radius dependence of erosion. The value is three which is consistent with the value for ductile materials.

The heavily eroded surfaces were examined in cross section. The as-received material is shown in Figure 29. Figure 29A shows quartz particles embedded in the alpha Ti_3Al target. Plastic flow of the target has occurred around the particle. Figure 29B shows another example of plastic flow on the erosion surface. No evidence of brittle fracture or cleavage is apparent. Examination of single impact damage on as-received material also revealed that plastic deformation rather than brittle behavior was typical. An example is shown in Figure 30. Not only is plastic flow exhibited in the actual impact crater, but plastic deformation has also occurred on the surface adjacent to the impact crater, as evidenced by the irregular surface in the upper right area of Figure 30. Cross sections through the eroded surface of embrittled material are shown in Figures 31A and B. In Figure 31A probable transformation is indicated by an arrow in the subsurface shear band. These transformation bands and cracked deformation bands are analogous to those which occur on the hard 1095 steel targets discussed earlier. Figure 31B shows an area on the same specimen which exhibits a high degree of plastic flow.

These results indicate that alpha Ti_3Al behaves in a predominantly ductile erosion mode. The evidence of transformation bands indicates localized temperature excursions into the beta region (approx. 1150°C) due to adiabatic heating on the embrittled material. Transformation bands in titanium alloys have been observed previously during ballistic impact (Ref. 20).
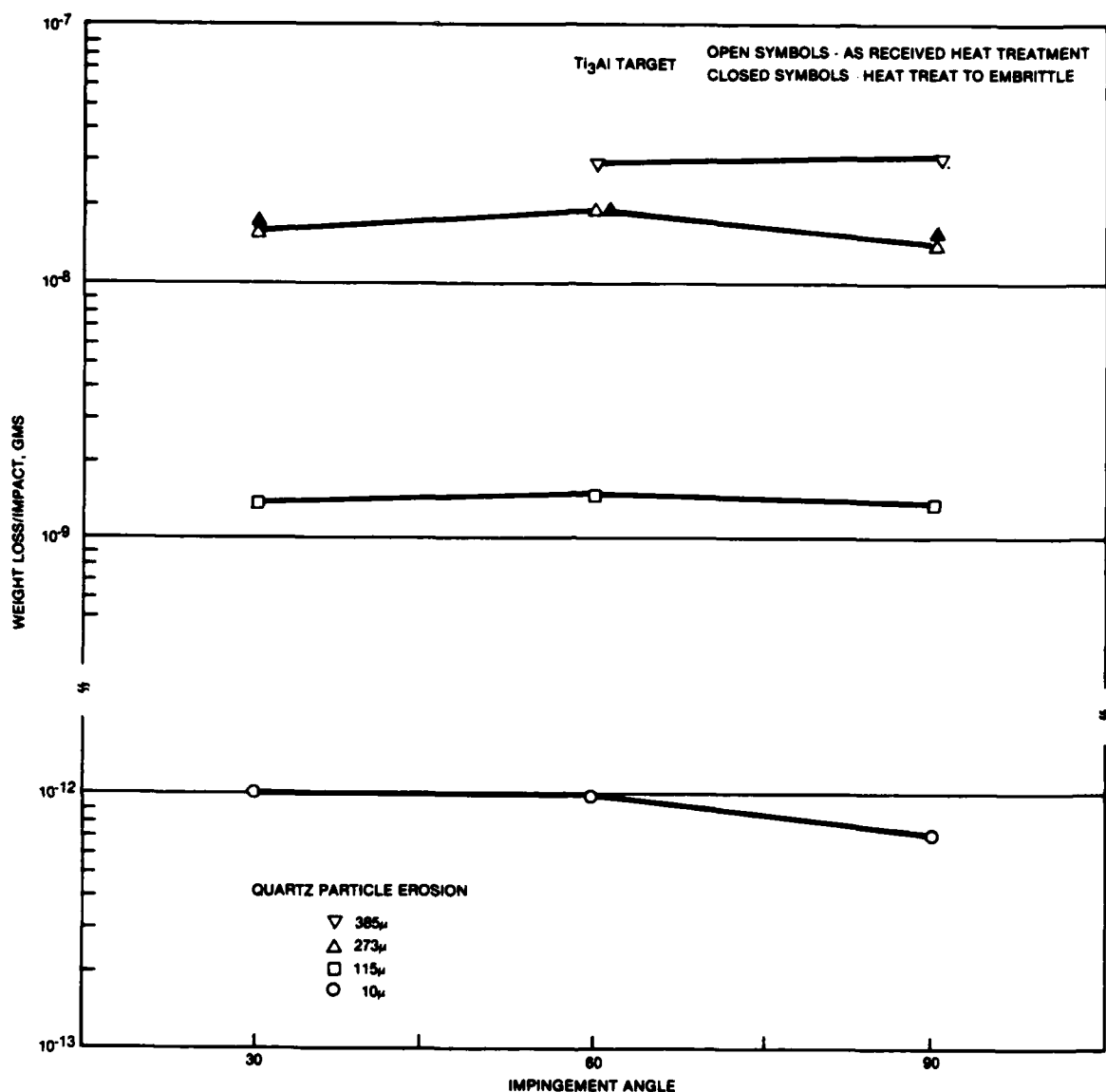
Figure 27. Erosion Weight Loss Per Impact Versus Angle of Impingement
for Alpha Ti₃Al Target. Particle Velocity = 153 mps.

Erosion of Aluminum, Copper, Molybdenum and Gold

2024 aluminum alloy, OFHC copper, pure molybdenum and 24 kt gold targets have
been eroded under various conditions. The 2024 aluminum targets were heat
treated to provide three levels of hardness or flow stress. The erosion
volume loss for 50 grams of dust is shown in Figures 32, 33 and 34 for 940
micron SiC, 273 micron quartz and 10 micron quartz particle impacts. 1095
steel targets in the maximum hardness and Rc 66 heat treatments are also

Figure 28. Particle Size Dependence of Erosion for Alpha Ti₃Al Target

40

A. Embedded Quartz Particles

B. Plastic Flow

Figure 29. Cross Section of Alpha Ti$_3$Al (As-Received) After Erosion With 273 Microns Quartz Particles Traveling at 153 mps, Impinging at 90 Degrees. Magnification: 1000X
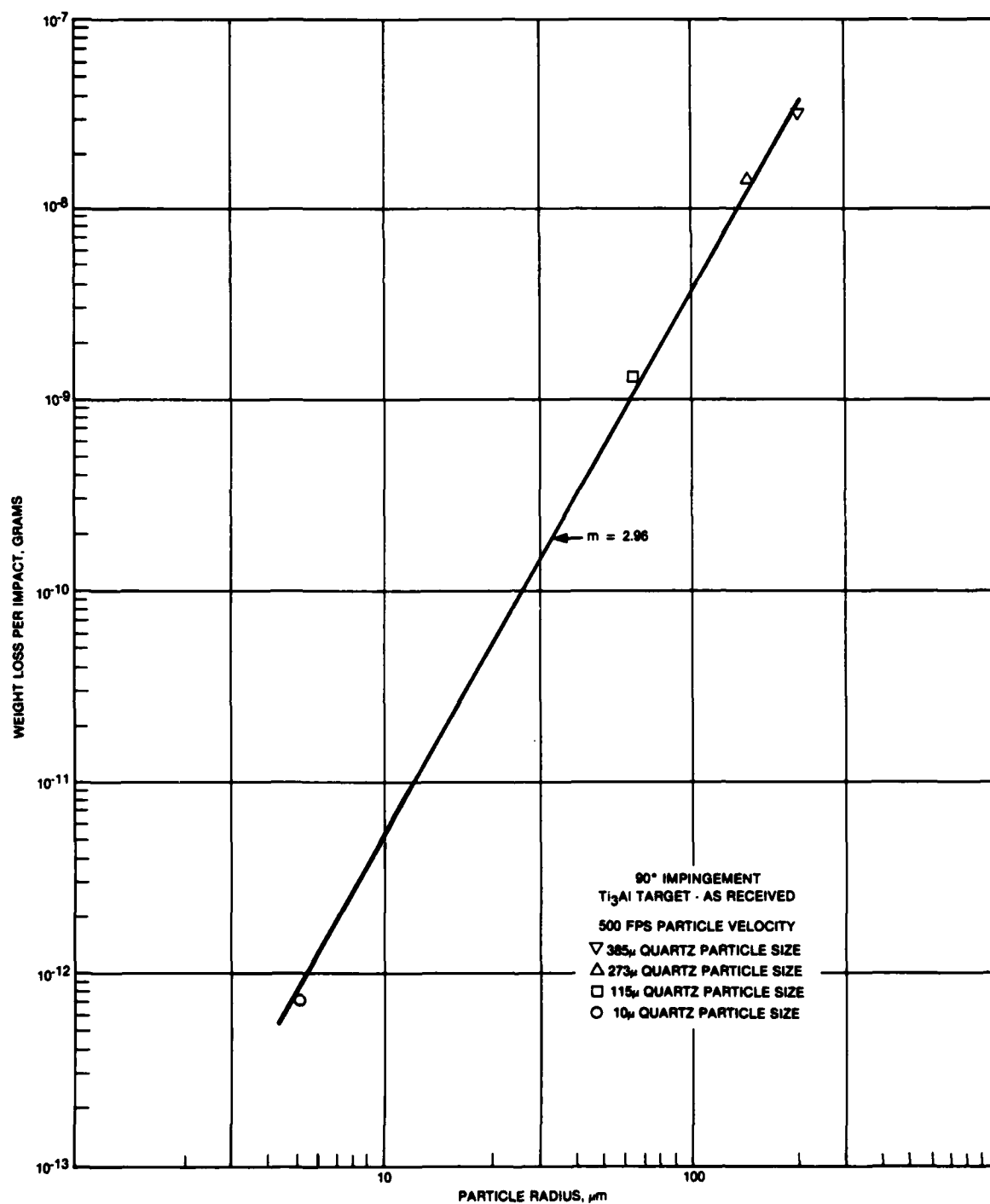
included. All of the new targets exhibited higher erosion at 30-degree than at 90-degree impingement, which is typical of ductile metals. The 2024 aluminum alloy in all three heat treatments generally eroded more than the other targets, and the specimens heat treated to a higher yield or flow stress eroded more than the softer fully annealed aluminum; however, the erosion rate difference between the three alloy conditions becomes less with reduced particle size.

Examples of the subsurface damage produced during erosion of the 2024 aluminum for each of the three microstructural conditions are shown in Figure 35 with the impact conditions of 273 micron particles traveling at 152 mps and at normal incidence. The depth of damage is greater on the soft 2024-0 target but all three show significant damage. Adiabatic heating may lead to some

41

Figure 30.   Single Impact on Alpha Ti₃Al Produced by 273 Micron Quartz at 153 mps Velocity and 90-Degree Impingement Angle. (Note Plastic Flow on Surface Adjacent to Impact Crater - Upper Right of Photograph). Magnification: 1000X

dissolution of the precipitate phase. The surface layer of the specimen shown in Figure 35B indicates a change in microstructure when compared to the bulk material. Due to the extremely fine nature of the precipitate phase (the diameter of the θ' phase is approximately 100 nm), it would be necessary to use transmission electron microscopy to direc   observe the phenomenon.

Of the three pure metals, molybdenum showed the best erosion resistance, copper the worst and gold fell in the middle. Typically, the three pure metals showed better erosion resistance than the 2024 aluminum alloy. Figures 36 and 37 illustrate the type of subsurface damage sustained by the three materials, 2024 aluminum, copper and molybdenum, after erosion by 273 micron quartz particles traveling 152 mps. Significant damage is observed; in fact, the molybdenum having the lowest erosion rate exhibits the greatest extent of damage.

Erosion of Fe-Cr Binary Single Phase Alloys

Pure iron and three Fe-Cr binary alloys were erosion tested to investigate the effect of solid solution strengthening on the erosion behavior. Figure 38 shows the variation of erosion rate and hardness with composition. A ductile erosion response is observed since in each case erosion is greater at 30-degree impingement than at 90-degree impingement. Contrary to the age hard-

42

A. Possible Transformation
   Band Indicated by Arrow
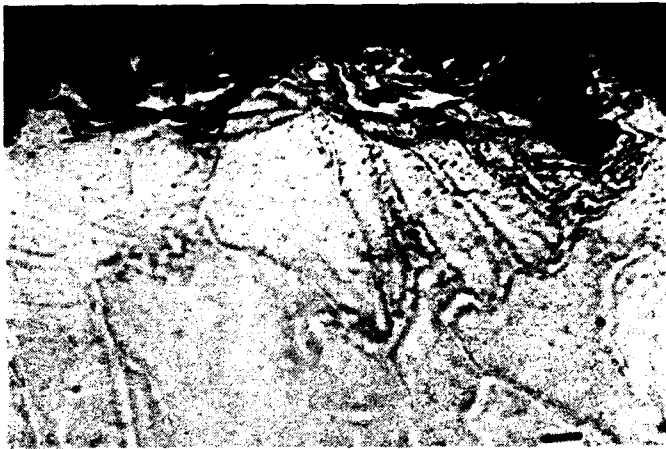
B. Plastic Flow

Figure 31. Cross Section of Alpha Ti$_3$Al Heat Treated to Embrittle After
            Erosion with 273 Micron Quartz Particles Traveling at 153
            mps, Impinging at 90 Degrees. Magnification: 1000X

ened alloys, the solution hardened alloys show improved erosion resistance
with increased hardness.

Single Impacts

Single impact erosion tests were performed on 1095 steel, copper and molyb-
denum targets. Figure 10 shows the impact crater of the 1095 steel target in
the fully hardened condition (Rc 66) and a similar impact crater is shown in
cross-section in Figure 39. Both figures show significant flow is observed,
in fact, a large shear lip is present. Again, this is evidence of an increase
in ductility during the impact event. Figure 40 shows the impact damage of a
copper target after simple impacts with 940, 273 and 10 micron particles. A
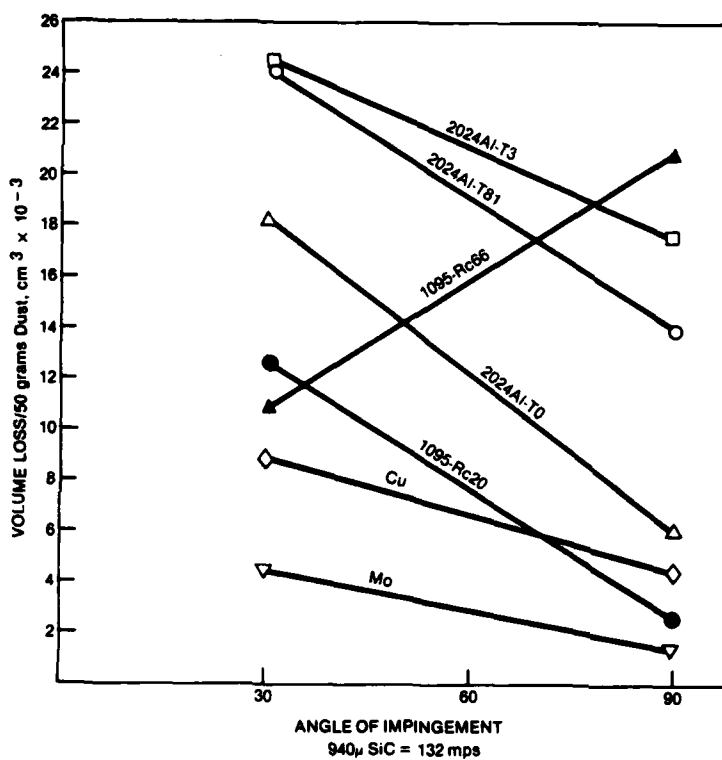
43

Figure 32.

Erosion Loss of
2024Al, 1095 Steel,
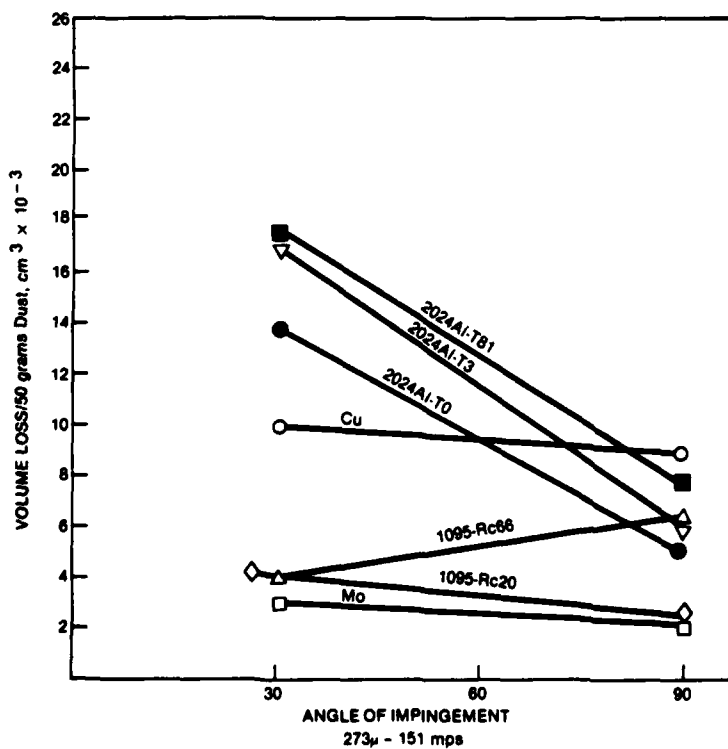Molybdenum and Copper
for 940 Micron SiC
at 132 mps.

Figure 33.

Erosion Loss of
2024Al, 1095 Steel,
Molybdenum and Copper
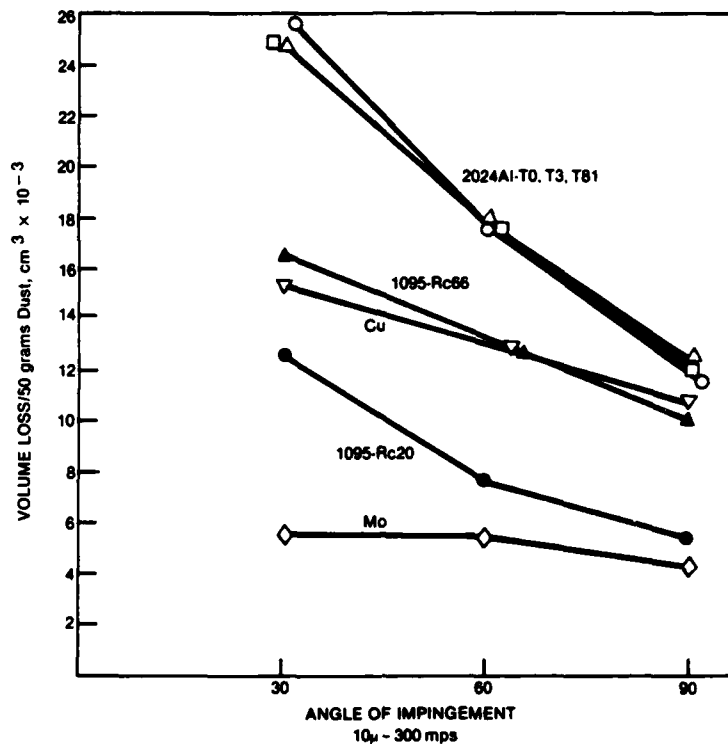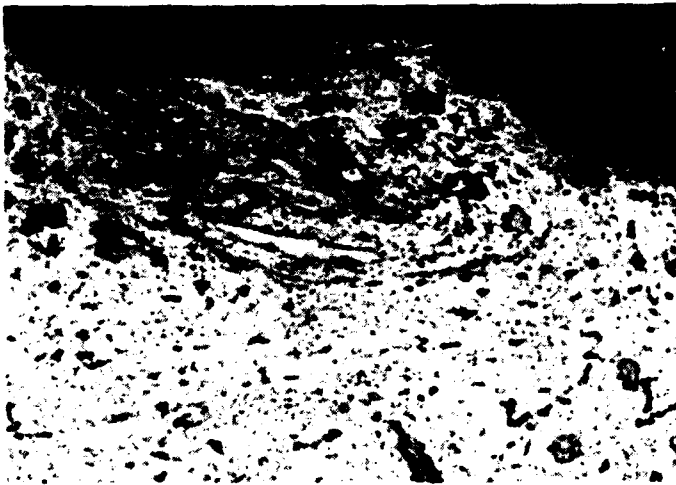for 273 Micron Quartz
at 151 mps

44

Figure 34. Erosin Loss of 2024Al, 1095 Steel, Molybdenum and Copper
for 10 Micron Quartz at 300 mps

great amount of ductility is apparent from the dimpled rupture type of frac-
ture. Shear lips are observed for the 10 micron eroded material but for the
940 and 273 micron material, shear lips were not observed. Similarly, the
molybdenum target, Figure 41, exhibited erosion damage of the same nature as
copper, i.e., dimpled rupture fracture surfaces and limited observations of
shear lips.

2.1.5 Discussion

One of the major objectives of this program was to identify the effects of
adiabatic heating in comparison to the effects of strain rate. Three major
effects are associated with adiabatic heating: localized melting, ductile
fracture of a brittle target material; and formation of subsurface transfor-
mation bands. Melting was observed with the 1095 steel targets in the fully
hardened condition. Ductile, dimpled rupture fracture surfaces were observed
for all eroded materials regardless of their heat treat condition. Transfor-
mation bands were observed as a function of both heat treatment and particle
size. These observations indicate a complex interrelationship between adi-
abatic heating and strain rate. The competing effects of heating and strain
rate are illustrated in Figures 42 and 43 for mild steel and molybdenum
respectively. As the temperature increases the strength decreases for all

45

A. To Heat Treatment
    Rb 7 Hardness
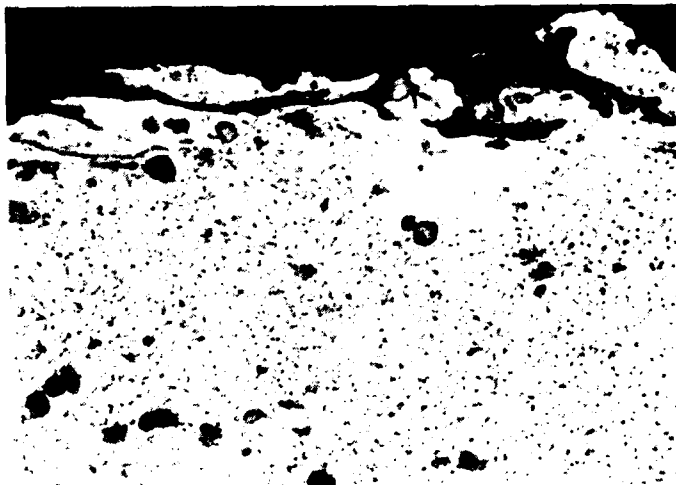
B. T3 Heat Treatment
    Rb 78 Hardness
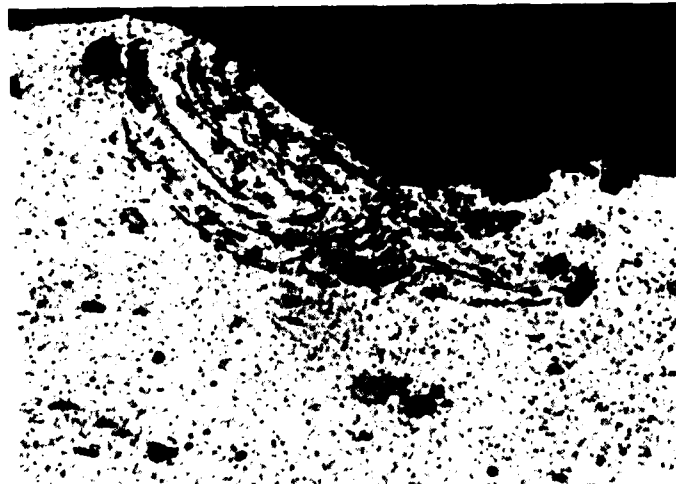
C. T81 Heat Treatment
    Rb 81 Hardness

Figure 35. 2024 Aluminum Alloy Eroded With 273 Micron Quartz at 152 mps,
            90-Degree Impingement (Magnification: 1000X)

46

Figure 36.

Copper Eroded With 273
Micron Quartz at 152 mps,
90-Degree Impingement
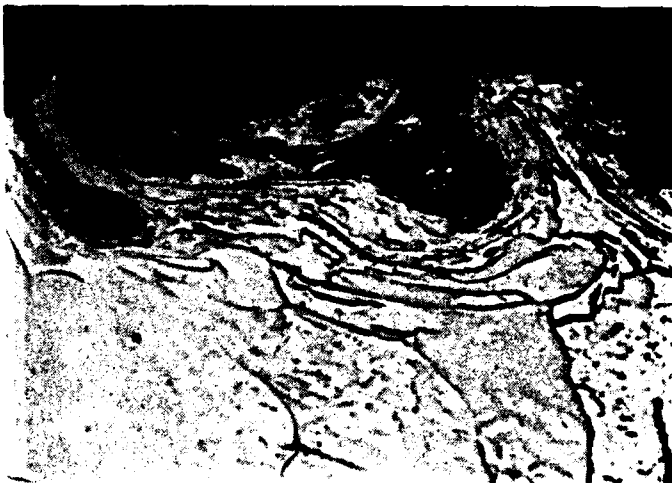
Magnification: 1000X

Figure 37.

Molybdenum Eroded With 273
Micron Quartz at 152 mps,
90-Degree Impingement

Magnification: 1000X

strain rates while increasing the strain rate increases the strength for all temperatures.

Strain rate is a function of both particle size and velocity. The calculation by Hutchings (Ref. 5, Fig. 44) estimated the mean strain rate as a function of both particle size and velocity. The range of particle sizes used in this program varied from 10 to 940 microns and velocities varied from 50 to 1000 mps. This results in a variation of the mean strain rate from 10^4 to 10^7/sec, all well above the strain rates at which mechanical properties are ordinarily measured. This complicates finding a correlation between material property and its erosion resistance. Very little data exists at such high strain rates and the material response during these very brief events of particle impact are not well understood. However, from the data gathered in this program, some comments can be made on strain rates and erosion resistance.
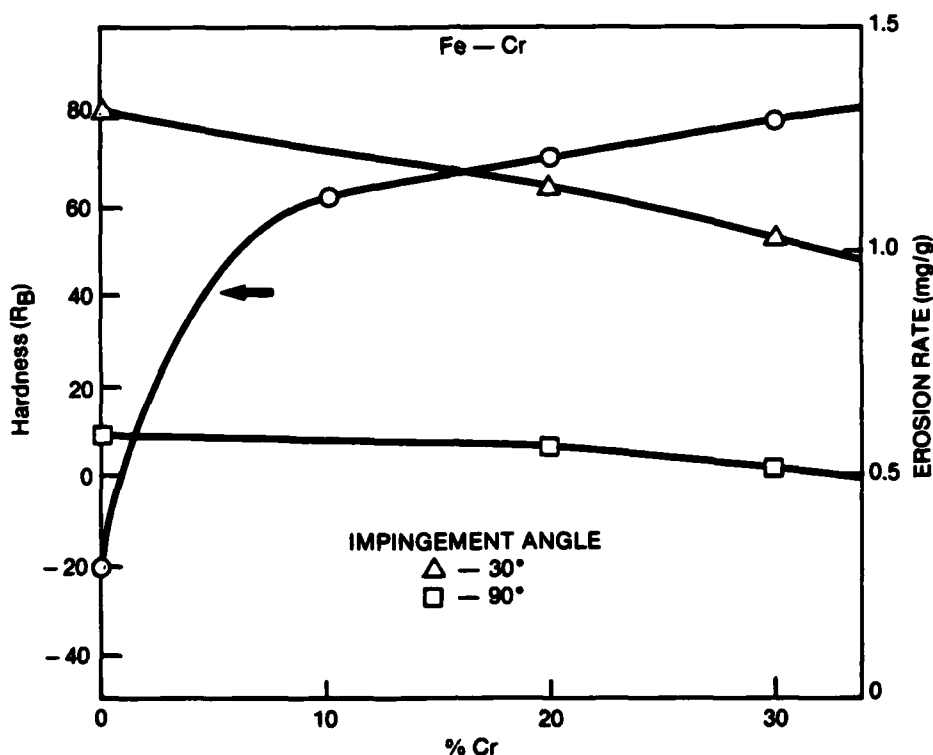
47

Figure 38. Variation of Hardness (Rb) and Erosion Rate With Composition. Erosion Conditions were 273 Micron Quartz Traveling at 188 mps.

Figures 45 through 49 show the erosion data plotted versus the particle size, keeping particle velocity, impact angle and material condition constant. Considering the results shown in Figure 44, the particle size is analogous to strain rate, the 10 micron particle corresponds to a strain rate of approximately 5×10^6/sec, whereas the 940 micron particle corresponds to a strain rate of approximately 5×10^4/sec. For each material tested the erosion rate decreased with decreasing particle size, implying that erosion rate decreases with increasing strain rate. This can be rationalized with the help of Figures 42 and 43. As the strain rate increases the strength of the material increases monotonically. Therefore, at the high strain rates associated with the small particle sizes the dynamic response of the target material results in a stronger, more erosion resistant material.

The influence of material condition as a function of particle size (i.e., strain rate) is demonstrated in Figures 45 and 46. For large particles a large variation in erosion rate occurs with the various heat treat conditions; whereas for the small particles the difference in erosion rate becomes quite small. This could be a reflection of the deformation process as related to strain rate. The large particles with the lower strain rates may behave in a more conventional sense, where microstructure and ordinary hardening mechanisms apply. However, with small particles and very high strain rates those conventional techniques of material processing may not be as important during the deformation event.

A. Magnification: 500X

B. Magnification 1500X

Figure 39. SEM Micrograph of Single Impact Crater in Cross-Section, 1095 Steel Target, Rc 66, 940 Micron SiC Particle, 125 mps, 90-Degree Impingement

49
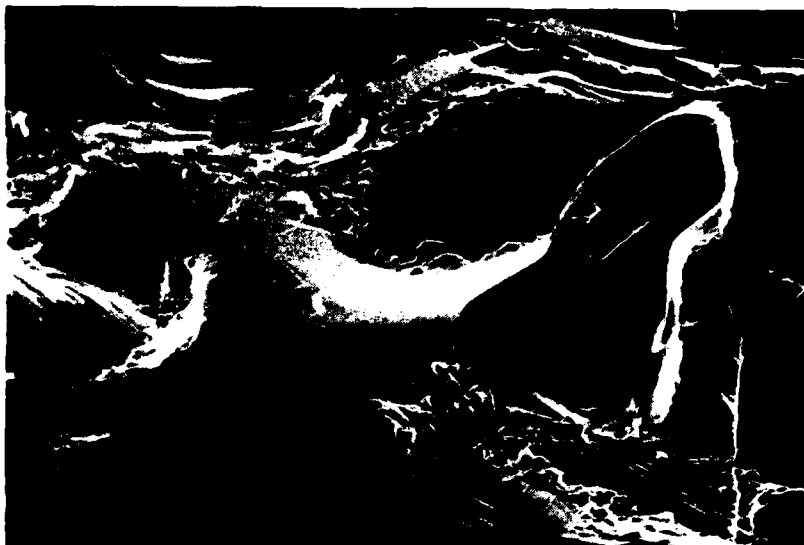
A. 940 Micron SiC

Mag: 300X

B. 273 Micron Sic
Quartz

Mag: 770X

C. 10 Micron
Quartz

Mag: 5500X

Figure 40. SEM Micrographs of Single Impact Craters of a Copper Target

50

A. 940 Micron SiC

   Mag: 200X
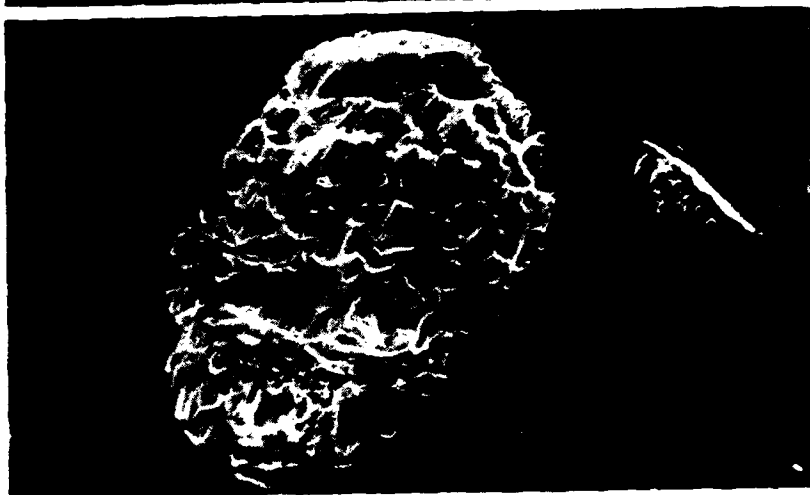
B. 273 Micron Quartz

   Mag: 650X

C. 10 Micron Quartz

   Mag: 6000X

Figure 41. SEM Micrographs of Single Impact Craters of a Molybdenum Target
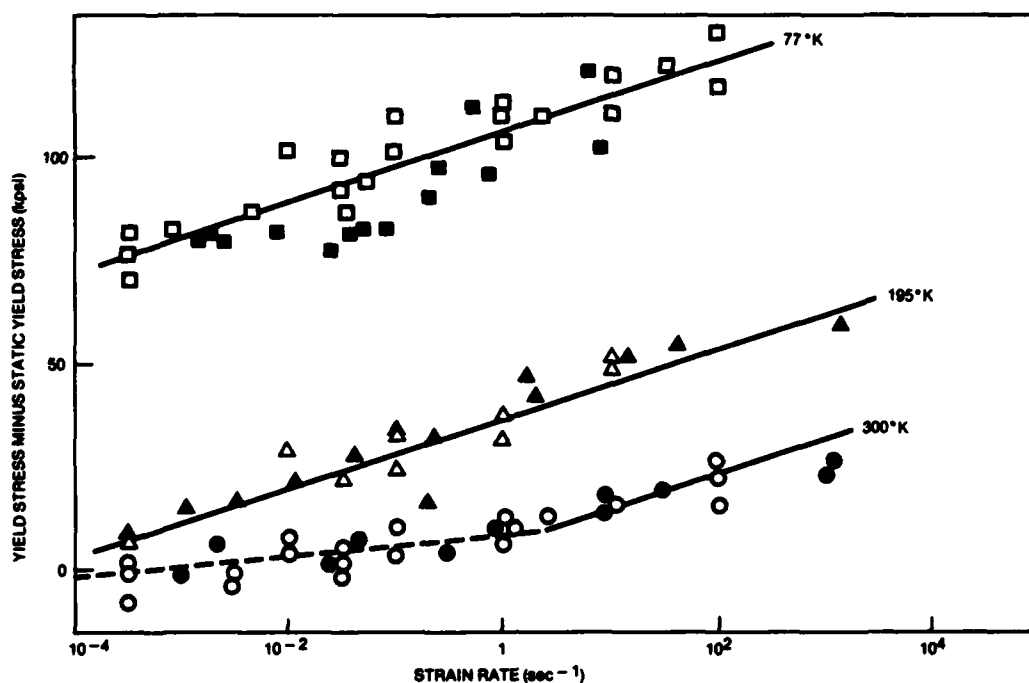
Figure 42. Temperature and Strain Rate Dependence of the Yield Stress of
Mild Steel (Data of Ref. 21, Figure Taken From Ref. 6)

Figure 43. Temperature and Strain Rate Dependence of the Yield Stress of
Molybdenum (Data of Ref. 22, Figure Taken From Ref. 6).

Figure 44.

Estimated Mean Strain Rates Associated With the Impact of Steel Spheres Onto a Steel Surface. Solid Lines, Purely Elastic Behavior; Broken Lines, Perfect Plastic Behavior (Ref. 6)

One final feature associated with the influence of particle size on the erosion rate is the apparent lack of effect of particle size on erosion rate when impingement is at 30 degrees. This is clearly shown in Figure 46 and to a lesser extent i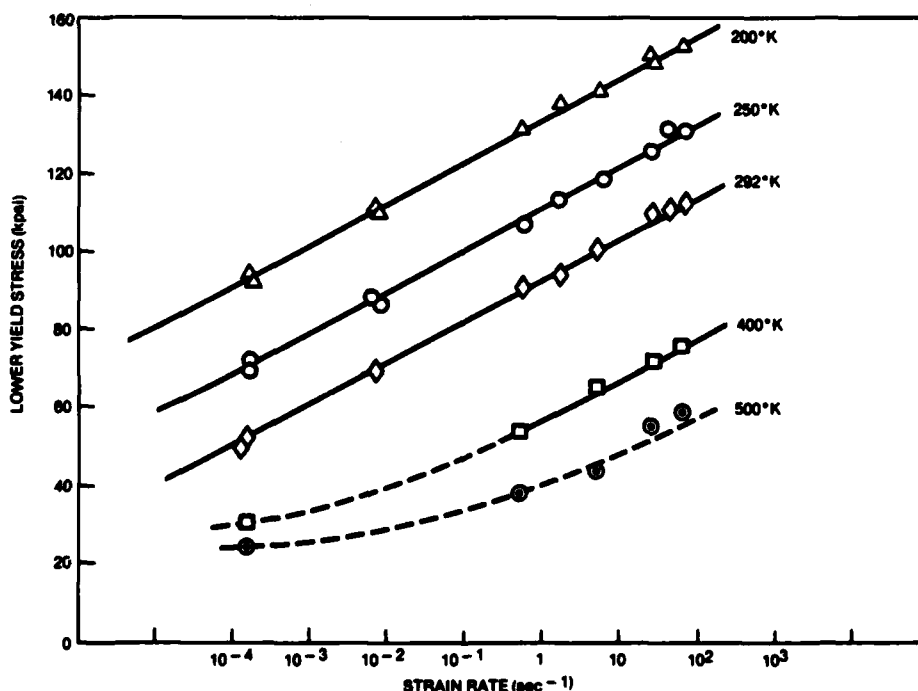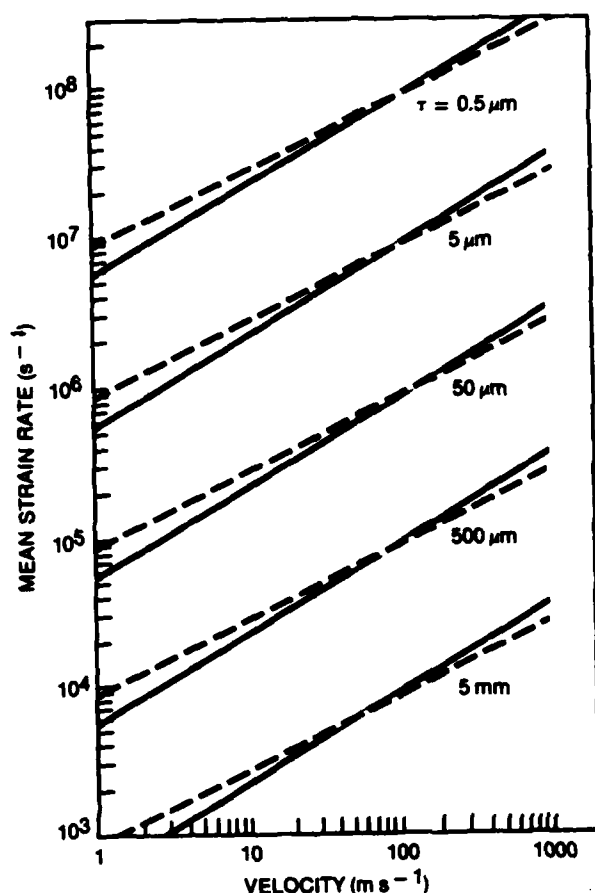n Figure 45B. The data shows that at 30-degree angle of incidence heat treatment condition does not affect the erosion rate, even though the erosion rate is significantly affected by angle of incidence. The angular dependence is surely associated with differing erosion mechanisms at the various impingement angles and the material response to these differing mechanisms.

Pure metals as well as the steel and aluminum alloys show the same type of behavior with respect to particle size and angle of incidence. The Fe-Cr alloys, however, have an erosion behavior that deviates slightly from that found for the 1095 steel alloy. Figure 38 shows the erosion rate of pure Fe and two Fe-Cr alloys, along with the Rb hardness. The figure shows that as the hardness of the the Fe-Cr alloys increase the erosion rate decreases. This is quite different than what was found for the 1095 steel shown in Figure 3. The erosion rate of the 1095 steel increased with increasing hardness, quite the opposite of the Fe-Cr alloy. Again, this is thought to be a consequence of the dynamic strain rate response. The Fe-Cr alloys are

Figure 45A.   Erosion Rate Versus Particle Size of 1095 Steel Heat Treated
to Three Different Conditions
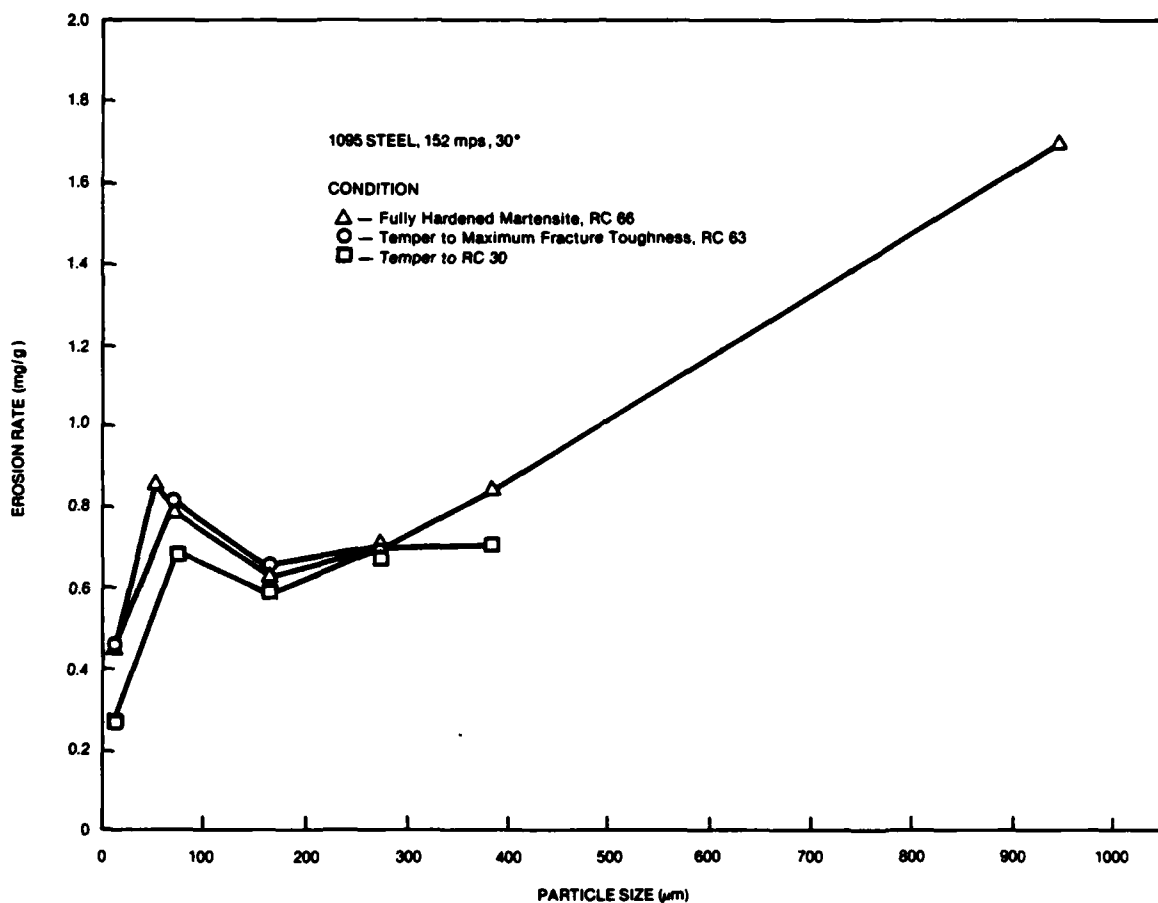
Figure 45B. Erosion Rate Versus Particle Size of 1095 Steel Heat Treated
to Three Different Conditions

single phase alloys which are solid solution hardened. Solid solution harden-
ing occurs by forcing different size solute atoms into the solvent lattice,
increasing the strain on the lattice. The hardening in this case increases
the lattice stiffness which improves erosion resistance. Similarily untemper-
ed martensite has a highly strained lattice, due to the carbon held in solu-
tion metastablely. However, the hard martensite has little available plas-
ticity. Therefore, during an impact, subsurface crack propagation is much
easier in martensite than in either Fe or the Fe-Cr alloys, which the results
presented indicate to be a major part of the material removal mechanism in
hardened steel. The two materials have quite different erosion mechanisms and
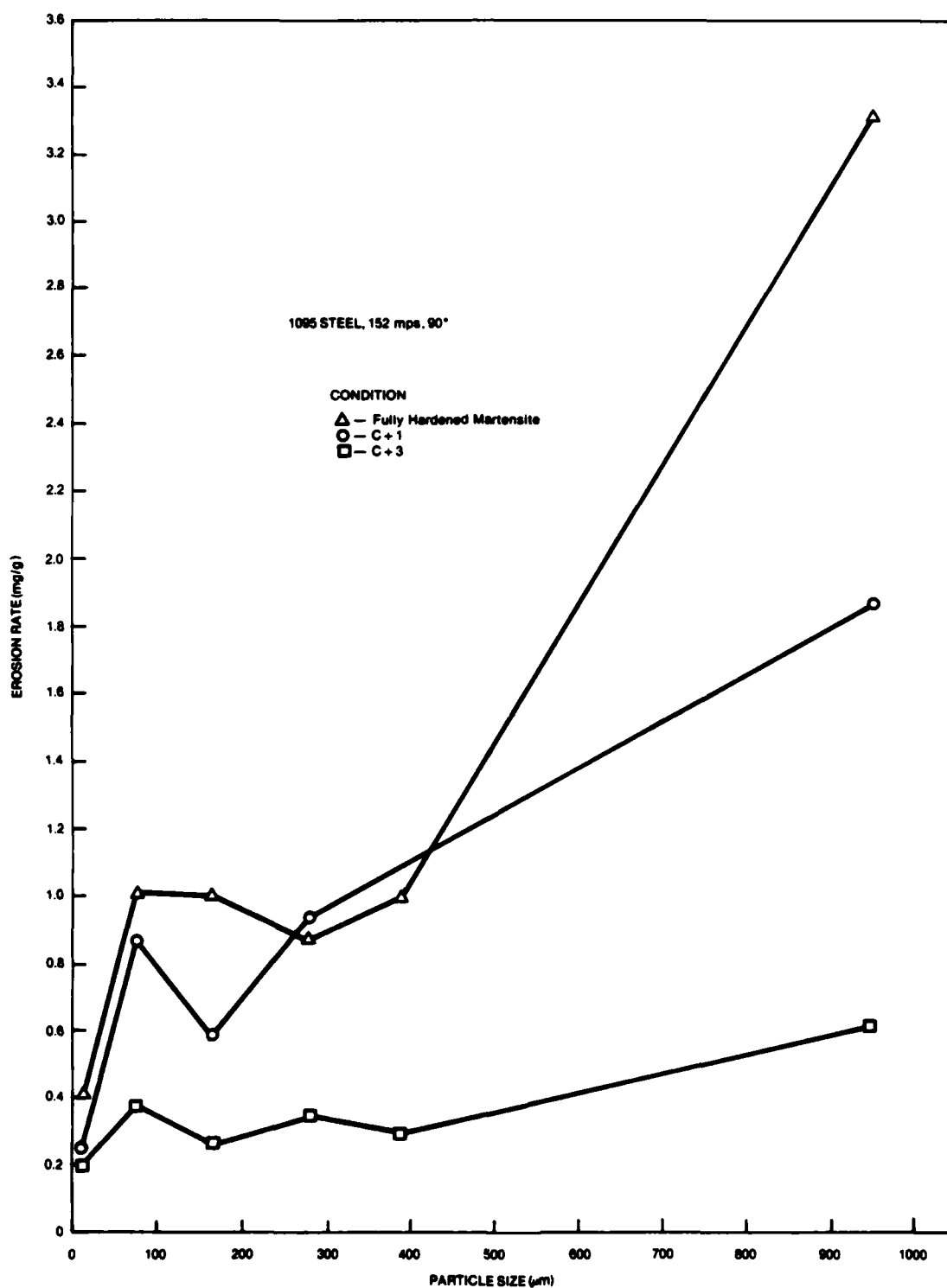must be considered separately.
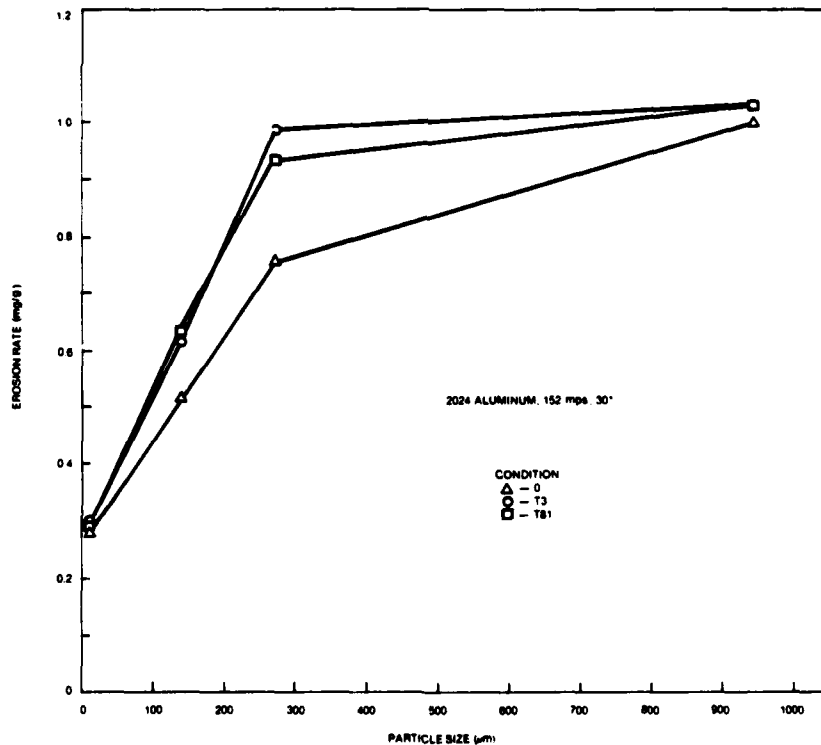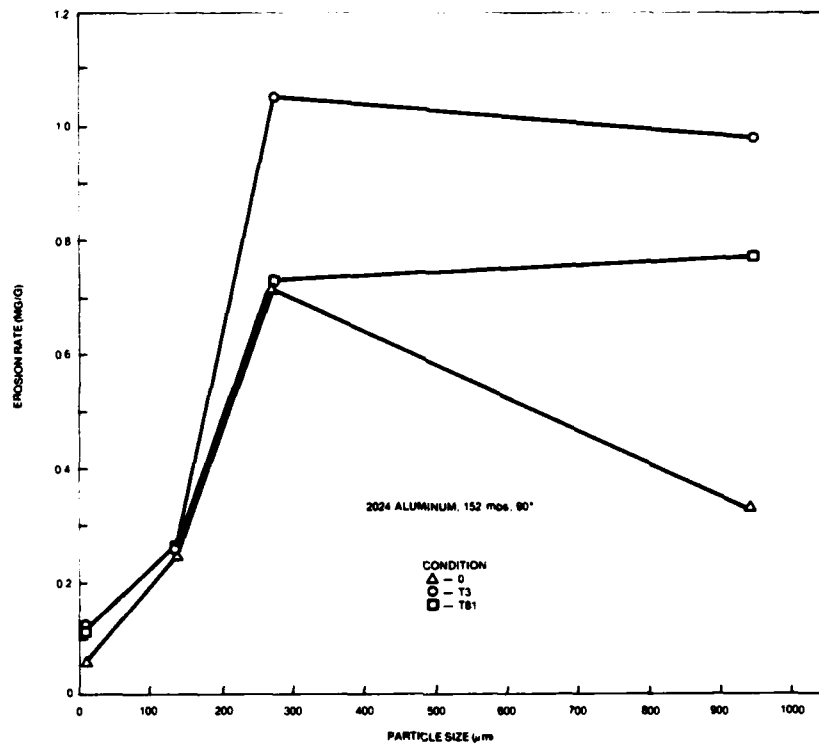
Figure 46. Erosion Rate Versus Particle Size of 2024 Aluminum Heat Treated to Three Different Conditions
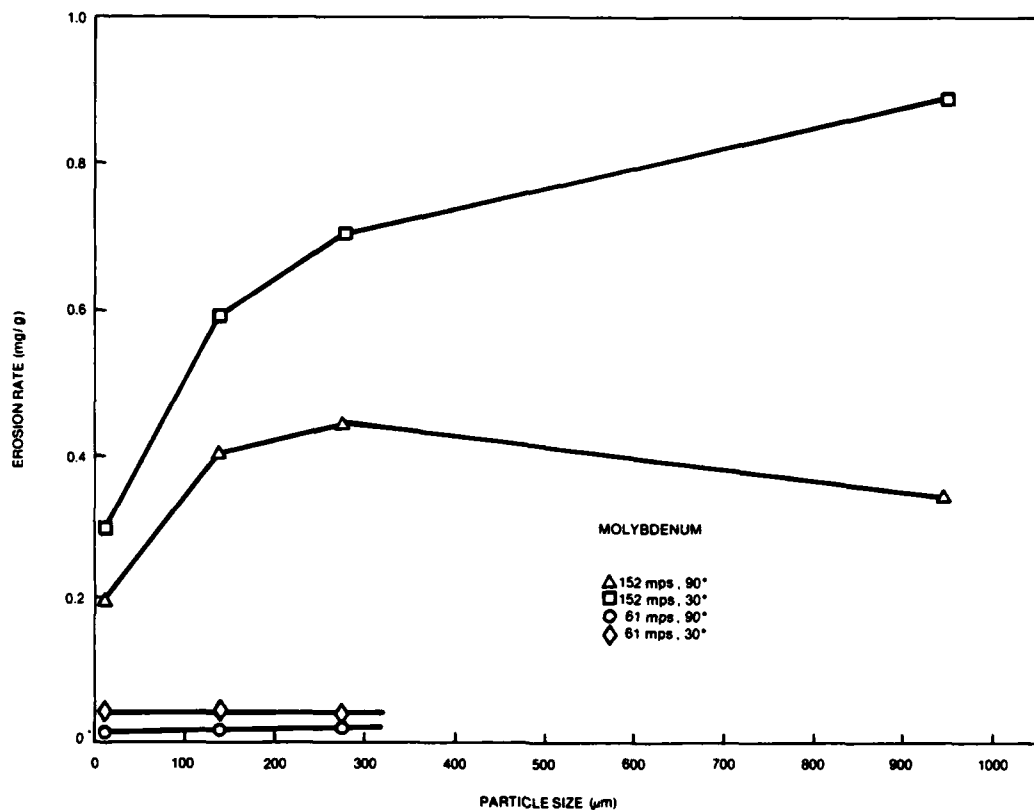
Figure 47. Erosion Rate Versus Particle Size of Pure Molybdenum

2.2 PHASE II - DYNAMIC HARDNESS

2.2.1 Introduction

The results of the Phase I effort showed that the material's microstructure could control the type of erosion response, whether it be ductile or brittle (as indicated by the angle of maximum weight loss). However, it was also shown that this occurrence of transition from brittle to ductile erosion type is also a function of particle size or strain rate; since, the strain rate during the impact event varies inversely with particle size. For eroding particles below 50 microns in diameter, all materials tested, for all micro-structural conditions, exhibited ductile-type erosion. This strain rate dependence of the erosion characteristics is not well understood. A major difficulty hindering the understanding of erosion is the high strain rate and short duration of an erosion impact event. Conventional mechanical properties are measured at strain rates many orders of magnitude lower than that which occurs during an erosion impact. Since it is well known that mechanical properties are influenced by strain rate (Ref. 23), it would appear reasonable

57
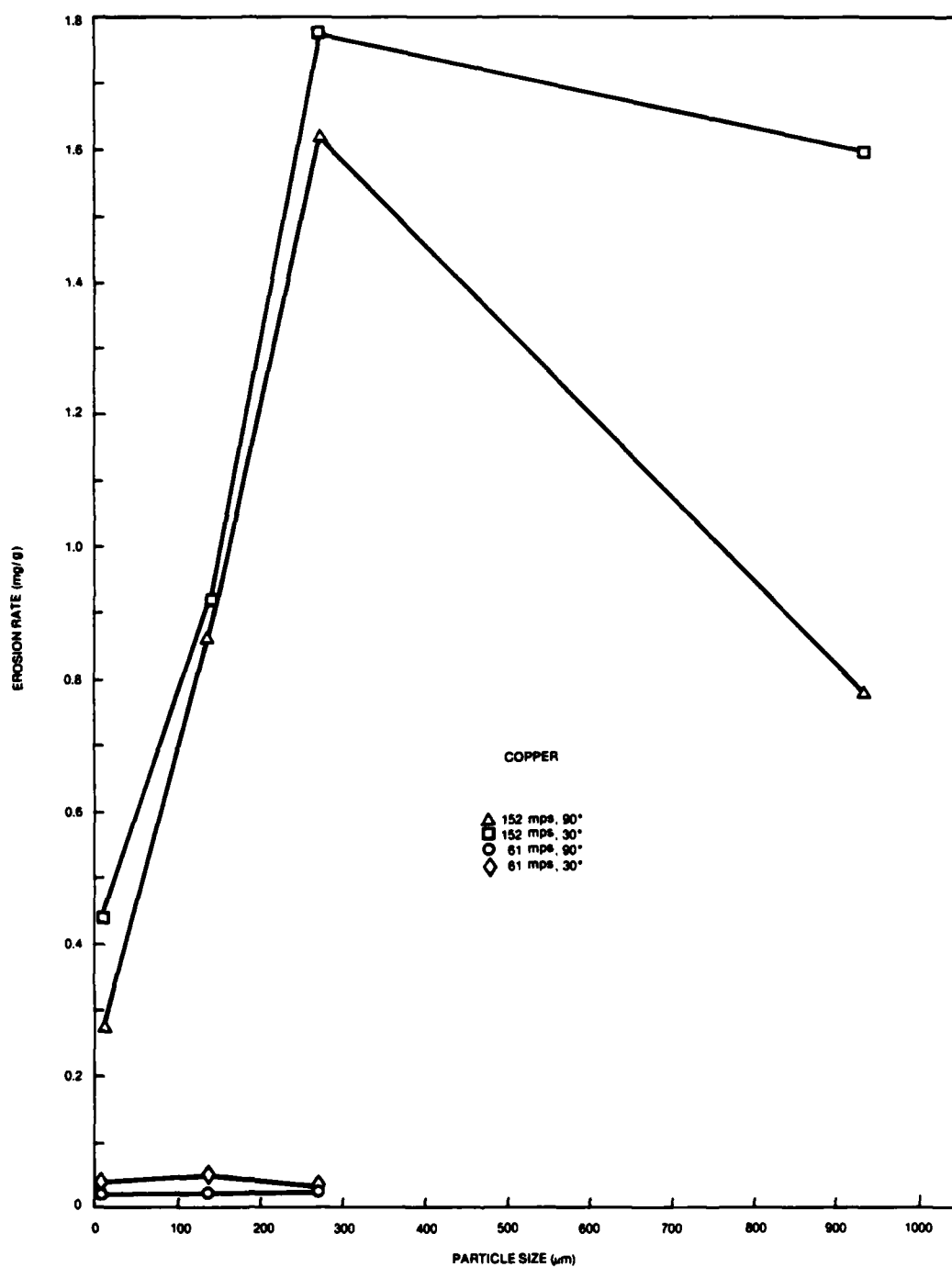
Figure 48.   Erosion Rate Versus Particle Size of Pure Copper
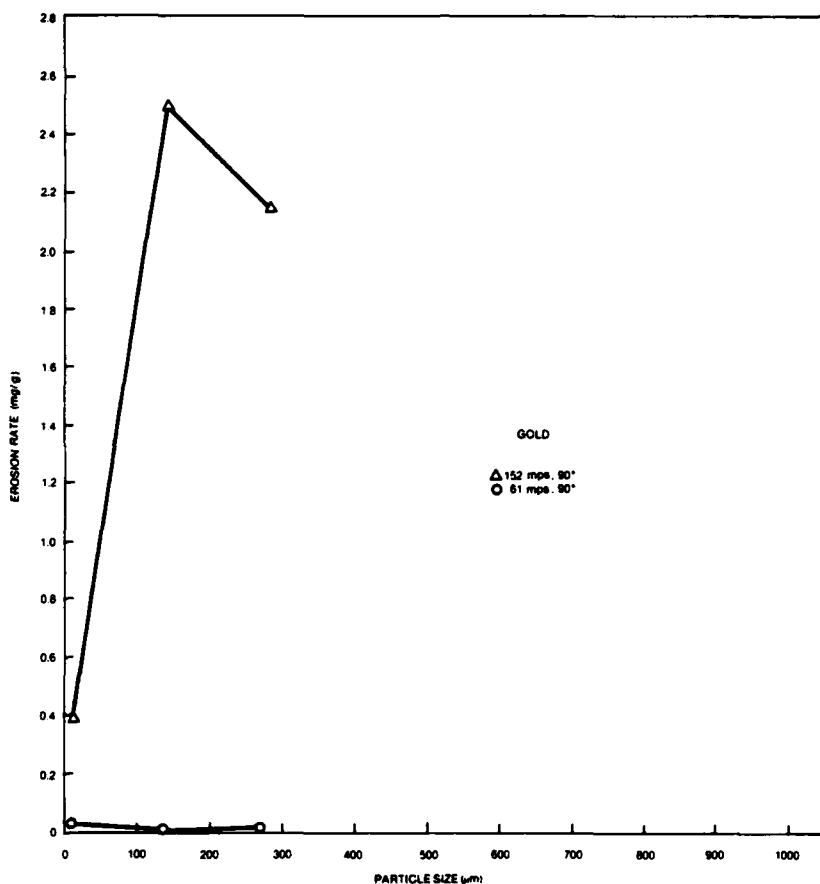
Figure 49. Erosion Rate Versus Particle Size of Pure Gold

that conventional mechanical properties would not correlate well with a materials erosion response.

It is believed that the evaluation of a material property under dynamic conditions similar to those experienced during an erosion impact event would provide valuable insight into the fundamental aspects of erosion and aid in the understanding of the material loss mechanisms. Dynamic hardness testing can be performed under conditions very similar to those of actual erosion testing. Strain rates in the 10^5 to 10^6/sec are readily obtainable with the facilities available for erosion testing.

The objective of this phase of the program was to measure the dynamic hardness of several materials under several dynamic conditions and to correlate these results with the results of erosion testing under similar dynamic conditions.

2.2.2 Dynamic Hardness Testing

The dynamic hardness of various target materials was determined as a function of both particle size and velocity. The dynamic hardness is defined as the pressure over the area of contact, which is assumed to be constant throughout the entire impact, and can be calculated from

$$p = \frac{MV_o^2}{2\pi l^2 (r - l/3)}$$

where V_o is the initial impact velocity, M is the mass of the impacting particle, l is the crater depth and r is the radius of the impacting particle (Ref. 24, 25). The crater diameter d is related to the crater depth l by

$$d = 2(2rl - l^2)^{1/2}$$

An order of magnitude estimate of the plastic strain rate $\dot{\varepsilon}$ during the impact can be determined from

$$\dot{\varepsilon} = 0.064(dV_o/l) \quad \text{(Ref. 24)}$$

The dynamic strain rates of the current work were estimated to be in the range of $10^5 - 10^6$/sec.

Dynamic hardness testing was performed using spherical glass bead indenters of three sizes, 23 microns, 69 microns, and 158 microns. The 23 microns size turned out to be too small to produce craters defined well enough to be of practical use. Table 6 shows the test conditions used for the dynamic testing.

The glass spheres used as indenters, were not of a unique size but a range of sizes with the average being that stated. Table 7 gives the size ranges of the three types of spheres used. The average size of the glass spheres was determined by measuring the diameter of forty spheres under magnification.

Specimens for dynamic hardness measurements were polished to produce a smooth surface to aid in making indention measurements. Approximately 0.007 gm of glass spheres were used for each dynamic hardness measurement. This resulted in well spaced craters that could readily be measured with the use of a metallograph. For each dynamic hardness measurement, the diameter of forty craters were measured. From the average crater diameter the average crater depth was calculated. The dynamic hardness was calculated from the average crater diameter, average particle size and the velocity of the averaged size particle.

A very wide variety of materials were tested. The substrates selected include pure metals with FCC, BCC and HCP crystal structures, simple binary alloys, and commercial alloys. The materials tested along with their Knoop hardness are given in Table 8. The pure metals were tested in the annealed condition

Table 6

Dynamic Hardness Test Conditions

Particle Diameter (microns)	Impact Velocity (mps)
23	240 209 123
69	207 181 112
158	182 159 98

Table 7

Glass Spheres Size Parameters

Average Diameter (Microns)	Screen Size (Mesh Size)	Size Range (Microns)
23	-400	<37
69	-150 + 200	<98
158	-50 + 100	<297

whereas the intermetallic compounds were aged to produce an ordered structure. The modified Fe_3Al was alloyed with 3.32% Mo to both aid in processing and improve the mechanical properties. Specimens were tested in the 100% and 50% ordered conditions. The Ti-6Al-4V was solution heat treated at 950°C for 1/2 hour followed by an ice water quench. Some of the specimens were then tempered at 530°C for four hours followed by air cooling. The 1095 steel specimens were normalized at 885°C for two hours followed by air cooling, austenitized at 800°C for two hours, quenched in ice brine and tempered for two hours at 370°C to produce a hardness of Rc 50.

61

Table 8

Substrate Materials Used For Dynamic Hardness Measurements

Material	Knoop Hardness
Mg	<60
Al	69
Cr	621
Fe	104
Ni	278
Cu	107
Zn	<69
Mo	241
Fe_3Al	304
FeAl	542
Ni_3Al	318
NiAl	241
90Fe-10Cr	192
70Fe-30Cr	391
Al, 2024-T6	122
Ti-6Al-4V (as-quenched)	466
Ti-6Al-4V (tempered)	438
SAE 1095 (as-quenched)	846
SAE 1095 (tempered)	547
Modified Fe_3Al (50% ordered)	318
Modified Fe_3Al (100% ordered)	351

Erosion testing was performed under conditions similar to those used for dynamic hardness testing. Quartz sand 68 microns average particle size were accelerated to 180 mps. The target material was impacted with 50 gm of sand at a 30° angle of incidence. Erosion weight loss was determined and converted to volume loss, giving a more representative comparison of erosion rates between different materials. The untempered 1095 steel was too hard for the glass spheres to make clear indentions; therefore, it was not possible to obtain dynamic hardness measurements of the untempered 1095 steel.

2.2.3 Results of Dynamic Hardness Testing

The results of the dynamic hardness testing are given in tabulated form in Appendix 1 and shown graphically in Figures 50-66. Both the crater depth vs. particle velocity and the dynamic hardness vs. particle velocity for constant indenter size, are shown. Generally, there is a monotonic increase in the crater depth with particle velocity as well as an increased crater depth with increased particle size. The particle size influenced the dynamic hardness more significantly than the particle velocity. It is apparent from the data that the error in the dynamic hardness measurements is larger than the variation due to particle velocity resulting in no clear relationship developed between particle velocity, and dynamic hardness. Figures 67 and 68 clearly show the strong influence of particle size on both the crater depth and dynamic hardness. As the particle size increases the crater depth increases; whereas the dynamic hardness decreases with increasing particle size at constant particle velocity.

The dynamic strain rates, shown in Appendix 1 are 2-4 x 10^6/sec and 4-8 x 10^5/sec for the 68 and 158 micron particle sizes respectively; however, the variation in dynamic strain rate with particle velocity is quite small. This accounts for the large difference in dynamic hardness between particle sizes with little difference due to velocity. The measurements agree in principle with those expected from previous measurements at high strain rates (Ref. 23). Clearly, increasing the dynamic strain rate increases the dynamic hardness.

The results of the erosion testing are shown in Table 9. The measured weight loss (and volume loss) decreases with particle velocity. Again, it is shown that heat treatment has only a minor affect on erosion resistance. Both the as-quenched and tempered Ti-6Al-4V and 1095 steel show only a small difference in erosion rates. Yet, there is a significant difference between the FeAl and Fe_3Al, NiAl and Ni_3Al and most notably, the 50% ordered and 100% ordered modified Fe_3Al. This gives further evidence that "lattice" type changes are more effective in influencing the erosion characteristics than microstructural changes.

Due to the uncertainty of the dynamic hardness measurements, it is not possible to make a direct correlation between the dynamic hardness with the measured erosion rates, however, Table 10 shows a general ranking of both erosion resistance and dynamic hardness. The general trend is that the materials with the higher dynamic hardness have the higher erosion resistance.
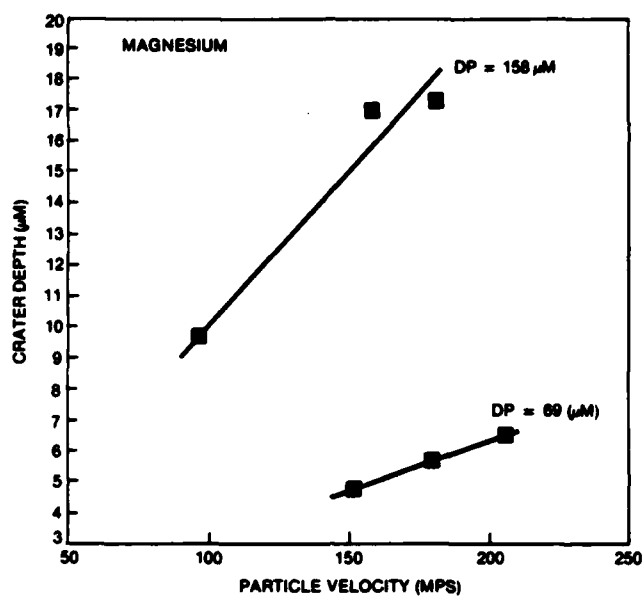
Figure 50a. Variation in Crater Depth Versus Particle
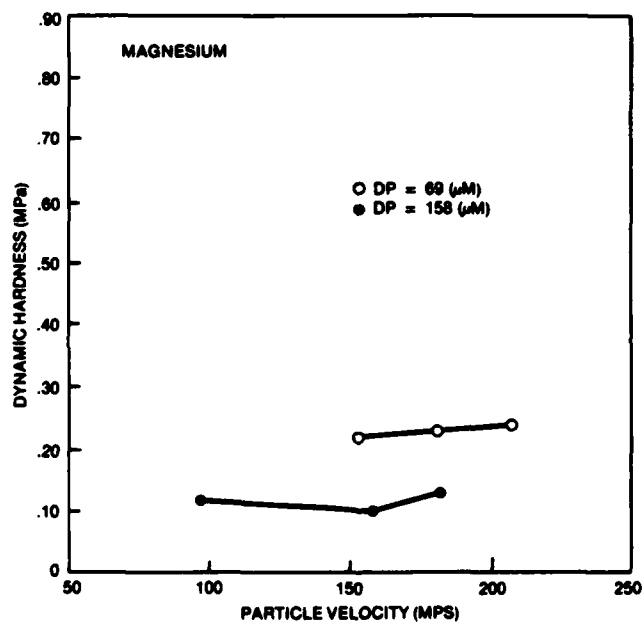Velocity for Magnesium

Figure 50b. Dynamic Hardness Versus Particle Velocity

64

Figure 51a.   Variation in Crater Depth Versus Particle
Velocity for Aluminum

Figure 51b.   Dynamic Hardness Versus Particle Velocity

65

Figure 52a. Variation in Crater Depth Versus Particle
Velocity for Chromium

Figure 52b. Dynamic Hardness Versus Particle Velocity

66

Figure 53a. Variation in Crater Depth Versus Particle
Velocity in Iron

Figure 53b. Dynamic Hardness Versus Particle Velocity

67

Figure 54a. Variation in Crater Depth Versus Particle Velocity in Nickel
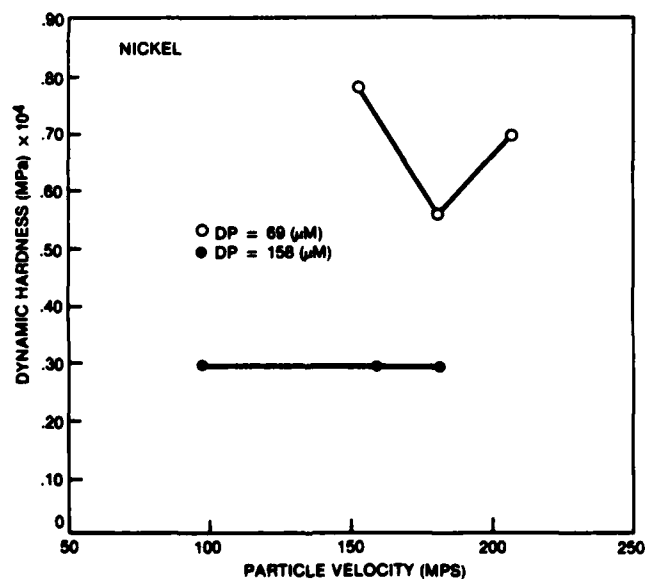
Figure 54b. Dynamic Hardness Versus Particle Velocity

68
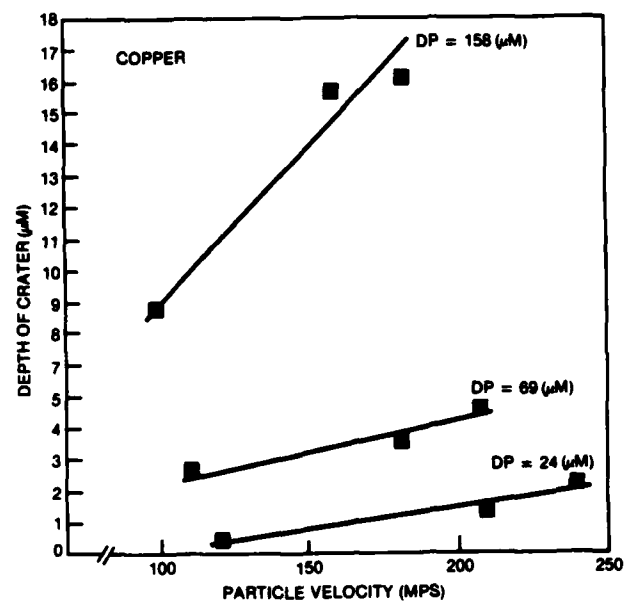
Figure 55a. Variation in Crater Depth Versus Particle
Velocity for Copper
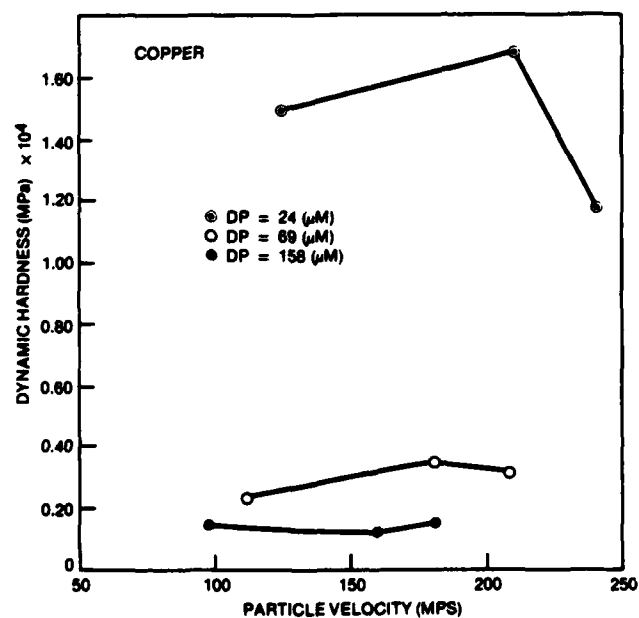
Figure 55b. Variation in Dynamic Hardness Versus Particle
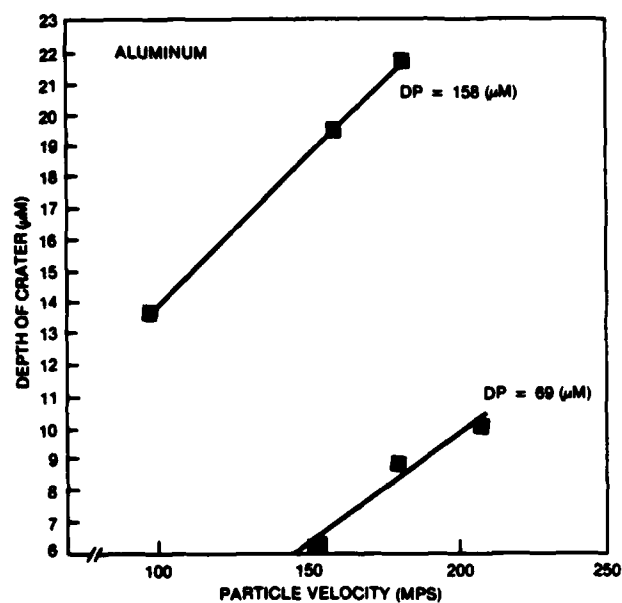Velocity

69
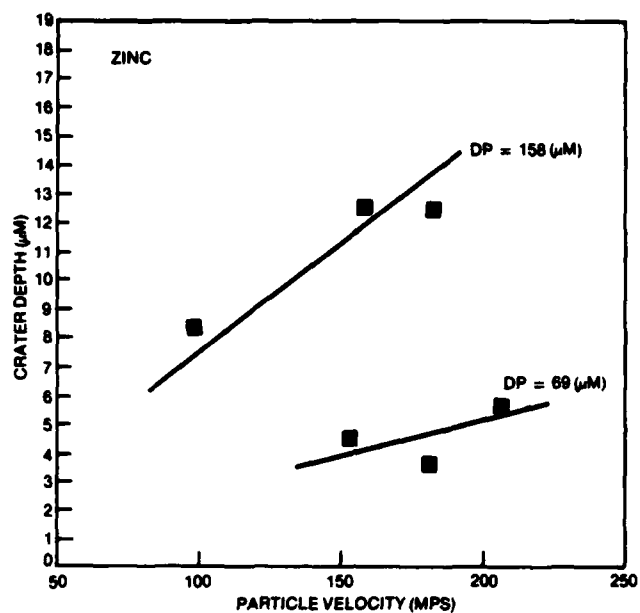
Figure 56a.   Variation in Crater Depth Versus Particle
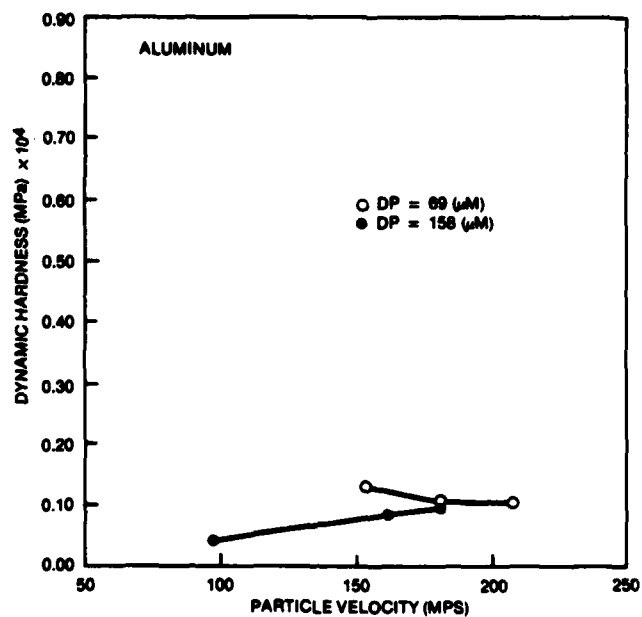   Velocity for Zinc
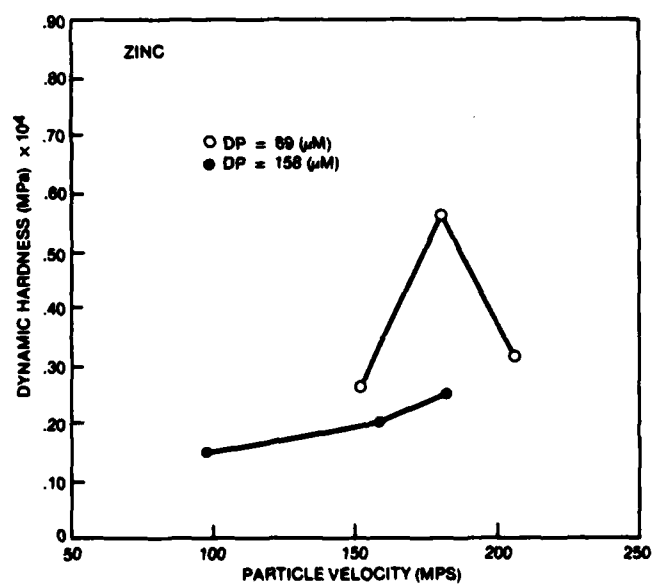
Figure 56b.   Dynamic Hardness Versus Particle Velocity
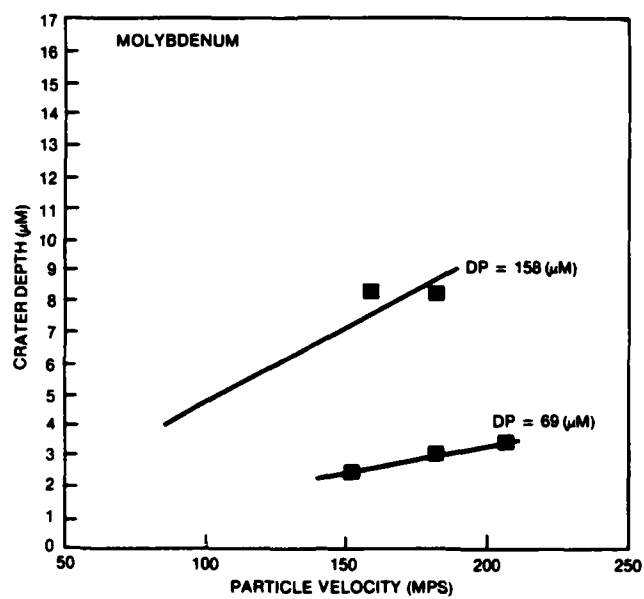
Figure 57a. Variation in Crater Depth Versus Particle
Velocity for Molybdenum
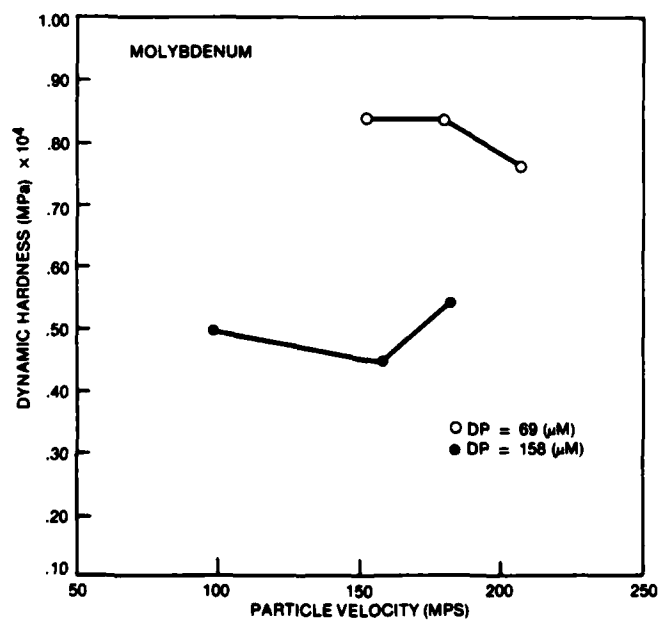
Figure 57b. Dynamic Hardness Versus Particle Velocity

71
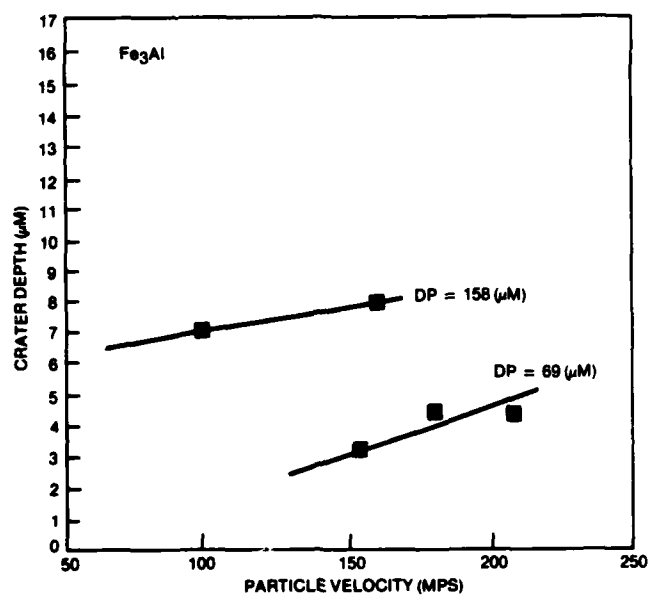
Figure 58a. Variation in Crater Depth Versus Particle
Velocity for Fe₃Al
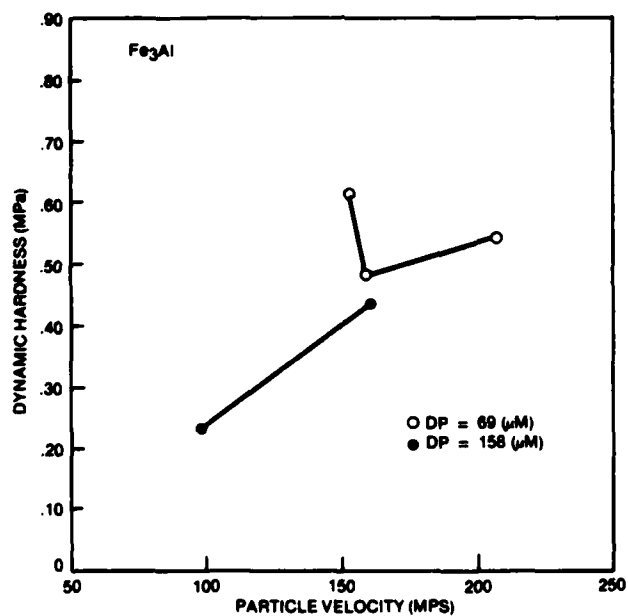
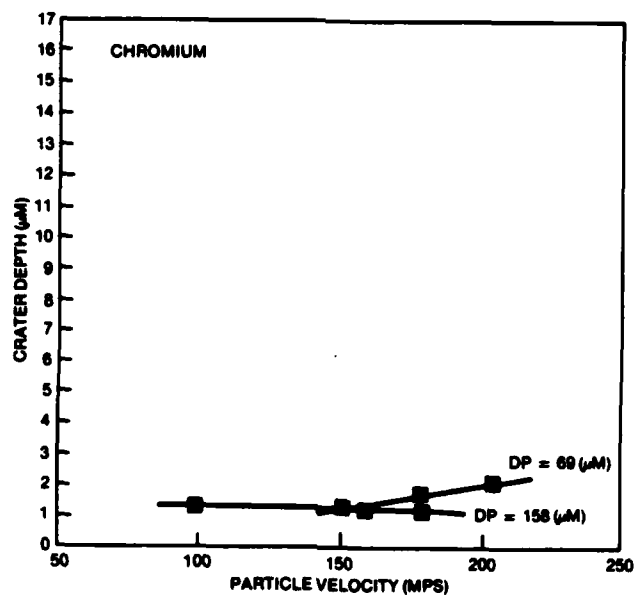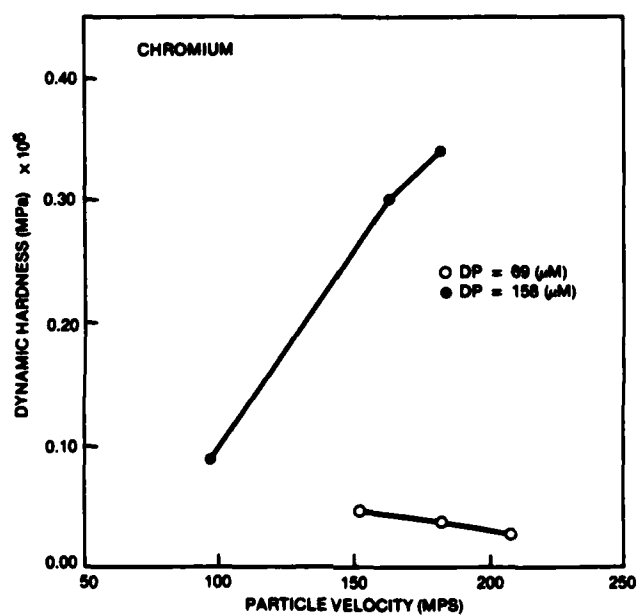Figure 58b. Dynamic Hardness Versus Particle Velocity

72
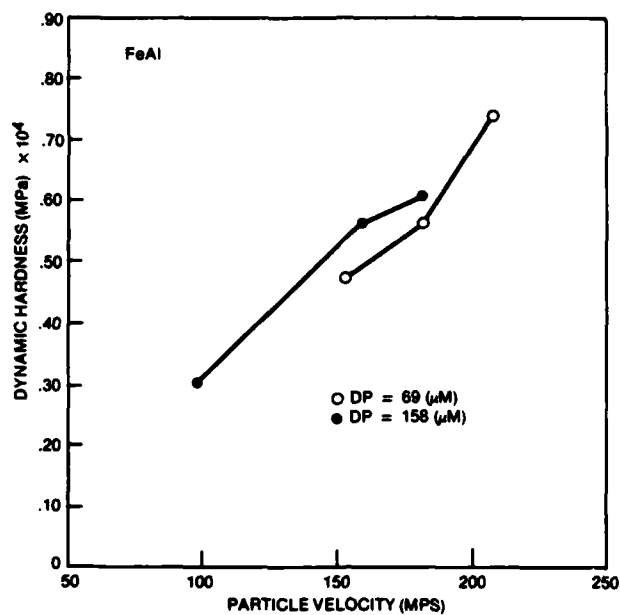
Figure 59a. Variation in Crater Depth Versus Particle
Velocity in FeAl
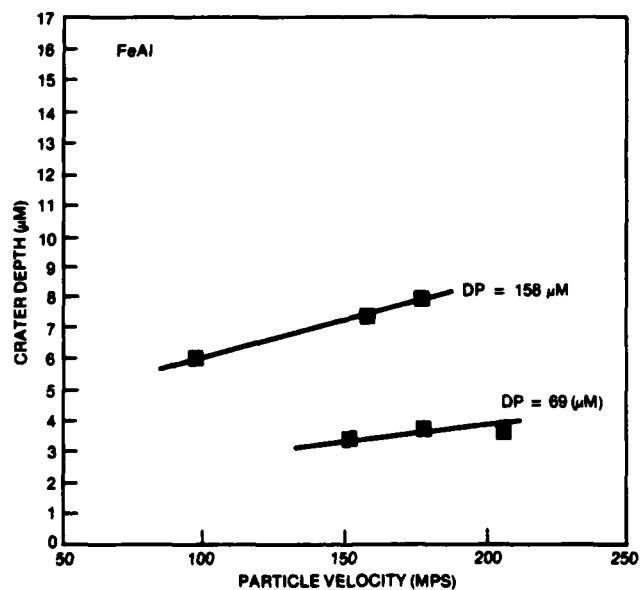
Figure 59b. Dynamic Hardness Versus Particle Velocity

73
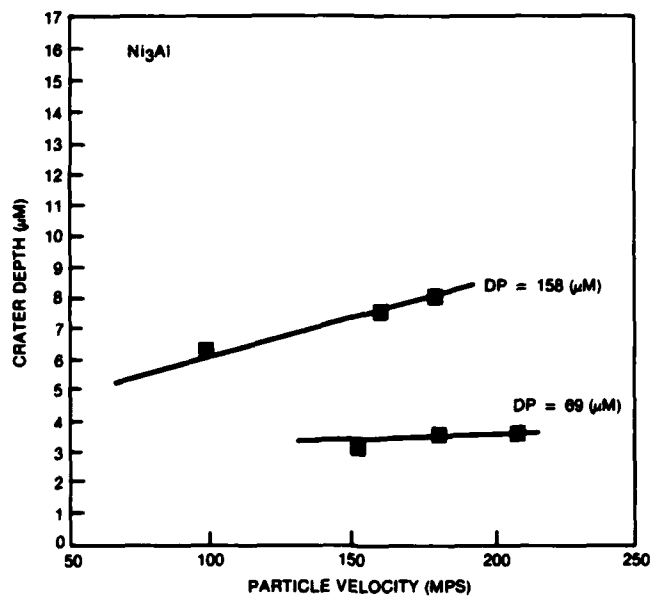
Figure 60a. Variation in Crater Depth Versus Particle
Velocity in Ni₃Al
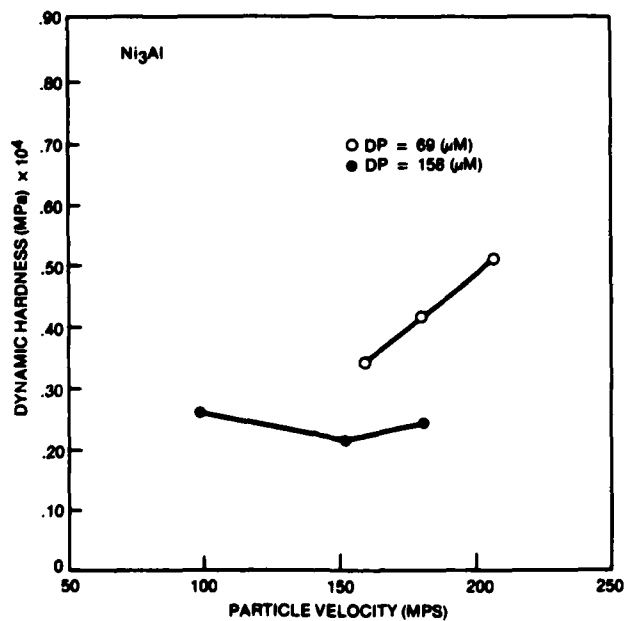
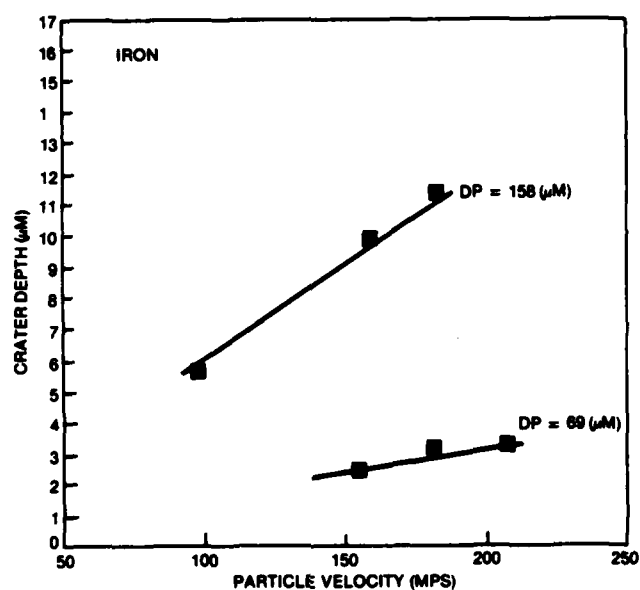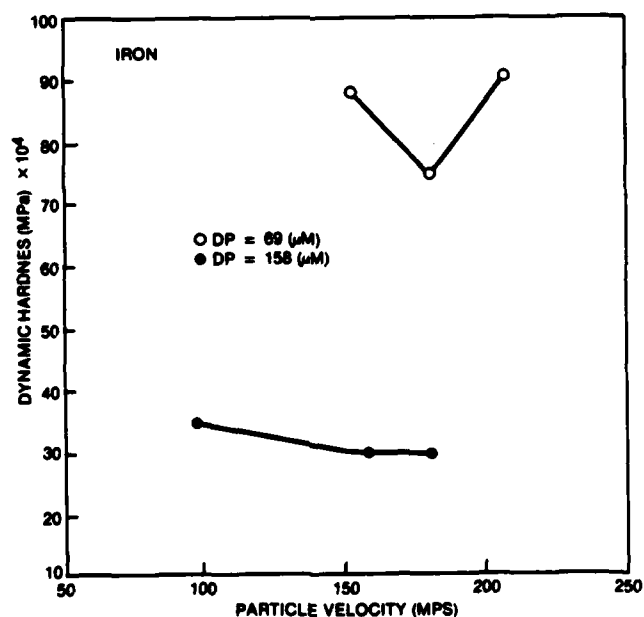Figure 60b. Dynamic Hardness Versus Particle Velocity
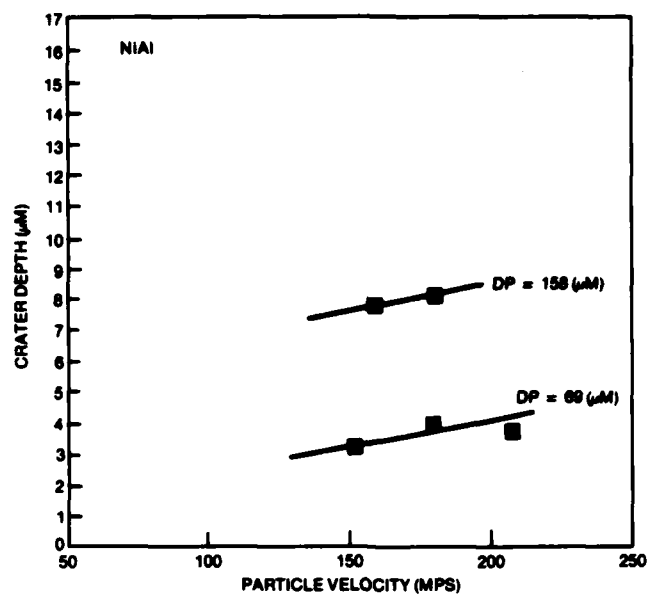
Figure 61a. Variation in Crater Depth Versus Particle
Velocity in NiAl
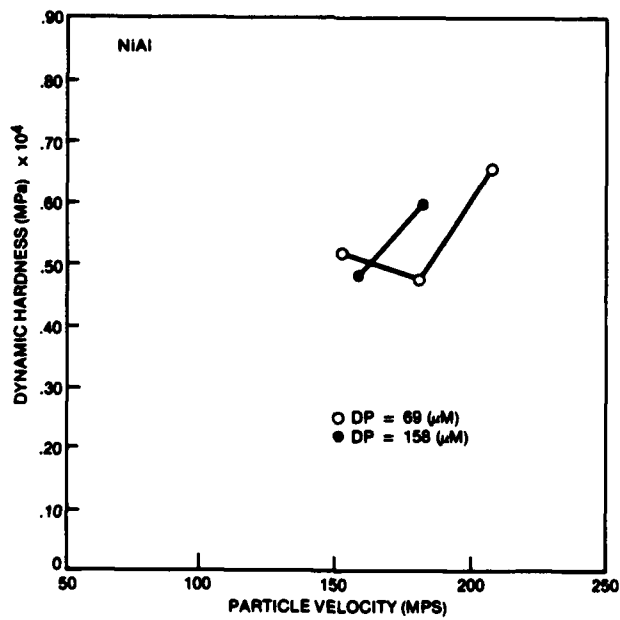
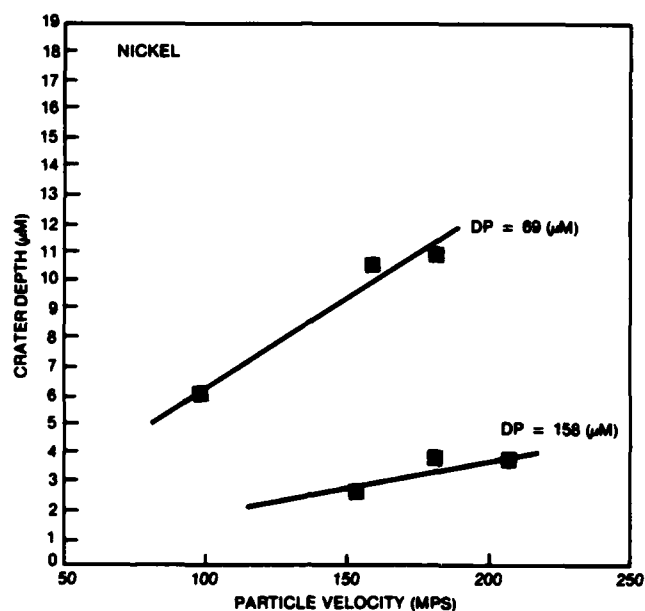Figure 61b. Dynamic Hardness Versus Particle Velocity
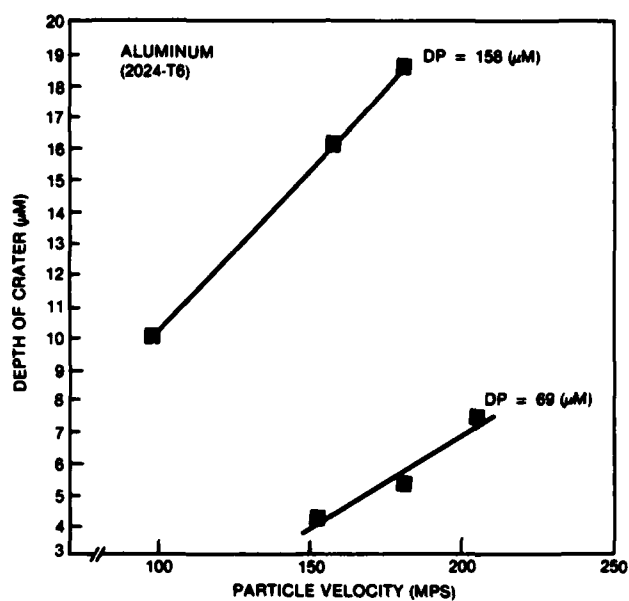
Figure 62a.   Variation in Crater Depth Versus Particle Velocity for the
Commercial Aluminum Alloy 2024 Heat Treated to the T6
Condition
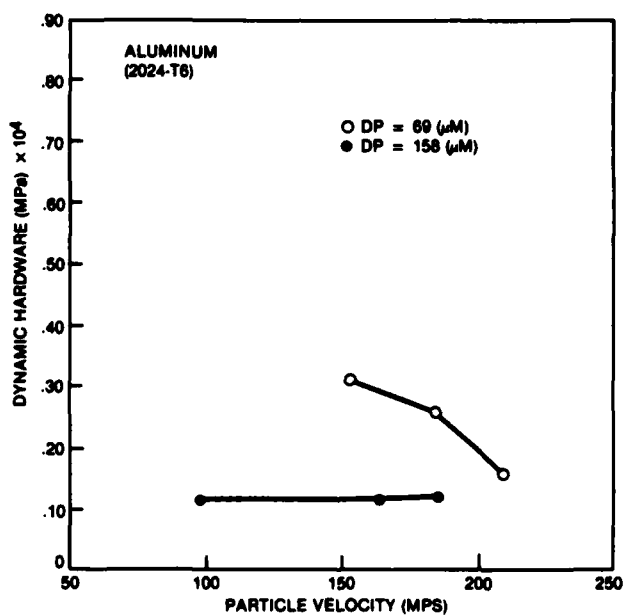
Figure 62b.   Dynamic Hardness Versus Particle Velocity

76
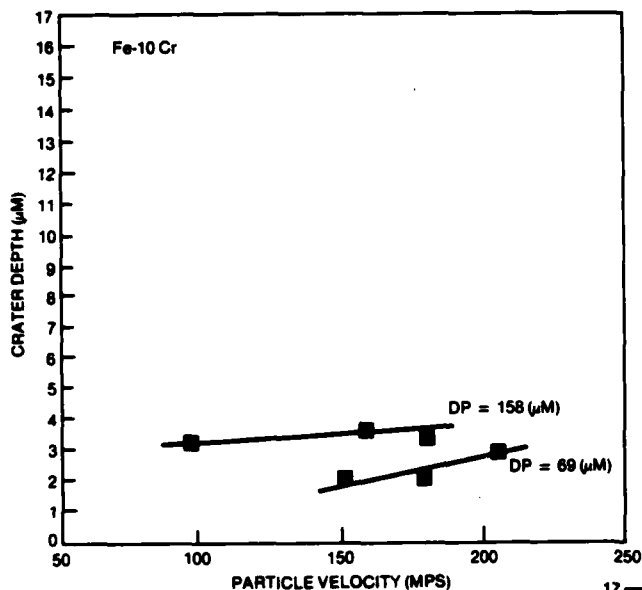
Figure 63a.

Variation in Crater Depth
Versus Particle Velocity
for Fe-10Cr

Figure 63b.

Crater Depth Versus Particle
Velocity for Fe-30Cr
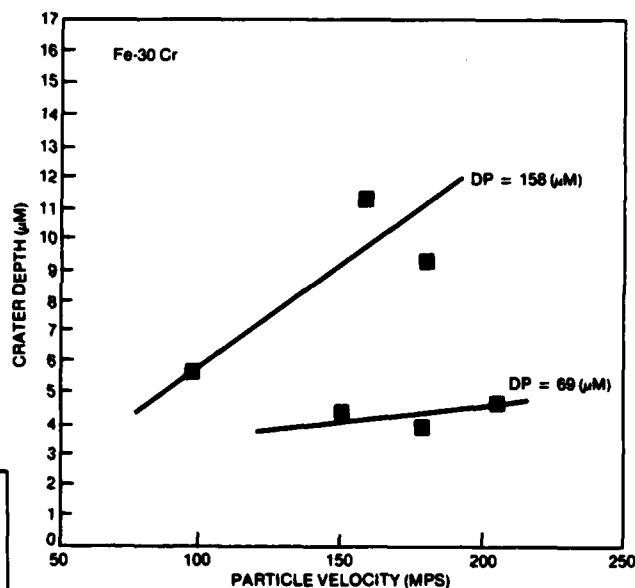
Figure 63c.

Dynamic Hardness Versus Parti-
cle Velocity for Fe, Fe-10Cr
and Fe-30Cr

77
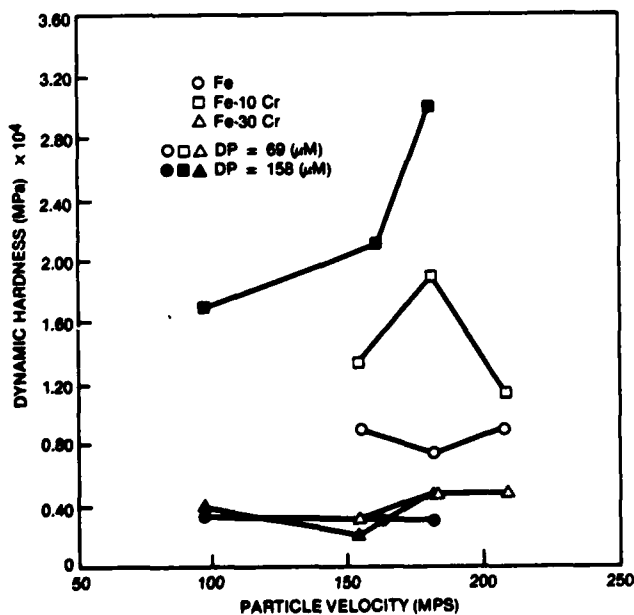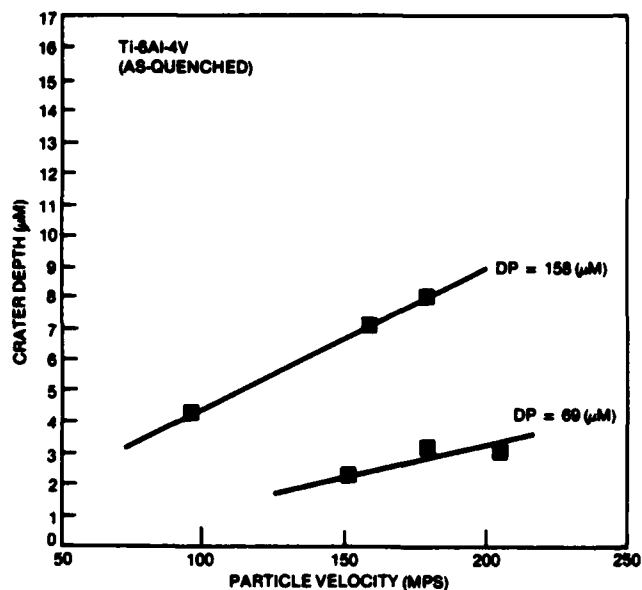
Figure 64a.

Variation in Crater Depth Versus Particle Velocity for Ti-6V-4Al in the As-Quenched Condition

Figure 64b.

Crack Depth Versus Particle Velocity for Ti-6V-4Al in the Quenched and Tempered Condition
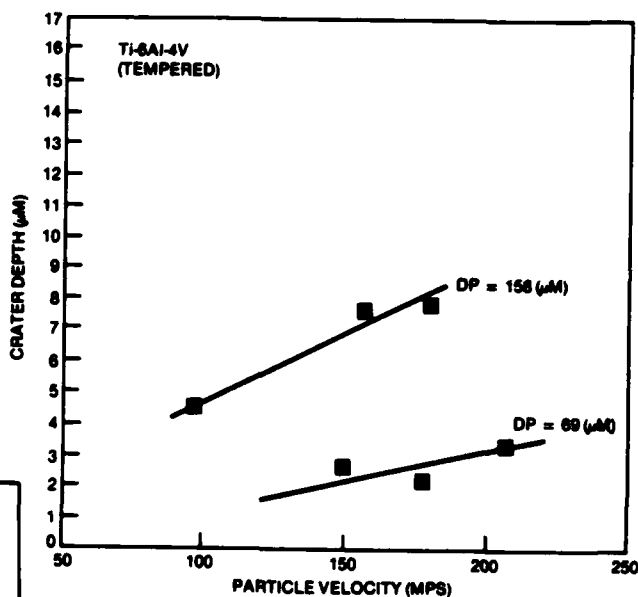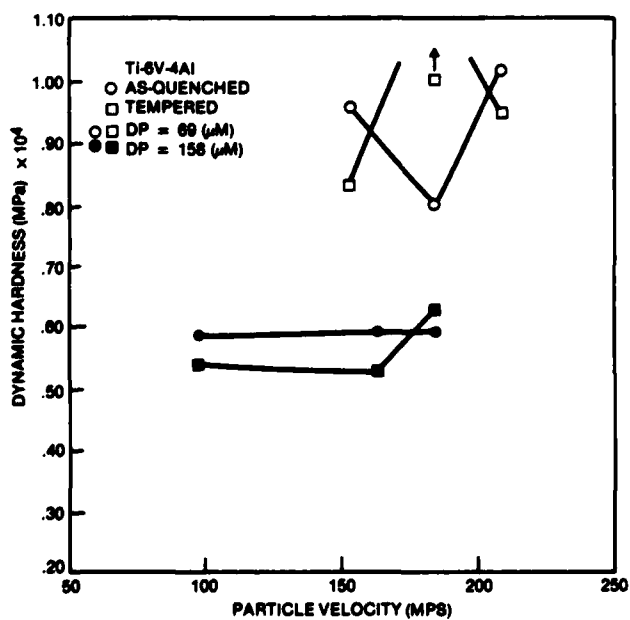
Figure 64c.

Dynamic Hardness Versus Particle Velocity for Ti-6V-4Al in Both the Unquenched and Tempered Condition
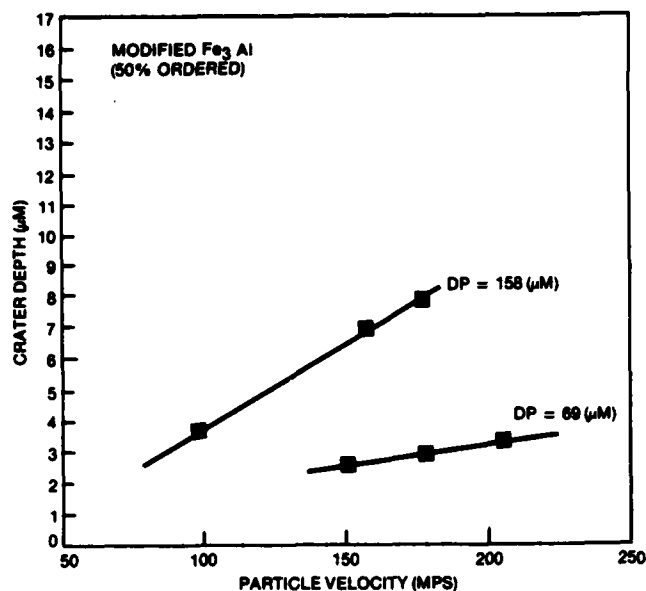
Figure 65a.

Variation in Crater Depth Versus Particle Velocity for a Modified Fe₃Al Alloy Heat Treated to Produce a 50% Ordered Structure

Figure 65b.

Crater Depth Versus Particle Velocity for the Modified Fe₃Al Alloy 100% Ordered
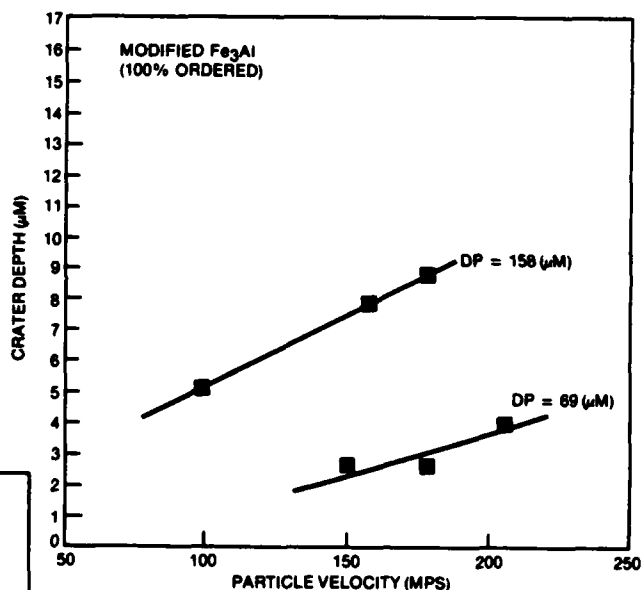
Figure 65c.

Dynamic Hardness Versus Particle Velocity for the Modified Fe₃Al Alloy in Both Heat Treat Conditions
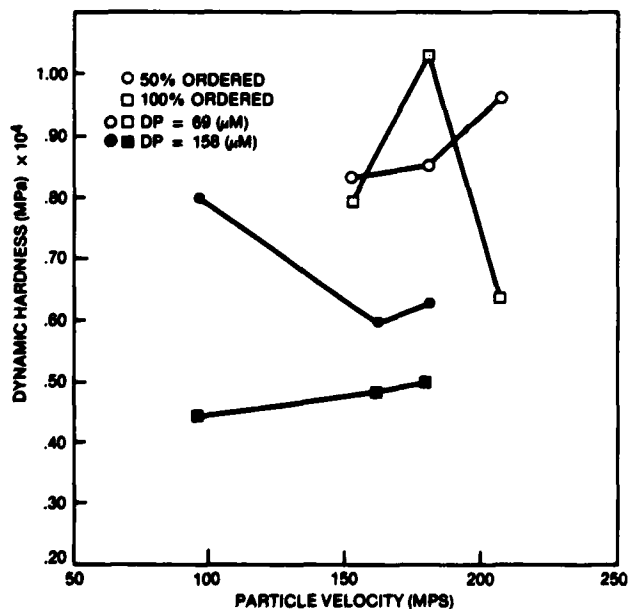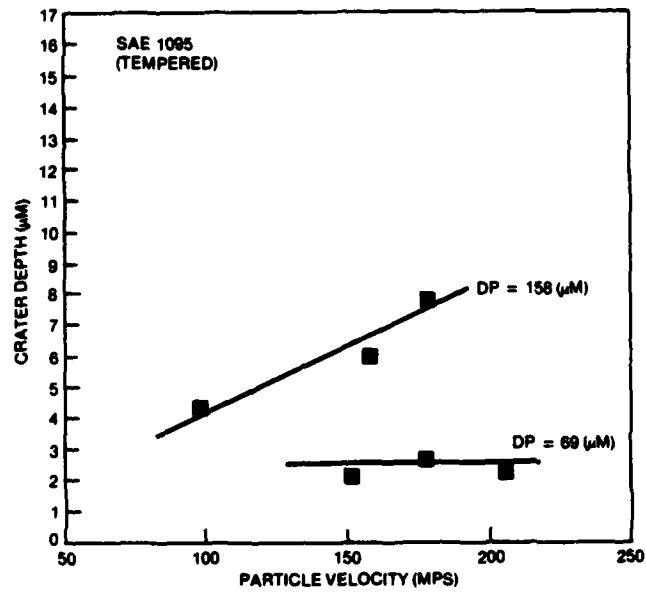
Figure 66a. Variation in Crater Depth Versus Particle Velocity for
SAE 1095 Steel in the Condition Tempered to Produce
Rc 50 Hardness
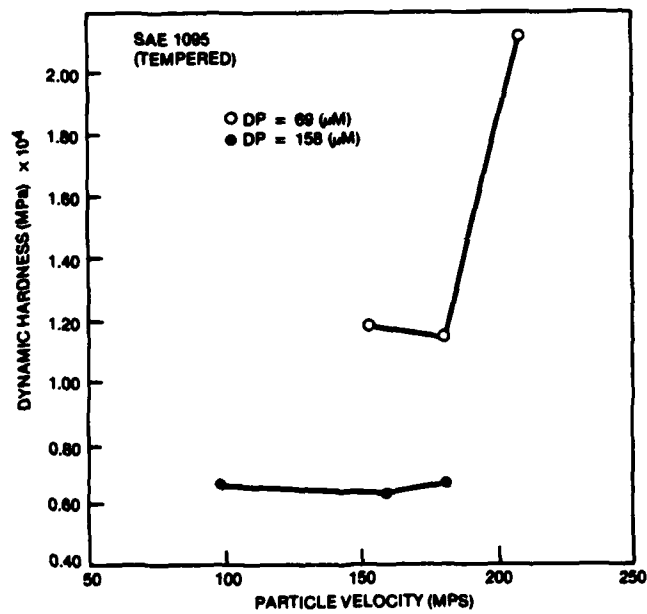
Figure 66b. Dynamic Hardness Versus Particle Velocity
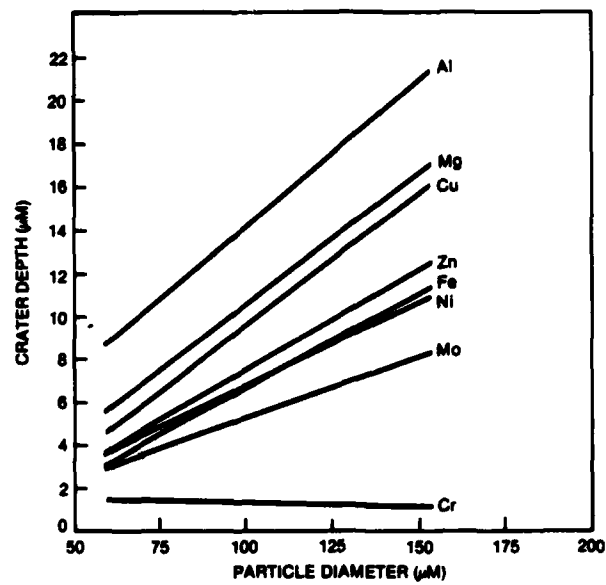
Figure 67a. Variation in Crater Depth for Two Particle Sizes of Constant Velocity for Several Pure Metals
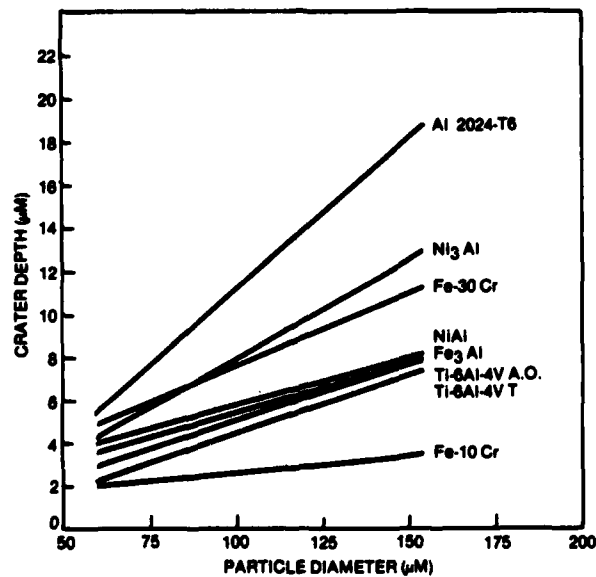
Figure 67b. For Several Alloys

81
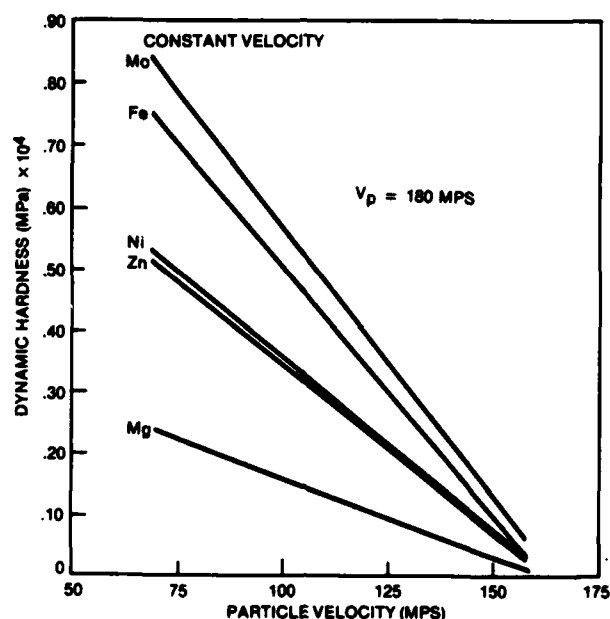
Figure 68. Variation in Dynamic Hardness for Two Particle Sizes at Constant Velocity of Several Pure Metals

This is particularly evident when like materials are compared. For example FeAl is above Fe_3Al in both columns as well as the 100% ordered Modified Fe_3Al over the 50% ordered Modified Fe_3Al.

2.2.4 Discussion

The results clearly indicate that there is an interrelationship between erosion resistance and dynamic hardness. Dynamic hardness measurements provide a means of determining a material property under dynamic conditions at very high strain rates. Great care, however, must be taken if accurate reliable data is to be obtained. A major problem with the current work is that the range of particle sizes is too large, resulting in a significant uncertainty in the particle size. This uncertainty in particle size in turn leads to a significant uncertainty in the particle velocity, both important parameters in the dynamic hardness calculations. The method has been shown affective for rather small sized indenters, achieving very high strain rates (i.e. $>10^6$/sec.). Further development of the experimental technique could lead to sigfnificant advancements in the understanding of deformation at high strain rates and the mechanisms of material removal by erosion.

Table 9

Results of Erosion Testing

Test Conditions:	Erosion 30°, 68 microns Weight Loss gm/50 gm $(cm^3/50$ gm$)$		Quartz
Material	207 mps	181 mps	153 mps
Cr	.1224 (0.0170)	.0930 (0.0129)	0.0632 (0.0088)
90Fe-10Cr	.1772 (0.0227)	.1268 (0.0163)	.0801 (0.0103)
70Fe-30Cr	.1488 (0.0193)	.1113 (0.0143)	.0716 (0.0093)
Fe_3Al	0.1203 (0.0212)	0.0934 (0.0165)	0.0677 (0.0119)
FeAl	0.1070 (0.0184)	0.0857 (0.0147)	0.0569 (0.0098)
Ni_3Al	0.1620 (0.0217	0.1258 (0.0168)	0.0767 (0.0103)
NiAl	0.0643 (0.0108)	0.0531 (0.0090)	0.0352 (0.0059)
1095 A. Q.	0.1486 (0.0206)	0.1080 (0.0156)	0.0732 (0.0117)
1095 Tempered	0.1452 (0.0202)	0.1153 (0.0160)	0.0764 (0.0106)
Ti-6Al-4V A.Q.	0.1377 (0.0311)	0.1033 (0.0233)	0.0660 (0.0149)
Ti-6Al-4V Tempered	0.1317 (0.0297)	0.1011 (0.0228)	0.0660 (0.0149)
Modified Fe_3Al 50% Ordered	0.1598 (0.0280)	0.1271 (0.0223)	0.0826 (0.0145)
Modified Fe_3Al 100% Ordered	0.1258 (0.0221)	0.0991 (0.0174)	0.0672 (0.0118)

Table 10

Relative Ranking of the Erosion Resistance Based on Volume Loss After
Exposure To 50 gm of 68 micron Quartz at 180 mps and of the Dynamic
Hardness Obtained from Impacts with 69 micron Spheres at 180 mps

Erosion Resistance	Dynamic Hardness
NiAl	Cr
Cr	Fe-10Cr
Fe-30Cr	Ti-6Al-4V Tempered
FeAl	1095 Tempered
1095 As-quenched	Modified Fe_3Al 100% ordered
1095 Tempered	Modified Fe_3Al 50% ordered
Fe-10Cr	Ti-6Al-4V As-quenched
Fe_3Al	FeAl
Ni_3Al	Fe-30Cr
Modified Fe_3Al 100% ordered	NiAl
Modified Fe_3Al 50% ordered	Fe_3Al
Ti-6Al-4V Tempered	Ni_3Al
Ti-6Al-4V As-quenched	

3

GENERAL CONCLUSION

Developing a general theory on the erosion mechanism of metals is a noble goal, unfortunately, the complexity of the physical events during an impact makes the task rather formidable. Erosion necessarily requires large amounts of plastic deformation at very high strain rates for very short durations. Mechanical properties and material response at high strain rates are not well understood, further complicating the understanding of erosion. This current program attempted to elucidate the effect of microstructural variations on the erosion characteristics of metals. The work showed that the microstructural features had only a minor affect on erosion. The results also indicated that the more fundamental "lattice" type changes have a greater affect on erosion resistance. The significance of this observation has practical implications in that it severely limits any erosion control possible by material processing alone. Erosion control is only provided by the application of materials with inherent erosion resistance.

Development of the dynamic hardness measuring techniques has provided a method of determining a material property at very high strain rates. Measurements have been made at strain rates as high as 7×10^6/sec. A correlation between erosion resistance and dynamic hardness was observed; however, further refinements in the dynamic hardness technique are required before precise data can be generated. The study of erosion has been seriously lacking material property data at very high strain rates; however, the current technique provides a means of measuring a high strain rate property over a broad range of dynamic conditions.

END

MICROCOPY RESOLUTION TEST CHART
NATIONAL BUREAU OF STANDARDS-1963-A
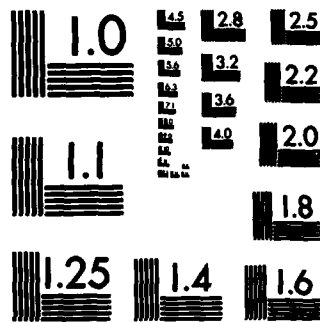
REFERENCES

1. Smeltzer, C.E., Gulden, M.E., McElmury, S.S., and Compton, W. A., 1970, "Mechanisms of Sand and Dust Erosion in Gas Turbine Engines", USAAVLABS Technical Report 70-36.

2. Finnie, I., Wolak, J., and Kabin, C., 1967, "Erosion of Metals by Solid Particles", Jr. of Materials, 2, No. 3.

3. Winter, R.E., and Hutchings, I.M., 1975, "The Role of Adiabatic Shear in Solid Particle Erosion", Wear, 35, pp. 141-148.

4. Jennings, W.H., Manning, C.R., Jr., and Head, W.J., "A Mechanical Model for Prediction of Ductile Erosion", USAAMRDL-TR-75-30.

5. Hutchings, I.M., 1977, "Strain-Rate Effects in Microparticle Impact", J. Phys. d: Appl. Phys., 10, pp. 151-156.

6. Campbell, J.D., 1973, "Review Paper Dynamic Plasticity: Macroscopic and Microscopic Aspects", Mat. Sc. & Eng., 12, pp. 3-21.

7. Hutchings, I.M., 1975, "Prediction of the Resistance of Metals to Erosion by Solid Particles", Wear, 35, pp. 371-374.

8. Vijh, A. K., 1976, "Resistance of Metals to Erosion by Solid Particles in Relation to the Solid State Cohesion of Metals", Wear, 39, pp. 173-175.

9. Metcalfe, A. G., 1978, Solar Turbines International, Private Communication.

10. Hutchings, I.M., "Proceedings Corrosion/Erossin of Coal Conversion Materials Conference," N.A.C.E. (1979) p. 393.

11. Finnie, I., 1960, "An Experimental Study of Erosion", Proc. S.E.S.A. (Vol. 17) (2), pp. 65-70.

12. Ruff, A.W. and Ives, L.K., 1975, "Measurement of Solid Particle Velocity in Erosive Wear", Wear, 35, pp. 169-182.

13. Tool Steel Catalog, Universal-Cyclops Steel Corp., p. 103.

14. Capus, J.M., 1967, in Temper Embrittlement in Steel, ASTM STP 407, pp. 3-19.

15. Gulden, M.E., 1980, "Study of Erosion Mechanisms of Engineering Ceramics, Static Fatigue of Ceramics", Dept. of Navy Office of Naval Research, Technical Report NR032-542.

16. Gulden, M.E., 1979, "Solid Particle Erosion of High Technology Ceramics", ASTM STP 664, Erosion: Prevention and Useful Applications.

17. Gulden, M.E., 1979, "Influence of Brittle to Ductile Transition on Solid Particle Erosion Behavior", Proc. Fifth International Conference on Erosion by Liquid and Solid Impact, Cambridge, England.

18. Torrance, A.A., 1978, "The Metallography of Worn Surfaces and Some Theories of Wear", Wear, 50, pp. 169-182.

19. Lindholm, U.S., Review of Dynamic Testing Techniques and Material Behavior", Inst. of Physics Conference Ser. No. 21, pp. 3-21.

20. Rogers, H.C., 1979, "Adiabatic Plastic Deformation", Annual Review of Materials Science, Vol. 9, pp. 283-404.

21. Rosenfield, A.L. and Hahn, G. T., Trans. Am. Soc. Metals, 59 (1966) p. 962.

22. Briggs, T. L. and Campbell, J.D., Acta Met., 20 (1972) p. 711.

23. J.D. Campbell, A.M. Eleidre and M.C.C. Tsao, "Strength of Metals and Alloys at High Strains and Strain Rates", Battelle Colloquim or Fundamental Aspects of Structural Alloy Design, Plennum Press, pp. 545-563.

24. I.M. Hutchings, "A Model for the Erosion of Metals by Spheroid Particles at Normal Incidence", Wear, vol. 70, August 15, 1981, pp. 269-281.

25. D.C. Rickerby and N.H. MacMillan, "The Erosion of Aluminum by Solid Particle Impingement at Normal Incidence", Wear, vol. 60, 1980, pp. 369-382.

APPENDIX 1

DYNAMIC HARDNESS TEST DATA

Material	Particle Diameter (μm)	Particle Velocity (m/sec)	Crater Diameter (μm)	Crater Depth (μm)	Dynamic Hardness (MPA)	Dynamic Strain Rate (sec^{-1})
Mg	69	207	40.1	6.4	2,400	2.4×10^6
		181	37.9	5.6	2,300	2.3×10^6
		153	35.6	4.9	2,200	2.1×10^6
	158	182	98.8	17.3	1,300	8.4×10^5
		159	97.8	16.9	1,000	7.5×10^5
		98	76.2	9.8	1,200	6.2×10^5
Al	69	207	49.0	10.1	1,000	1.9×10^6
		181	46.2	8.8	1,000	1.8×10^6
		153	39.9	6.3	1,300	1.8×10^6
	158	182	108	21.3	900	7.5×10^5
		159	104	19.5	800	6.9×10^5
		98	89	13.8	600	5.1×10^5
Cr	69	207	23.2	2.0	23,400	4.4×10^6
		181	20.5	1.5	29,700	4.4×10^6
		153	17.7	1.2	38,000	4.2×10^6
	158	182	25.5	1.0	343,000	3.8×10^5
		159	24.6	1.0	304,000	3.2×10^5
		98	27.0	1.2	80,000	1.8×10^5
Fe	69	207	29.2	3.22	9,100	3.5×10^6
		181	28.7	3.10	7,500	3.1×10^6
		153	25.4	2.41	8,800	3.0×10^6
	158	182	81.3	11.3	3,000	1.1×10^6
		159	76.7	9.9	3,000	1.0×10^6
		98	58.4	5.6	3,500	8.3×10^5

Material	Particle Diameter (μm)	Particle Velocity (m/sec)	Crater Diameter (μm)	Crater Depth (μm)	Dynamic Hardness (MPa)	Dynamic Strain Rate (sec^{-1})
Ni	69	207	31.1	3.7	7,000	3.2×10^6
		181	30.8	3.6	5,600	2.9×10^6
		153	26.2	2.6	7,700	2.8×10^6
	158	182	80.2	10.9	3,000	1.1×10^6
		159	78.6	10.5	3,000	9.6×10^5
		98	60.7	6.1	3,000	7.9×10^5
Cu	24	240	16.3	3.3	11,800	6.9×10^6
		209	14.2	2.4	16,600	6.8×10^6
		123	11.3	1.4	15,100	5.3×10^6
	69	207	37.7	5.6	3,100	2.6×10^6
		181	34.6	4.6	3,400	2.5×10^6
		112	30.6	3.5	2,200	1.8×10^6
	158	182	95.7	16.1	1,500	8.8×10^5
		159	94.4	15.7	1,200	7.7×10^5
		98	72.4	8.8	1,400	6.5×10^5
Zn	69	207	37.7	5.6	3,100	2.6×10^6
		181	30.7	3.6	5,600	2.8×10^6
		153	34.0	4.5	2,600	2.1×10^6
	158	182	85.0	12.4	2,500	1.5×10^6
		159	85.4	12.5	2,000	8.8×10^5
		98	70.5	8.3	1,500	6.8×10^5

Material	Particle Diameter (μm)	Particle Velocity (m/sec)	Crater Diameter (μm)	Crater Depth (μm)	Dynamic Hardness (MPa)	Dynamic Strain Rate (sec^{-1})
Mo	69	207	30.5	3.5	7,600	3.3×10^6
		181	27.9	2.9	8,400	3.2×10^6
		153	25.4	2.4	8,400	3.0×10^6
	158	182	70.1	8.2	5,500	1.3×10^6
		159	70.1	8.2	4,500	1.1×10^6
		98	53.6	4.7	5,000	9.1×10^5
Fe$_3$Al	69	207	33.1	4.2	5,400	3.0×10^6
		181	32.7	4.1	4,300	2.7×10^6
		153	27.7	2.9	6,100	2.7×10^6
	158	182	----	---	----	----
		159	63.4	7.8	4,800	1.0×10^5
		98	64.6	6.9	2,300	7.4×10^5
FeAl	69	207	30.7	3.6	7,400	3.3×10^6
		181	30.7	3.6	5,600	2.8×10^6
		153	29.6	3.3	4,700	2.5×10^6
	158	182	68.9	7.9	6,000	1.3×10^6
		159	65.8	7.2	5,600	1.2×10^6
		98	60.6	6.0	3,000	8.0×10^5
Ni$_3$Al	69	207	33.6	4.3	5,100	3.0×10^6
		181	33.0	4.2	4,100	2.6×10^6
		153	35.8	5.0	2,100	2.0×10^6
	158	182	86.1	12.8	2,400	1.0×10^6
		159	74.3	9.3	3,400	1.0×10^6
		98	63.0	6.5	2,600	7.7×10^5

Material	Particle Diameter (μm)	Particle Velocity (m/sec)	Crater Diameter (μm)	Crater Depth (μm)	Dynamic Hardness (MPA)	Dynamic Strain Rate (sec^{-1})
NiAl	69	207	31.6	3.8	6,500	3.2×10^6
		181	32.0	3.9	4,800	2.7×10^6
		153	28.9	3.2	5,200	2.5×10^6
	158	182	69.2	8.0	6,000	1.3×10^6
		159	68.2	7.7	4,800	1.1×10^6
		98	----	--	-----	--------
90Fe-10Cr	69	207	27.6	2.9	11,400	3.6×10^6
		181	22.9	1.9	18,800	3.9×10^6
		153	22.9	1.9	13,300	3.4×10^6
	158	182	46.6	3.5	30,100	2.0×10^6
		159	47.6	3.7	21,100	1.7×10^6
		98	43.6	3.1	16,800	1.1×10^6
70Fe-30Cr	69	207	34.4	4.5	4,700	2.9×10^6
		181	31.3	3.8	5,100	2.7×10^6
		153	33.0	4.2	3,000	2.2×10^6
	158	182	73.4	9.1	4,700	1.2×10^6
		159	81.0	11.2	2,400	9.3×10^5
		98	57.5	5.4	3,700	8.5×10^5
Al2024-T6	69	207	42.7	7.3	1,600	2.2×10^6
		181	37.1	5.4	2,600	2.2×10^6
		153	33.0	4.2	3,100	2.2×10^6
	158	182	102	18.7	1,100	8.0×10^6
		159	96.0	16.2	1,100	7.6×10^6
		98	77.2	10.1	1,100	6.1×10^5

Material	Particle Diameter (μm)	Particle Velocity (m/sec)	Crater Diameter (μm)	Crater Depth (μm)	Dynamic Hardness (MPA)	Dynamic Strain Rate (sec⁻¹)
Ti-6Al-4V (A.Q.)	69	207	28.3	3.0	10,300	3.6×10^6
		181	28.1	3.0	8,100	3.1×10^6
		153	24.8	2.3	9,700	3.0×10^6
	158	182	69.4	8.0	5,900	1.3×10^6
		159	65.0	7.0	5,900	1.2×10^6
		98	51.1	4.3	5,800	9.5×10^5
Ti-6Al-4V (Tempered)	69	207	28.8	3.1	9,600	3.5×10^6
		181	24.4	2.2	14,600	3.7×10^6
		153	25.8	2.5	8,300	2.9×10^6
	158	182	68.2	7.7	6,300	1.3×10^6
		159	66.8	7.4	5,300	1.2×10^6
		98	52.6	4.5	5,400	9.3×10^5
SAE 1095 (A.Q.)	69	207				
		181				
		153				
	158	182				
		159				
		98				
SAE 1095 (Tempered)	69	207	23.7	2.1	21,500	4.3×10^6
		181	25.9	2.5	11,300	3.5×10^6
		153	23.7	2.1	11,600	3.2×10^6
	158	182	67.8	7.6	6,500	1.3×10^6
		159	64.5	6.9	6,100	1.2×10^6
		98	50.2	4.1	6,500	9.7×10^5

Material	Particle Diameter (μm)	Particle Velocity (m/sec)	Crater Diameter (μm)	Crater Depth (μm)	Dynamic Hardness (MPA)	Dynamic Strain Rate (sec^{-1})
Modified Fe$_3$Al 50% ordered	69	207	28.7	3.1	9,700	3.5×10^6
		181	27.7	2.9	8,600	3.2×10^6
		153	25.6	2.5	8,300	2.9×10^6
	158	182	68.6	7.8	6,200	1.3×10^6
		159	64.7	6.9	6,000	1.2×10^6
		98	47.6	3.7	8,000	1.0×10^6
Modified Fe$_3$Al 100% ordered	69	207	31.9	3.9	6,300	3.1×10^6
		181	26.5	2.6	10,400	3.4×10^6
		153	26.1	2.5	7,900	2.9×10^6
	158	182	72.1	8.7	5,000	1.2×10^6
		159	68.5	7.8	4,800	1.1×10^6
		98	55.2	5.0	4,400	8.8×10^5

END

FILMED

9-84

DTIC